University of Sussex

Development Of A Planar Penning Trap For Quantum Applications With Electrons

April Louise Cridland

Submitted for the degree of Doctor of Philosophy

University of Sussex

September 2018

Declaration Of Authorship

I, April Cridland, declare that this thesis titled, **Development Of A Planar Penning Trap For Quantum Applications With Electrons** and the work presented in it are my own. I confirm that:

- This work was done wholly or mainly while in candidature for a research degree at this University.
- Where any part of this thesis has previously been submitted for a degree or any other qualification at this University or any other institution, this has been clearly stated.
- Where I have consulted the published work of others, this is always clearly attributed.
- Where I have quoted from the work of others, the source is always given. With the exception of such quotations, this thesis is entirely my own work.
- I have acknowledged all main sources of help.
- Where the thesis is based on work done by myself jointly with others, I have made clear exactly what was done by others and what I have contributed myself.

Signed:

Date:

Abstract

UNIVERSITY OF SUSSEX

April Louise Cridland

Doctor of Philosophy

Development Of A Planar Penning Trap For Quantum Applications With Electrons

This thesis presents the development of the Geonium Chip, a planar Penning trap. The Geonium Chip consists of the five electrodes of a cylindrical Penning trap projected onto the surface of a microfabricated chip. Beneath the chip is a planar magnetic field source currently made from coils of niobium titanium wire. Traditionally the magnetic field source is a large superconducting solenoid, replacing this with a planar source makes the setup scalable, portable and economical.

The Geonium Chip, with its magnetic field source and detection electronics, need to be placed in a cryostat. In this thesis, I describe the development of the cryogenic setup with particular emphasis on the design and optimisation of the non-destructive detection system. I detail the cryogenic wiring of the cryostat including the thermalisation of high current wires and the noise reduction techniques employed on the detection signal. In addition, I explore the parasitic capacitances of the Geonium Chip using microwave network analysis and describe the testing of the magnetic field source at 4 K. Finally, I discuss the generation of electrons within the trap and the results of our first attempts at trapping a cloud of electrons.

Together, the chip and the magnetic field source can be used to trap ions for ultra-accurate mass spectrometry or an electron for single microwave photon detection. A single microwave photon detector is a tool that is currently still missing in quantum technology and is needed for determining the quantum state of microwave radiation fields. This is vital for quantum communication and cryptography. Additionally, using the Geonium Chip as a mass spectrometer has the potential to lead to very accurate mass spectrums without the need for frequent calibration. Finally, eliminating the expensive superconducting solenoid will make accurate mass spectrometry available to a wider market.

Acknowledgements

Firstly, thank you to my supervisor, Dr Jose Verdu Galiana, for his valuable support and being generous with his time. Thank you to the members of the Geonium team: Jonathan, John, Frances, Alberto and Ryan, who have been fundamental in the completion of the work contained within this thesis and have provided a great deal of assistance over the last four years. I would also like to thank the members of the ITCM and IQT groups for sharing their equipment, resources and a series of fruitful discussions. Finally, thank you to Abhijit and my family for their continued patience and emotional support.

I would like to acknowledge EPSRC and the school of Mathematics and Physics, University of Sussex as the main source of funding for this project with additional funding received from the SEPnet impact fund.

In addition to work performed by the author, data has also been included where the majority of results have been obtained by other members in the Geonium Chip group:

- **Chapter 2** - The mathematical model of the Geonium Chip and the plots in figures 2.8 to 2.10 have been obtained by Dr Jose Verdu Galiana.
- **Tables 4.3 and 4.4** - Data was obtained by PhD candidate Alberto Uribe.
- **Figure 4.19** - Data was obtained by PhD candidate John Lacy.

Contents

List of Tables

List of Figures

Chapter 1

Introduction

1.1 Penning Traps

A Penning trap confines a charged particle's motion by combining an electrostatic field with a magnetic field. The electrostatic field is generated by metallic electrodes such that a harmonic potential well is formed along the axis of the trap. The magnetic field forces the particle to undergo a circular motion around its axis, confining the particle "radially" within the trap. Once trapped, the particle motion is a superposition of three harmonic oscillators giving it three distinct frequencies; the axial, magnetron and cyclotron. The axial frequency is caused by the electrostatic potential well, the cyclotron frequency is mainly caused by the magnetic field and the magnetron frequency is due to the combination of the magenetic and electric fields. The name 'Penning' trap was coined by Hans Dehmelt [11, 12] in deference to Franz Penning who noticed that electron lifetime in coaxial cylinders could be increased with the use of a magnetic field [13]. Dehmelt later went on to recieve a Nobel prize for his work with ion traps in 1989 [14].

In 1973, Dehmelt used a hyperbolic Penning trap to trap and detect a single electron [15]. This single electron setup was then used to measure the free electron g-factor via the continuous Stern-Gerlach effect [16] giving a value for the magnetic anomaly that was measured to a precision of 10^{-12}. It is at this point that Dehmelt introduces the term 'geonium' to mean an electron *'bound to the earth via the trap structure and the magnet'* [17]. From here we have taken the name of our trapping system as the Geonium Chip, a system capable of trapping one single electron above the surface of a chip based Penning trap.

1.1.1 Planar Penning Traps

The original planar Penning trap designs were motivated by the intent to realise a scalable quantum computer. Currently the most advanced technology in quantum computing is a linear Paul trap [18–20]. However, cryogenic Penning traps are also good candidates. They combine static electric and magnetic fields to give low decoherence rates [22] and two-dimensional arrays of planar traps can address scalability issues. Arrays allow a higher density of qubits than can be achieved with a linear array of 3D traps [23]. The progress of microfabrication means that arrays of both Paul and Penning traps can now be fabricated with smaller trap dimensions and these arrays are not only repeatable but can also be produced with a high yield [24, 25]. Additionally, in 2003 I. Marzoli and P. Tombesi proposed a single electron in a Penning trap as a quantum processor [26, 27]. Three-dimensional Penning traps had already enabled a high level of control over the quantum spin state of a single trapped electron [28]. The spin states can be used to form the basis of a quantum register as these states are long lived, allowing gate operation times to be much smaller than decoherence times [26].

As a result, planar Penning trap designs [23, 29–31] were put forward with the intention of trapping a single electron. A cloud of electrons were trapped in a planar Penning trap both at room temperature [32, 33] and at 100 mK [34]. However, the design in [32] suffered from a lack of mirror symmetry about the potential minimum preventing the electrostatic potential from being harmonic. This anharmonic potential led to a frequency broadening of the electron signal and prevented the resolution of a single electron [34]. In response, optimised planar trap designs were proposed [35] and have potentially detected a single trapped electron. However, improvements in the trap stability and detection sensitivity are required to state this with confidence [36]. Therefore, the detection of a single electron in a planar Penning trap remains a current experimental challenge.

1.2 Applications of Penning Traps

Penning traps not only have applications in quantum computing but they have also provided the most stringent tests of quantum electrodynamics (QED) [37]. The free electron g-factor was measured in a cylindrical Penning trap at Harvard and was found to agree with the QED predicted value to a precision of $\left|\frac{\Delta g}{2}\right| < 9 \times 10^{-13}$ [38, 39]. The move to a cylindrical trap, from the original hyperbolic trap, allowed the trap to be considered as a microwave cavity leading to a better calculation of the electrostatic field and uncer-

tainties caused by cavity shifts. This was due to a better understanding of the cavity's radiation field.

Penning traps have also been used to test CPT-symmetry in the lepton and baryon sectors. In the lepton sector the electron and positron g-factors were compared with an uncertainty of 2×10^{-12}, allowing their $g-2$ values to be compared with a greater than 4 ppb precision [40, 41]. In the baryon sector the BASE collaboration [42] have compared the charge to mass ratio of the proton $\left(\frac{q}{m}\right)_p$ to that of the antiproton $\left(\frac{q}{m}\right)_{\bar{p}}$ achieving $\left(\frac{q}{m}\right)_p / \left(\frac{q}{m}\right)_{\bar{p}} - 1 = 1(69) \times 10^{-12}$, which is in excellent agreement with CPT invariance [43].

Finally, Penning traps have been used to determine fundamental constants. These are values which are not predicted by theory but their ratios and relationships to other constants can be. In particular, a recent measurement of the atomic mass of a single proton has been achieved with a precision of 32 ppt [44]. This gives the proton-electron mass ratio to a relative precision of 43 ppt, a factor of 2 more precise than the previous value [45]. This ratio is important for comparing experimental measurements with theoretical predictions across different areas of physics [46].

Penning traps have therefore proved themselves to be ultra-precise and versatile instruments for probing the nature of physics. We rely on the experimental progress made in the above references to address two particular applications to which the Geonium chip is suited; single microwave photon detection and ultra-accurate mass spectrometry.

1.2.1 Single Microwave Photon Detection

A fundamental tool in quantum-optics is a single photon detector. Photon detectors in the optical regime have been used in radiation-matter interactions leading to applications in quantum information processing, metrology and spectroscopy [47–49]. However, there are currently no efficient single photon detectors in the microwave regime [50, 51]. These photons have energies of 4 - 5 orders of magnitude less than those in the optical sector [52]. This makes resolving single microwave photons challenging.

Efficient single microwave photon detectors are needed for determining and manipulating the quantum state of radiation fields which is vital for quantum information, communication and cryptography. Single microwave photon detectors could also lead to ultra-accurate microwave spectroscopy. Microwave spectroscopy is used to observe the rotational spectra of gaseous molecules. This has applications in investigating the interstellar medium, the bonding structure of molecules and the monitoring of some manufacturing

processes [53].

Designs for single microwave photon detectors have been developed using superconductor and semiconductor technology [54] with a research group recently achieving a single photon efficiency of 0.66 ± 0.06 [52]. However, this was a achieved with a low bandwidth of $\sim 2\pi \times 16$ MHz and was operated in a time-gated mode rather than a continuous mode. The desirable features of a single microwave detector are that it achieves a high efficiency, be broadband, passive and single shot [55].

Our approach to the problem is to use a trapped electron as a transducer. This was the method first used to detect single microwave photons [28]. We will use the Geonium Chip with an integrated planar magnetic field source to trap electrons. The electrons will be loaded into the trap using the photoelectric effect. Photoelectrons will be released from the surface of the chip using an ultraviolet light source. The released photoelectrons will then be confined by the magnetic and electric fields. Once the photoelectrons are confined the reduced cyclotron motion will be cooled to its ground state using a custom made miniature adiabatic demagnetisation refrigerator (ADR) which is being developed at the Mullard Space Science Laboratory [56] and will be able to reach 80 mK. This initialises the cyclotron mode ready to detect an incoming microwave photon and eliminates any thermal photons already in the system.

Microwave photons will be collected from the outside environment using an antenna and guided into the Geonium chip using a Coplanar-waveguide transmission line. The MW photons will interact with the electron's cyclotron mode provided that their frequency is close to the electron's cyclotron frequency. This interaction can be detected using the continuous Stern-Gerlach effect [57]. The continuous Stern-Gerlach effect relies on the use of a magnetic bottle which consists of a curvature in the magnetic field. The curvature causes the the axial potential seen by the electron to become dependent upon the quantum state of the cyclotron motion. When a single incoming MW photon is resonant with the electron's cyclotron frequency it is absorbed and the quantum number of the cyclotron energy increases by one. Due to the axial potential's dependence on the cyclotron energy's quantum state the potential shifts, and as a result the electron's axial frequency also undergoes a discrete shift. This process can be seen in figure 1.1.

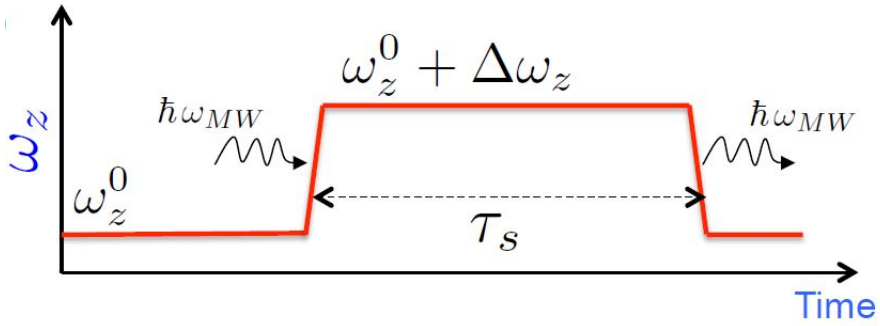

Figure 1.1: When the trapped electron is placed in a magnetic bottle its axial frequency (ω_z) becomes dependent upon the quantum state of its cyclotron motion. When a single incoming resonant MW photon is absorbed the cyclotron quantum state increases by one, causing a discrete shift ($\Delta\omega_z$) in the axial frequency [53]. After a time period (τ_s) equal to the radiative lifetime of the cyclotron state, spontaneous emission causes the photon to be re-emitted.

The detection of the axial frequency is described in detail in Chapter 3 and its detection leaves the cyclotron state unchanged. This is therefore a quantum non-demolition detection (QND) and the incident photon can be recovered. Multiple microwave photons can also be detected because the magnitude of the shift in the axial frequency is directly proportional to the number of microwave photons that interact with the electron [53].

The electron's reduced cyclotron frequency is mainly determined by the strength of the magnetic field. As a result the Geonium Chip could potentially be tuned from 2.8 GHz to 56 GHz using a magnetic field strength of 0.1 T to 2 T[1]. Potentially, the frequency could be increased up to 100 GHz making this a broadband detection system. The efficiency of the Geonium Chip does not suffer from the limitations seen in lamda three level systems such as in [51] and is theoretically capable of 100% quantum efficiency [53].

The Geonium Chip is therefore capable of becoming a high efficiency, broadband quantum non-demolition detector of single microwave photons.

1.2.2 Mass Spectrometry

Mass spectrometry is the process of obtaining the mass to charge ratio ($\frac{m}{q}$) of an unknown analyte ion, thereby chemically identifying the ion. It has applications in food testing, forensics, pharmacology, analysis of petro-chemicals and many other fields. Mass spectro-

[1]The upper limit of 2 T is the current capability of the planar magnetic field source which is made from niobium titantium and therefore has a critical current above which, the source is no longer superconducting. It is not a fundamental limitation of the Geonium Chip.

metry is a mature technology but is still subject to technical advancement and a growing market. In 2015 the global market for instruments alone was $3 billion and is expected to grow at a compound annual rate of 7.6 % [58]. The Geonium Chip has the potential to fit into a gap in this market and provide high accuracy mass spectrometry with a smaller footprint and capital outlay than current competing technologies. The two main competitors of the Geonium Chip are the Fourier Transform - Ion Cyclotron Resonance (FT-ICR) and the Orbitrap.

Fourier Transform - Ion Cyclotron Resonance

An FT-ICR is a room temperature Penning trap that detects the cyclotron frequency of the analyte ions. The ions are injected into the trap and excited by a radio frequency resonant with the cyclotron motion. This excitation pushes the ions into a wider orbit and groups them into spatially coherent packets [59]. The wider orbit is necessary to take the ions closer to the detection plates so that they induce an image charge on the plates that is large enough to be amplified and detected. The ions also need to be spatially coherent as the image charges are picked up from two parallel detection plates. If the ions were uniformly distributed then they would induce currents which were 180° out of phase on each plate which would then sum to zero, preventing detection of the ions. The induced current oscillates at the same frequency as the ions. It is amplified and then Fourier transformed to the frequency domain to create a spectrum of peaks. The peaks occur at frequencies coinciding with the ions' cyclotron frequencies and whose heights relate to the ions' abundances. Their mass to charge ratios can then be calculated from their cyclotron frequences (ν_p) using [60]

$$\frac{m}{q} = \frac{A}{\nu_p} + \frac{B}{\nu_p^2}, \tag{1.1}$$

where A and B are constants that are found from the calibration of the FT-ICR.

The calibration of the FT-ICR requires at least two different calibrant ions of known mass to charge ratio and is most effective when the calibrant ions are injected along with the analyte ions. Therefore, to achieve the maximum accuracy a calibration needs to be carried out every time a new sample is analysed. This makes the spectrum more difficult to interpret. They also require ~ 100 ions of a particular $\frac{m}{q}$ to induce a measurable signal [60] and will therefore suffer from accuracy loss if the ion statistics are not high enough.

FT-ICRs can obtain the highest accuracy and resolution in the mass spectrometry market, however they are also the most expensive with costs approaching $1 million, due

to their use of large superconducting solenoids to provide the magnetic field.

Orbitrap

The Orbitrap is a modified Knight-Kingdon trap [61] which consists of two electrodes; an outer barrel electrode and an inner spindle. This trap is purely electrostatic and does not use a magnetic field. The electrodes produce a quadro-logarithmic potential which causes the ions to orbit the central electrode in a radial motion and transverse its length in an axial motion. The radial field bends the ion towards the inner electrode but the ions' initial tangential velocity creates an opposing centrifrugal force. When these forces are balanced the ions undergo an almost circular orbit around the central electrode, thereby trapping them radially. The electric field in the axial direction is purely linear and the conical shape of the electrode pushes the ions into the widest part of the trap [62], trapping them axially.

As the potential in the axial direction is purely quadratic, the ions' motion can be described as a harmonic oscillator which is completely independent of the radial motion and the ions' initial parameters. The radial motion however, is strongly dependent upon the ions' initial energy and after 50-100 oscillations the ions of a particular mass to charge ratio dephase from a packet into a thin ring of uniformly distributed ions. The ions' frequencies are detected using the image current they induce on the two halves of the outer electrode, which is followed by differential amplification, in the same manner as the FT-ICR. Consequently, the radial motion will induce opposite currents on the outer electrodes which will cancel each other out. It is therefore impossible to measure the mass to charge ratio of an ion using the radial frequency. However, in the axial direction the ions remain in phase for hundreds of thousands of oscillations before the ion packet broadens due to trap imperfections and background gas collisions. This allows the axial frequency to be measured using broadband image current detection and fast Fourier transform to the frequency domain. The mass to charge ratio is calculated using [63]

$$\omega_z = \sqrt{(q/m)k}, \tag{1.2}$$

where k is the electrostatic field curvature which is obtained during calibration.

The Orbitrap has a mass resolution of 150,000 which is only surpassed by the FT-ICR. However, it has a larger trapping volume and as a result of the shielding provided by the central electrode it has an increased space charge capacity at higher masses. Although the Orbitrap avoids the use of a superconducting solenoid which reduces the initial costs,

it is still placed at the upper end of the market. The quality of the mass spectrum is also defined by many different parameters making it a complex instrument [5].

Geonium Chip

The Geonium Chip can operate as an FT-ICR with the added benefits of being smaller, more economical and without the need for regular calibration. The Geonium Chip has the potential to be portable with an accuracy and resolution 4 - 5 orders of magnitude higher than current portable systems [5]. We are currently exploring the feasibility of commercialising the Geonium Chip as a mass spectrometer and figure 1.2 shows the expected position of our technology in the current mass spectrometry market.

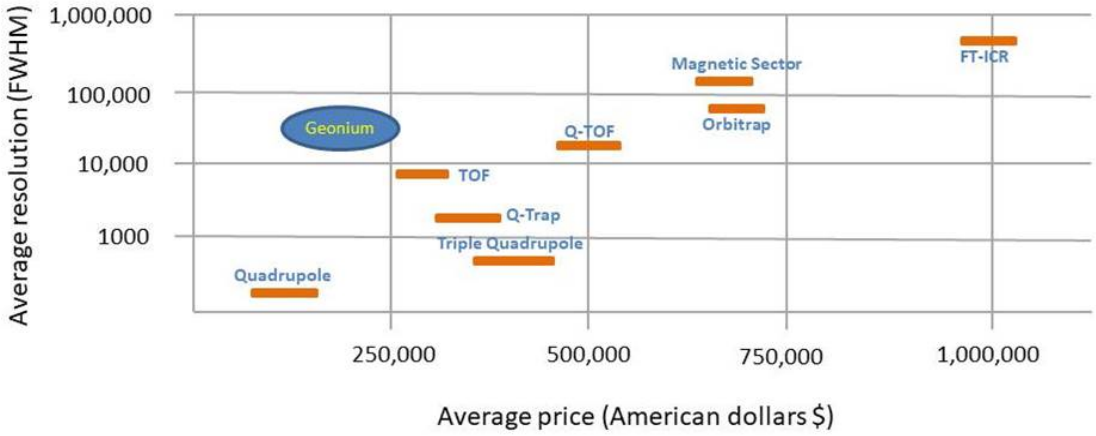

Figure 1.2: Potential market position of the Geonium Chip with respect to the Orbitrap and FT-ICR [5]. The average resolution of the Geonium Chip depicted here is a conservative estimate.

The Geonium Chip will be operated at cryogenic temperatures where ions will not need to be excited prior to detection. The detection scheme will use the image charge technique seen in FT-ICRs and Orbitraps but the image current will only be picked up from one electrode. Therefore, differential amplification will not be used and the ions' phase will not affect the detection signal. The magnetic field will be provided by a planar source negating the need for an expensive large bore magnet. This dramatically reduces the capital outlay making the technology accessible to a wider market.

Once the ions are injected into the trap they will undergo the three motions introduced in section 1.1; the reduced cyclotron (ω_p), magnetron (ω_m) and axial (ω_z). The cyclotron and axial frequencies will be measured using broadband image current detection and fast Fourier transformed to the frequency domain as seen in both the FT-ICR and Orbitrap.

The magnetron frequency does not depend upon the mass of the ion and can therefore be measured prior to the operation of the mass spectrometer using an electron. Once this has been measured it no longer needs to be measured again. The free cyclotron frequency (ω_c) of the ion of interest is then calculated from the powerful Brown-Gabrielse invariance theorem [64]

$$\omega_c = \sqrt{\omega_z^2 + \omega_p^2 + \omega_m^2}. \tag{1.3}$$

This calculated free cyclotron frequency is completely independent of any trap imperfections or ellipticity and can be used to determine the mass to charge ratio using

$$\frac{m}{q} = \frac{B}{\omega_c}, \tag{1.4}$$

where B is the strength of the magnetic field in the axial direction. Therefore, once the two measured frequencies are known the mass to charge ratio can be calculated. Using this method means that the free cyclotron frequency is obtained directly and therefore the trap does not need calibrating once it is in operation.

The mass resolution shown in figure 1.2 is calculated from the centre of a mass peak (m) divided by the full width at half maximum of the peak (Δ m). Using equation 1.4 the mass resolution is therefore dependent upon the uncertainty in the measurement of the free cyclotron frequency $\frac{\Delta\omega_c}{\omega_c}$, which is $\simeq 10^{-6}$ in the best case scenario. This is limited by the precision of the voltage supplies used for the trapping potential. However, in reality there will also be other experimental limitations due to the stability of the magnetic field and the temperature dependent frequency fluctuations.

1.3 Thesis Content

This thesis details the building of the first cryogenic setup to incorporate the Geonium Chip. The aim of this project was to demonstrate the trap's capability of confining charged particles so that it can be further developed for the applications listed above.

To that end, chapter 2 describes the overall design of the Geonium Chip and how the trapping voltages can be chosen to produce a harmonic trapping potential. The process by which the trapped particle can be detected, with emphasis on the parameters that can affect the effectiveness of the detection system, is explained in chapter 3. Chapter 4 details the investigation into the Geonium Chip's high frequency response using microwave network analysis to determine the chip's parasitic capacitances. The building and

characterisation of the planar magnetic field source, including its performance at 4 K, is described in chapter 5. Chapter 6 discusses the building of the detection system, from optimising the helical resonator to making a cryogenic amplifier. The rest of the cryogenic setup including the cryostat, electronics and thermalisation considerations are explored in chapter 7 which also describes the techniques undertaken to reduce noise on the detection signal once the entire setup was complete. Finally, the current status of the experiment and the next steps planned for its progression are explored in chapter 8.

At the beginning of this PhD project the Geonium group had acquired a 4 K pulse tube and received a custom cryostat designed by J.Pinder and manufactured by the Sussex University Workshop. The cryostat included radiation shields and mechanical mounting struts but no wiring. In addition, the microfabricated design of the Geonium Chip had not yet been finalised. As such, this thesis details much of the physical components necessary to build and wire a new cryogenic system.

Chapter 2

Trapping Of Charged Particles

This chapter introduces the design of the Geonium Chip planar Penning trap and most importantly its capability of producing a harmonic trapping potential. As stated in section 1.1.1 previous planar Penning trap designs have suffered from anharmonic potentials which have prevented the detection of a single electron. The chapter begins by reviewing the trapping principles of a Penning trap with reference to our planar design before discussing the electrostatic potential created by the chip's electrodes. The potential reveals that the Geonium Chip is an elliptical Penning trap, whose ellipticity can be controlled by the trapping voltages. The elliptical nature of the trap leads to the ideal motion of a charged particle within the trapping volume and the effect that imperfections in the trapping potential can have on the particle's eigenfrequencies. It is shown that these imperfections in the potential can be minimised through appropriate choices of trapping voltages. Finally, the conditions required for a harmonic trapping potential above the Geonium Chip are listed.

2.1 Principle Of Trapping

The Geonium Chip is based upon the projection of a five pole cylindrical Penning trap, onto a planar surface, as seen in figure 2.1.

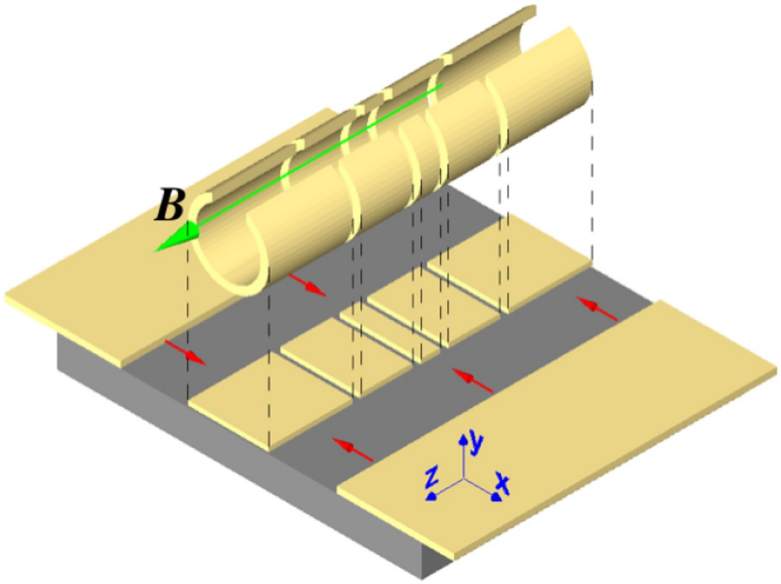

Figure 2.1: The projection of a 5 pole cylindrical Penning trap onto a planar surface sandwiched between two side electrodes [6]

The chip consists of five central electrodes bordered by two side electrodes. The central electrodes are made of the ring, two compensation electrodes and two endcaps as shown in figure 2.2. The electrodes are shielded by a ground plane which provides an equipotential reference. The centre of the ring electrode is chosen as the origin of the axes (0,0,0).

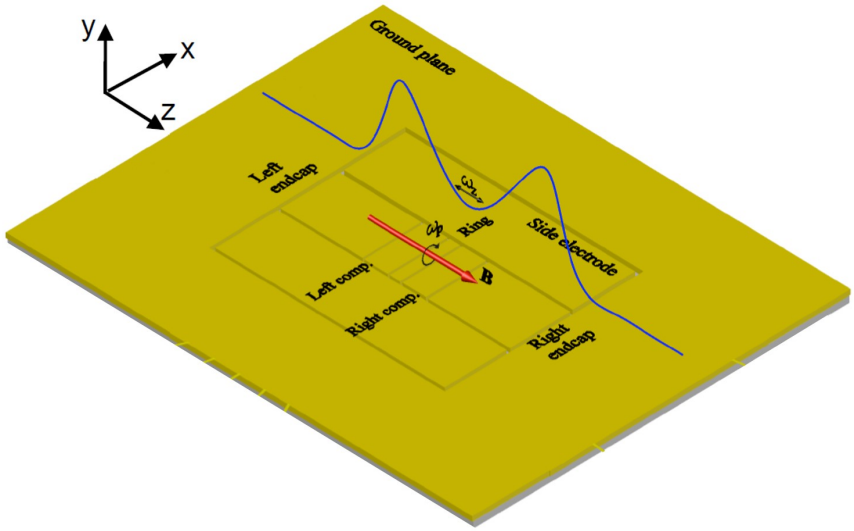

Figure 2.2: The electrodes of the Geonium Chip surrounded by a ground plane with the magnetic field (red) parallel to the surface of the chip and the electrostatic potential well (blue) illustrated above the central electrodes

When carefully chosen DC voltages are applied to the electrodes they generate an

axial potential well. The electron oscillates around the potential minimum at a tunable trapping height, $(0, y_0, 0)$, which is mathematically defined in section 2.2. The frequency of this axial oscillation, ω_z, is dependent solely on the voltages applied to the electrodes. However, the electric field is not sufficient to provide trapping in all directions. This is due to Earnshaw's theorem which states that a charged particle cannot be trapped by forces provided from one purely static electric field. This is because all of the force field lines would need to point towards the equilibrium position of the particle, ensuring that there is a restoring force in all directions. This makes the equilibrium position a sink and therefore the divergence of the field at that point must be negative. However, this violates Gauss' law which states that the divergence of any electric force field is zero in free space. Therefore, a force $(\vec{F})$ due to a purely electrostatic field obeys Laplace's equation

$$\nabla \cdot \vec{F} = \nabla \cdot (-\nabla \Phi) = -\nabla^2 \Phi = 0, \tag{2.1}$$

where Φ is the electrostatic potential. As a result, the field does not have a local maxima or minima, only a saddle point. The saddle point due to the electrostatic field gives a relative minimum along the z-axis and a relative maximum along the x and y axes as seen in figure 2.3.

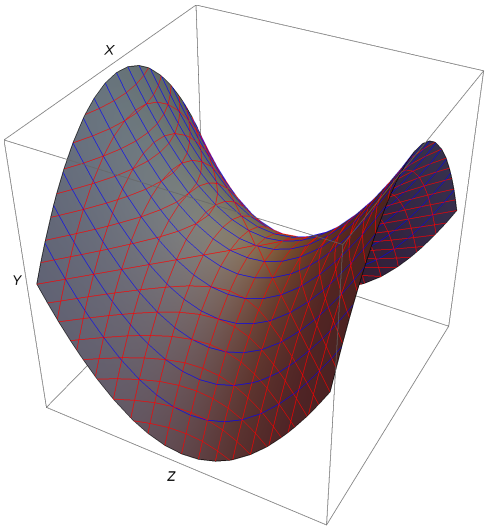

Figure 2.3: A saddle point with a relative minimum along the z-axes shown by blue contour lines and relative maximums along the x and y axes shown by red contour lines.

Therefore, to provide a restoring force in the x and y-directions an additional static magnetic field is required. The magnetic field source lies beneath the chip providing a homogeneous field parallel to the chip's surface and orientated in the axial direction (z). The electrons process around the axis of the magnetic field with a reduced cyclotron

frequency, ω_p, that is mainly dependent upon the strength of the magnetic field $\vec{B} = B_0 \cdot \hat{u}_z$ [65]. The final mode of the particle's oscillation is the slow drift of the magnetron frequency, ω_m, which is caused by a combination of the electric and magnetic fields. The motion of the electron is a superposition of these three harmonic oscillators and is depicted in figure 2.4.

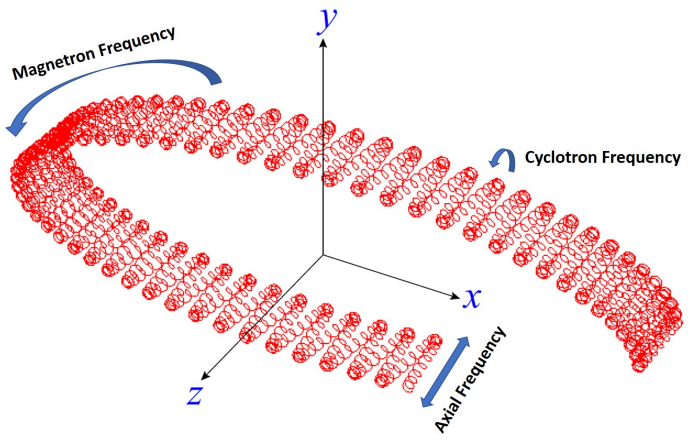

Figure 2.4: Motion of the electron within the trap showing the three frequencies of oscillation [6]

2.2 Electrostatic Potential

In order to calculate the voltages required for trapping, the electrostatic potential (Φ) of the trap inside a rectangular metallic box was calculated by J. Verdu [4]. The metallic box, with dimensions L_x, L_y and L_z (see figure 2.5), acts as a microwave cavity which increases the lifetime of the electron in the trap by reducing the spontaneous emission rate of the cyclotron motion. The microwave chamber is described in more detail in section 4.5. The expression for the electrostatic potential of the enclosed trap is [4]

$$\Phi(x, y, z) = \Phi_{\text{el}}(x, y, z) + \Phi_{\text{gaps}}(x, y, z), \tag{2.2}$$

where $\Phi_{\text{el}}(x, y, z)$ is the electrostatic potential of the chip modified by the presence of the microwave chamber and $\Phi_{\text{gaps}}(x, y, z)$ is the potential of the insulating gaps between the electrodes. The expression for $\Phi_{\text{gaps}}(x, y, z)$ can be seen in the Appendix A. $\Phi_{\text{el}}(x, y, z)$ is given by [4]

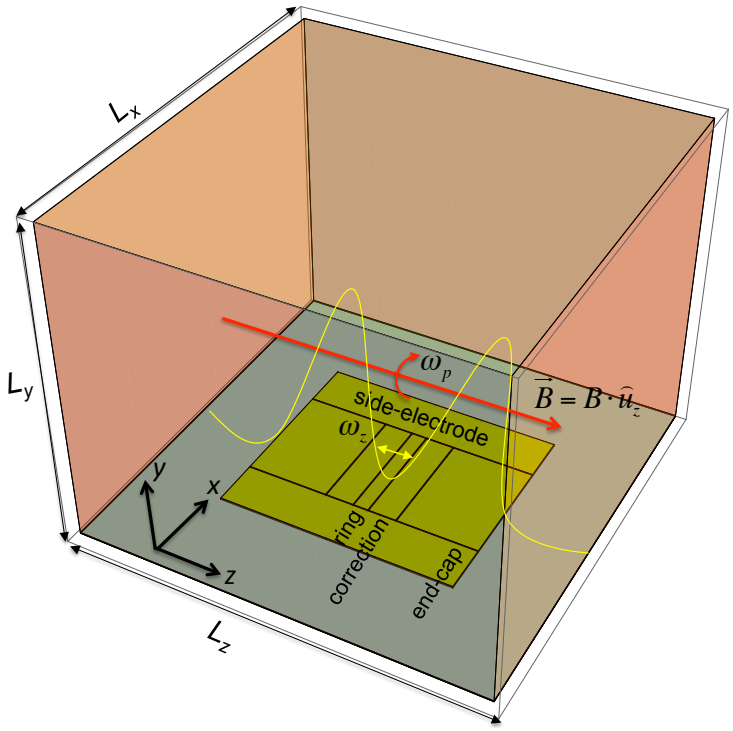

Figure 2.5: Sketch of the Geonium Chip within a metallic microwave chamber whose presence modifies the trapping potential [4]. The origin of the axes (0,0,0) is at the center of the ring electrode.

$$\Phi_{\mathrm{el}}(x,y,z) = \frac{4\,V_r}{\pi^2} \cdot \sum_m^\infty \sum_n^\infty \left\{ \sin\left(\frac{m\pi}{2}\right) \sin\left(\frac{n\pi}{2}\right) \right. \tag{2.3}$$
$$\times \frac{\Lambda^r_{m,n} + T_c\,\Lambda^c_{m,n} + T_e\,\Lambda^e_{m,n} + T_g\,\Lambda^g_{m,n}}{m \cdot n \cdot \sinh\left(A_{m,n}\,L_y\right)}$$
$$\left. \times \cos\left(\frac{m\pi\,z}{L_z}\right) \cos\left(\frac{n\pi\,x}{L_x}\right) \sinh\left(A_{m,n}(L_y - y)\right) \right\}$$

$$m = 1,3,5\ldots\infty \quad ; \quad n = 1,3,5\ldots\infty \quad \text{and } A_{m,n} = \pi\sqrt{\frac{m^2}{L_z^2} + \frac{n^2}{L_x^2}}.$$

The terms $\Lambda^r_{m,n}$, $\Lambda^c_{m,n}$, $\Lambda^e_{m,n}$ and $\Lambda^g_{m,n}$ are functions which define the contribution of each of the trap's electrodes to the total potential, where r refers to the ring, c to the correction electrode, e to the endcap and g to the side electrode. They are dependent upon the dimensions of the electrodes and the microwave chamber. Their explicit expressions can be seen in Table A.1 of Appendix A. The potential also depends upon the voltage ratios; T_c, T_e and T_g. T_g is the side electrode to ring voltage ratio, $T_g = V_g/V_r$ where V_g is the voltage applied to the side electrodes and V_r is the voltage applied to the ring. T_e is the endcap to ring voltage ratio, $T_e = V_e/V_r$ where V_e is the voltage applied to the

endcaps. Finally, T_c is the tuning ratio

$$T_c = \frac{V_c}{V_r}, \tag{2.4}$$

where V_c is the voltage applied to the compensation electrodes. T_c is particularly important for eliminating energy dependent fluctuations in the axial frequency and is discussed further in section 2.2.2. T_e mainly determines the height above the surface of the chip at which the electron is trapped. The trapping height, y_0, is defined as

$$\left.\frac{\partial \Phi(0,y,0)}{\partial y}\right|_{y=y_0} = 0, \tag{2.5}$$

and is therefore an equilibrium position in the electrostatic field. This position must be above the surface of the chip and coincide with an area of the magnetic field which is homogeneous. It must also be appropriate for the expected amplitude of the trapped particle's motion. If the trapped electron is too close to the surface of the chip it may strike the electrodes and be lost from the trap. The expected amplitudes of the particle's motion are discussed further in section 2.2.1. They depend upon the energies of the three motions (axial, cyclotron and magnetron) and the mass of the particle.

For such an equilibrium position to exist the voltages must also follow the inequality $|V_e| > |V_c| \gtrapprox |V_r|$, otherwise a potential well is not formed above the chip. Finally, T_g manipulates the ellipticity of the magnetron motion and its implications are discussed briefly in section 2.2.1.

2.2.1 Ellipticity

The curvature of the electrostatic potential along $\hat{u}_x$ $\left(C_{200} = \frac{1}{2}\frac{\partial^2 \Phi}{\partial x^2}\Big|_{(0,y_0,0)}\right)$ is not the same as that along $\hat{u}_y$ (C_{020}) meaning that the Geonium Chip is an elliptical Penning trap. The ideal quadrupole potential of the Geonium Chip (shown in figure 2.6) therefore becomes [6]

$$\Phi_{\text{quad}}(x,y,z) = C_{002}\left\{\left(z^2 - \frac{x^2 + (y-y_0)^2}{2}\right) + \frac{\epsilon}{2}\cdot(x^2 - (y-y_0)^2)\right\}, \tag{2.6}$$

where C_{002} is the curvature of the electrostatic potential along $\hat{u}_z$ and ϵ is the ellipticity of the trap. If the ellipticity is reduced to zero then the quadrupole returns to that of a cylindrically symmetric Penning trap [65]. The ellipticity is defined as

$$\epsilon = \frac{1-\xi}{1+\xi}, \quad \xi = \frac{C_{200}}{C_{020}}. \tag{2.7}$$

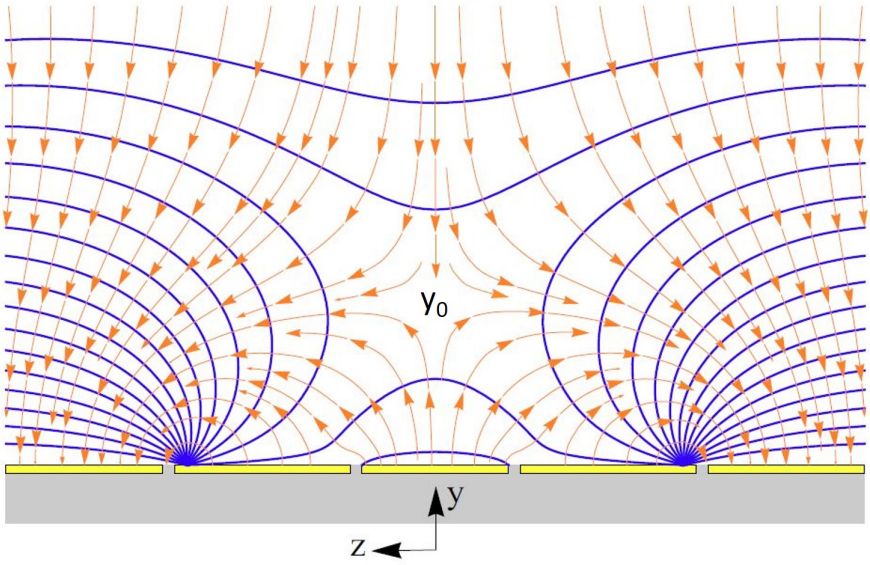

Figure 2.6: The ideal quadrupole potential of the Geonium Chip shown in blue with the electric field lines shown in orange [1]. The trapping position, y_0, is shown at the centre of the quadrupole. The field lines coming down towards the trap and completing the quadrupole, stem from the ground planes' interaction with the particle.

As stated earlier the ideal motion of the trapped particle is a superposition of three harmonic oscillators. The frequencies of these oscillations in an elliptical trap have been calculated analytically by M. Kretzschmar to give [66]

$$\omega_z = \sqrt{2C_{002}\frac{q}{m}}, \tag{2.8}$$

$$\omega_p = \sqrt{\frac{1}{2}(\omega_c^2 - \omega_z^2) + \frac{1}{2}\sqrt{\omega_c^2\,\omega_1^2 + \epsilon^2\,\omega_z^4}}, \tag{2.9}$$

$$\omega_m = \sqrt{\frac{1}{2}(\omega_c^2 - \omega_z^2) - \frac{1}{2}\sqrt{\omega_c^2\,\omega_1^2 + \epsilon^2\,\omega_z^4}}, \tag{2.10}$$

where $\omega_1 = \sqrt{\omega_c^2 - 2\omega_z^2}$, $C_{002} = \frac{1}{2}\frac{\partial^2\Phi}{\partial z^2}\Big|_{(0,y_0,0)}$, ω_c has already been defined in equation 1.4, q is the charge of the trapped particle and m is its mass. For an electron trapped above the surface of the Geonium chip with the dimensions given in [4][1] and the voltages: $V_r = -1$ V, $T_c = 1.045876$, $T_e = 2.741$ and $T_g = 0$ in a 0.5 T field the expected frequencies are

[1] width of central electrodes = 7 mm, width of side electrodes = 3 mm, length of ring electrode = 0.9 mm, length of compensation electrodes = 1.71 mm, length of endcap electrodes = 5.0 mm, gaps between electrodes = 50 μ m

$$\begin{aligned}\omega_z &= 2\pi \cdot 26\,\text{MHz},\\ \omega_p &= 2\pi \cdot 14\,\text{GHz},\\ \omega_m &= 2\pi \cdot 20\,\text{kHz},\end{aligned}$$

where in general $\omega_p > \omega_z > \omega_m$. The amplitudes of these motions are

$$A_z = \frac{1}{\omega_z}\sqrt{\frac{2E_z}{m}}, \tag{2.11}$$

$$A_p = \frac{1}{\omega_p}\sqrt{\frac{2E_p}{\gamma_+ m}}, \tag{2.12}$$

$$A_m = \sqrt{\frac{2E_m}{(\omega_m^2 - \omega_z/2)m}}, \tag{2.13}$$

where $\gamma_+ = 1 - \frac{\omega_z^2}{2\omega_p^2} \simeq 1$, E_p is the cyclotron energy, E_z is the axial energy and E_m is the magnetron energy of the particle. The magnetic field must be large enough to ensure that A_p does not become comparable with A_m. If they become comparable and $\omega_c^2 \leq 2\omega_z^2$, then ω_p becomes unphysical and A_p becomes imaginary (i.e. unbounded) [67].

The ellipticity only slightly affects the cyclotron orbit but it is what gives the magnetron orbit its oval shape. For the magnetron motion to be stable ϵ must be between 1 and -1. Outside of this range trapping is not possible as the magnetron motion becomes unbounded and hyperbolic [66]. The ellipticity can be experimentally measured using [4]

$$\epsilon = \pm\frac{\sqrt{(\omega_p^2 - \omega_m^2)^2 - \omega_c^2\omega_1^2}}{\omega_z^2}. \tag{2.14}$$

The sign of ϵ describes the orientation of the magnetron ellipse, whether the major axis of the oval is in the x or y direction. For the current geometry of the Geonium Chip we can only optimise the electrostatic potential for a positive ϵ and therefore the major axis of the magnetron motion lies in the x-direction. The ellipticity is controlled by T_g and therefore for a constant ring voltage the aspect ratio of the magnetron motion is controlled by the voltage applied to the side electrodes. The variation of this aspect ratio with the ellipticity of the electrostatic potential can be seen in figure 2.7. Alternative dimensions of the Geonium Chip can be computed that allow T_g to be manipulated such that $\epsilon = 0$ and the trap becomes cylindrically symmetric.

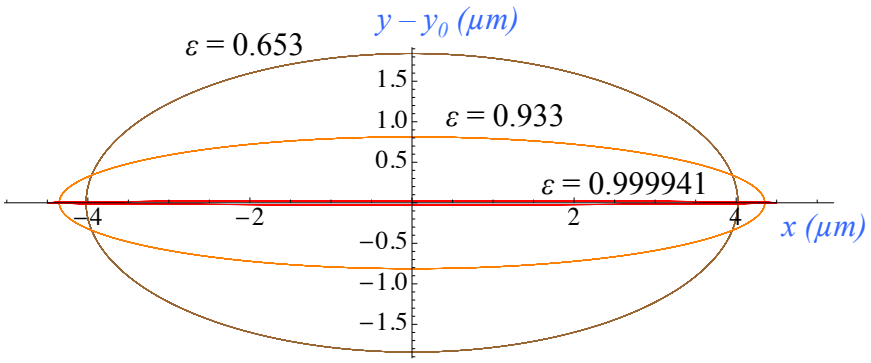

Figure 2.7: Variation of the aspect ratio of the magnetron motion with the ellipticity of the electrostatic trapping potential [4].

As $\epsilon \to 1$ the minor axis of the ellipse becomes very small and the motion becomes almost linear. This confines the electron to a finite horizontal plane of $y = y_0$ and $\omega_m \to 0$. To achieve this ultra-elliptical regime sideband cooling must be applied to the magnetron motion before ϵ is driven adiabatically towards 1.

The magnetron motion follows equipotential lines around a potential hill and therefore to cool the motion, energy must be injected into the magnetron mode to push it up the potential hill. This causes the radius of the magnetron motion to reduce. Sideband cooling uses a drive frequency of $\omega_m + \omega_z$ to couple the axial and magnetron motions. Once coupled the motions can exchange energy and therefore energy can be pumped into the magnetron mode causing its radius to reduce. The axial mode is continuously resistively cooled by its connection to the detection electronics and is therefore not heated by this process [65].

This ultra-elliptic regime has the potential to achieve a quasi two-dimensional electron gas above the surface of the chip but further discussion on this is beyond the scope of this thesis.

2.2.2 Anharmonicities

In reality the trap does not follow the ideal electrostatic potential presented in [66]. Using a series expansion of the potential $\Phi(x, y, z)$ around the equilibrium position $(0, y_0, 0)$ anharmonicities up to the fourth order can be found [6]

$$\begin{aligned}\Phi(x,y,z) &= \phi(0,y_0,0) + \ldots\ldots \\ &+ \underbrace{C_{002}\,z^2 + C_{200}\,x^2 + C_{020}\,(y-y_0)^2}_{\phi_{quad}} + \underbrace{C_{012}\,z^2(y-y_0) + C_{210}\,x^2\,(y-y_0) + C_{030}\,(y-y_0)^3}_{\text{odd anharmonicities}} \\ &+ \underbrace{C_{202}\,z^2\,x^2 + C_{022}\,z^2\,(y-y_0)^2 + C_{220}\,x^2\,(y-y_0)^2 + C_{004}\,z^4 + C_{400}\,x^4 + C_{040}\,(y-y_0)^4}_{\text{even anharmonicities}}. \quad (2.15)\end{aligned}$$

The coefficients of the expansion are given by

$$C_{ijk} = \frac{1}{i!\,j!\,k!} \cdot \frac{\partial^{i+j+k}\,\phi(x,y,z)}{\partial x^i\,\partial y^j\,\partial z^k}\Big|_{(0,y_0,0)}. \tag{2.16}$$

Each anharmonicity produces frequency shifts which scale linearly with the electron's energies and as such can be expressed as a matrix [6]

$$\begin{pmatrix} \Delta\nu_p \\ \Delta\nu_z \\ \Delta\nu_m \end{pmatrix} = \underbrace{\begin{pmatrix} M_{1,1} & M_{1,2} & M_{1,3} \\ M_{2,1} & M_{2,2} & M_{2,3} \\ M_{3,1} & M_{3,2} & M_{3,3} \end{pmatrix}}_{M=\text{frequency-shifts matrix}} \cdot \begin{pmatrix} \Delta E_p \\ \Delta E_z \\ \Delta E_m, \end{pmatrix} \tag{2.17}$$

The overall frequency shifts matrix is a sum of all the individual matrices and an illustrative example, for one electon, taken from [6] is

$$M = \begin{pmatrix} 5\cdot 10^{-6} & 0.5 & -0.9 \\ 1\cdot 10^{-3} & 203 & -411 \\ -2\cdot 10^{-6} & -0.4 & 2 \end{pmatrix} \text{ Hz K}^{-1}. \tag{2.18}$$

The most dangerous frequency shift is caused by $M_{2,2}$ as it leads to a dependence of the axial frequency on the axial energy. The axial frequency is particularly important as it can be used to determine the other frequencies through sideband coupling [65] and the energy level of the cyclotron motion through the Stern-Gerlach effect. A fluctuation of 203 Hz K^{-1} could prevent the particle from being detected. However, an optimal tuning ratio (T_c^{opt}) can be found which eliminates $M_{2,2}$ as seen in figure 2.8.

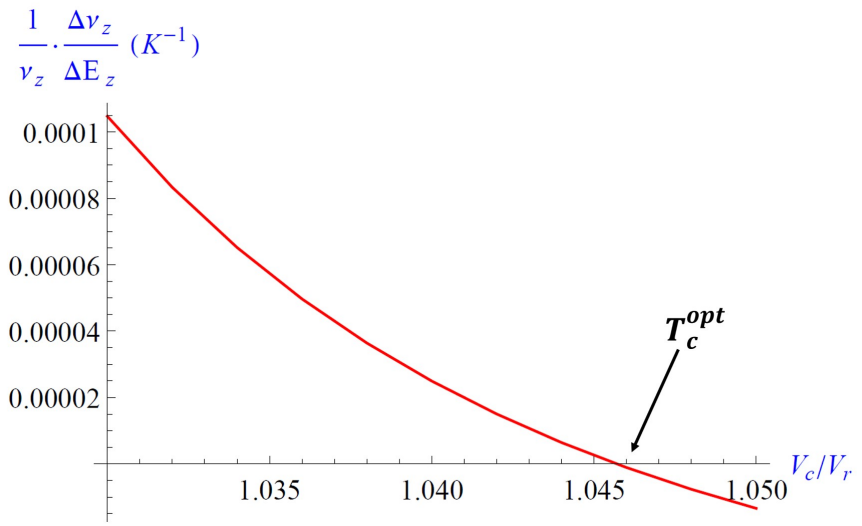

Figure 2.8: The variation of $M_{2,2}$ with T_c to find the optimal tuning ratio T_c^{opt} which eliminates the linear dependence of the axial frequency on the axial energy

T_c^{opt} can be found for a range of trapping heights, thereby giving the trap a *useful trapping interval*, which is seen in figure 2.9. Outside of this interval T_c^{opt} cannot be found and $M_{2,2}$ cannot be completely eliminated, reducing the accuracy of the frequency measurements. Therefore, the values of V_c and V_e with respect to V_r must be chosen carefully to keep y_0 within the useful trapping interval.

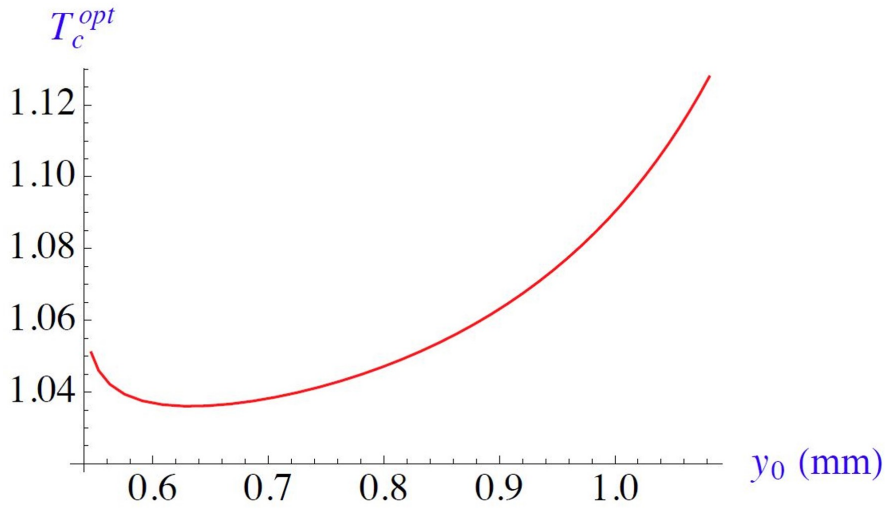

Figure 2.9: The range of trapping heights for which an optimum tuning ratio can be found [4], for the dimensions given in that publication. Alternative dimensions of the electrodes give different values of T_c^{opt}.

The useful trapping interval in figure 2.9 was calculated with $T_g = 0$. However, T_g does not need to be zero. Figure 2.10a shows that an optimal tuning ratio can be found

for other values of T_g whilst T_e is kept constant. In fact, T_g can be used to extend the useful trapping interval. Figure 2.10b shows that with a T_g of 3.0 an optimal tuning ratio can be found for values of y_0 from 1.0 mm up to 1.7 mm. Whereas when T_g is kept at zero the useful trapping region only extends from 0.55 mm to 1.13 mm [4].

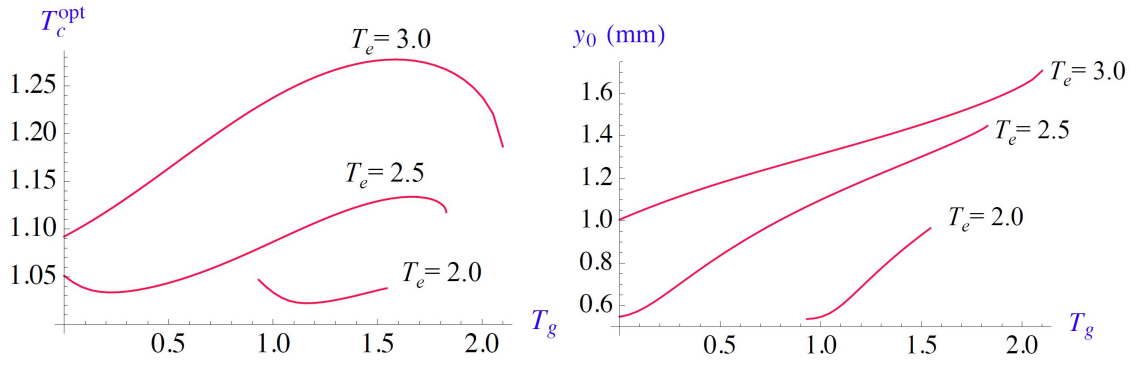

(a) T_c^{opt} for a range of T_g

(b) Useful trapping interval for a range of T_g

Figure 2.10: Optimal tuning ratios for a range of T_g which can be used to extend the useful trapping interval [4]

The extension of the useful trapping interval may prove useful when trapping larger ions by allowing them to be trapped further from the surface of the chip. For the rest of this thesis T_g is considered to be set to zero.

2.3 Requirements For Trapping

The requirements for trapping are:

- A magnetic field parallel to the surface of the chip which is large enough to prevent A_p from becoming too large and unbounded.
- $|V_e| > |V_c| \gtrapprox |V_r|$ must be fulfilled to ensure that there is an equilibrium position above the surface of the chip in which the charged particle can be held.
- $-1 > \epsilon > 1$ is required to maintain a stable magnetron motion and therefore a well defined magnetron frequency.
- y_0 must be within the useful trapping interval so that the frequency shift caused by $M_{2,2}$ can be eliminated by finding T_c^{opt}.

Chapter 3

Detection Of Trapped Charged Particles

This chapter describes the detection of a single trapped electron's axial frequency and the methods which can be employed to optimise the detection system.

There are two types of detection systems; destructive and non-destructive. Destructive detection systems consist of releasing charged particles from the trap and accelerating them towards a detection plate such as a microchannel plate [68]. The motional frequencies of a cloud of particles can be found by exciting the cloud with a 'tickle' frequency before releasing them from the trap to collide with the detection plate. If the 'tickle' frequency is resonant with one of the motional frequencies then the more energetic particles in the cloud will become so excited that they leave the trap before the cloud is forcably ejected towards the detection plate. Therefore, if the residual ion number is plotted as a function of the 'tickle' frequency then there will be a dip in the residual ion number at each of the cloud's resonant frequencies [68, 69]. The main disadvantage of this approach is that not only does the trap have to be reloaded for each change in the 'tickle' frequency but also that measurement statistics can only be increased by reloading the trap and repeating the measurement multiple times. Non-destructive detection however, allows the frequency of a particle to be measured whilst the particle is still orbiting within the trap. Here, measurement statistics can be increased by time-averaging the signal [70]. Non-destructive detection is also particularly important for our intended application of the detection of signal microwave photons. As explained in section 1.2.1 we wish to build a system which detects the presence of microwave photons without affecting their quantum state. This would not be possible with a destructive detection system, as losing the electron from the trap would also destroy the information stored in its cyclotron mode. The chapter begins

by reviewing the non-destructive detection technique introduced in section 1.2.2 with particular application to our planar trap. This then leads to the important parameters of the system which can be optimised to maximise the detection signal. To that end the system is also modelled using microwave network analysis to assess its performance at high frequencies and investigate the effects of coupling the trap with the detection system. Finally, requirements for an optimal detection system for the Geonium Chip are stated.

3.1 Principle Of Detection

Once the principles in chapter 2 have been applied and the electron is trapped above the surface of the Geonium Chip, it induces positive charges on the the trap's electrodes. This distribution of positive charges move across the surface of the chip with the electron, thereby creating an induced current, as seen in figure 3.1. The induced current oscillates at the same frequency as the electron.

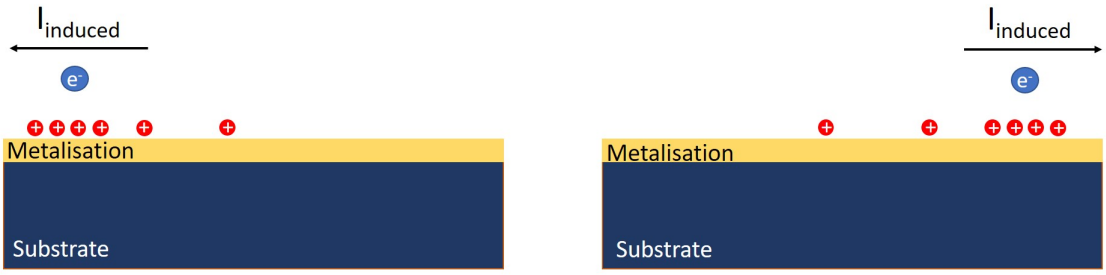

Figure 3.1: The trapped electron induces a positive charge distribution on the surface of the Geonium Chip which oscillates at the same frequency as the electron.

The induced current can be picked up from one of the electrodes and passed through a very large resistor to create an induced voltage (figure 3.2) which can then be further amplified. However, the chip has a parasitic capacitance to ground which will form an AC short at high frequencies. This would completely bypass the resistor and prevent the induced voltage from passing to the rest of the detection system. To mitigate this, a tuned inductance rather than a pure resistance can be used. The tuned inductance is provided by a helical resonator which consists of a coil located in a conductive shield. The coil's inductance tunes out the parasitic capacitance of the chip so that on resonance the inductance of the coil completely compensates the coil's self capacitance and the parasitic capacitance of the chip to leave only a resistive response. This ensures that the current passes through the resonator and induces a voltage there, rather than going to ground through the chip's parasitic capacitance. The parasitic capacitance of the chip is discussed

in great detail in chapter 4.

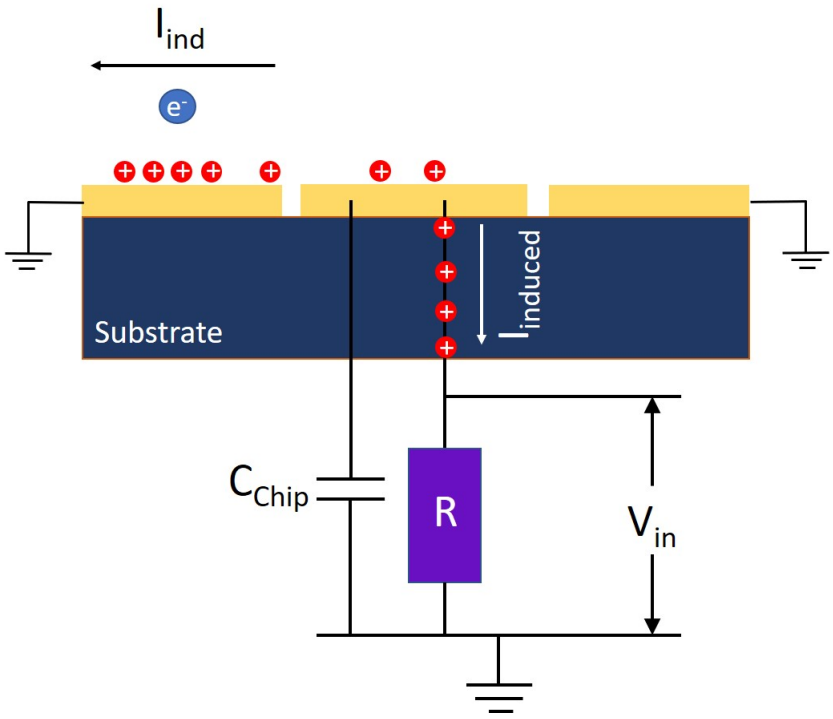

Figure 3.2: The induced current is picked up from one of the electrodes and passed through a large resistor to induce a large voltage. If the parasitic capacitance of the chip is too large, then the induced current will flow to ground through the capacitor rather than the resistor, thereby preventing the electron from being detected.

The voltage induced across the helical resonator is

$$V_{\text{ind}} = I_{\text{ind}} \cdot Z(\omega), \tag{3.1}$$

where I_{ind} is the current induced by the motion of the electron and $Z(\omega)$ is the frequency dependent impedance of the helical resonator. This voltage is the signal that is used to detect the trapped electrons and must be maximised to ensure that the signal is large enough to be observed at room temperature. The resonator presents a higher impedance at its resonance frequency and a lower impedance at all other frequencies. This maximises the voltage drop on resonance and minimises the voltage drop at all other frequencies thereby reducing background noise [70]. The helical resonator can be electrically represented as a tank circuit which consists of the self-inductance of the coil (L), the parasitic capacitance between the coil's windings and its shield (C) and its resistive losses (R) all connected in parallel. Its equivalent circuit and frequency response can be seen in figure 3.3.

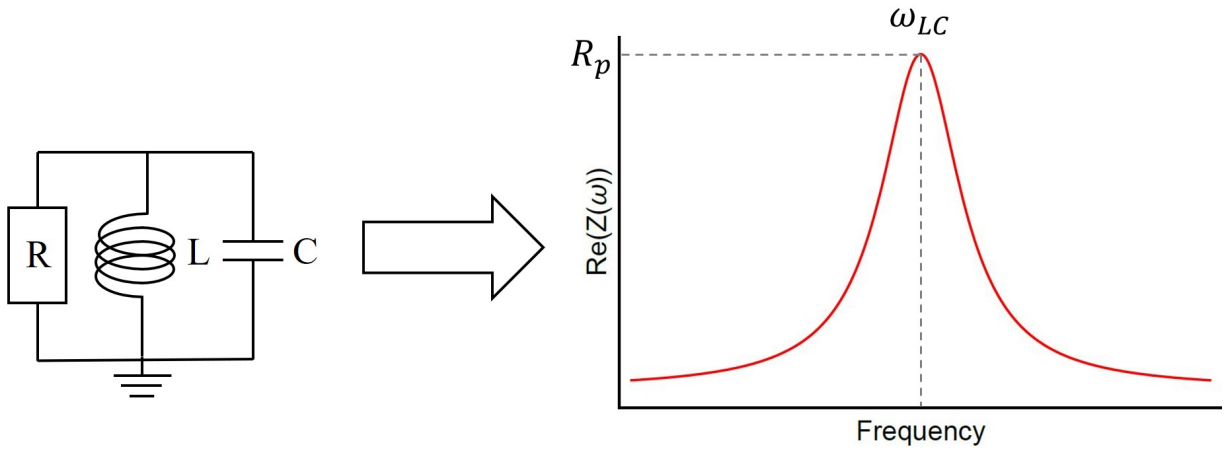

Figure 3.3: Left: The lumped element representation of a tank circuit. Right: The real part of the frequency response of a parallel tank (LCR) circuit where the resonance peaks at $\omega_{LC} = 2\pi\nu_{LC}$ with a maximum impedance of R_p, the parallel resistance of the tank circuit.

The full detection circuit now becomes that shown in figure 3.4 [7] where the chip is capacitively coupled to the parallel tank circuit of the helical resonator. The capacitive coupling prevents the DC trapping voltage applied to the electrode from entering the detection electronics. The induced voltage is amplified as close to the chip as possible to maintain a high signal to noise ratio. This signal is passed through a room temperature amplifier to a Fast Fourier Transform (FFT) spectrum analyser which transforms the signal from the time domain to the frequency domain. In the frequency domain the unexcited 4 K noise of the coil appears as a peak in the voltage and the signal of the electron is superimposed onto this as a peak or a dip depending upon the temperature of the electron with respect to the resonator. This is discussed further in section 3.1.4.

3.1.1 Effective Coupling Distance

An important decision must now be made on which electrode to capacitively couple to the detection system. The majority of this thesis is concerned with measuring the axial frequency of the trapped electron but the following mathematical treatment is also relevant for the electron's cyclotron frequency.

The electron's motion, $\mathbf{r} = \mathbf{r}(t)$, generates the induced current which is nothing other than the variation of the induced charge (q_{ind}) with time

$$I_{\text{ind}}(t) = \frac{d\, q_{\text{ind}}(\mathbf{r}(t))}{dt} = \nabla q_{\text{ind}}(\mathbf{r}) \cdot \dot{\mathbf{r}}(t). \tag{3.2}$$

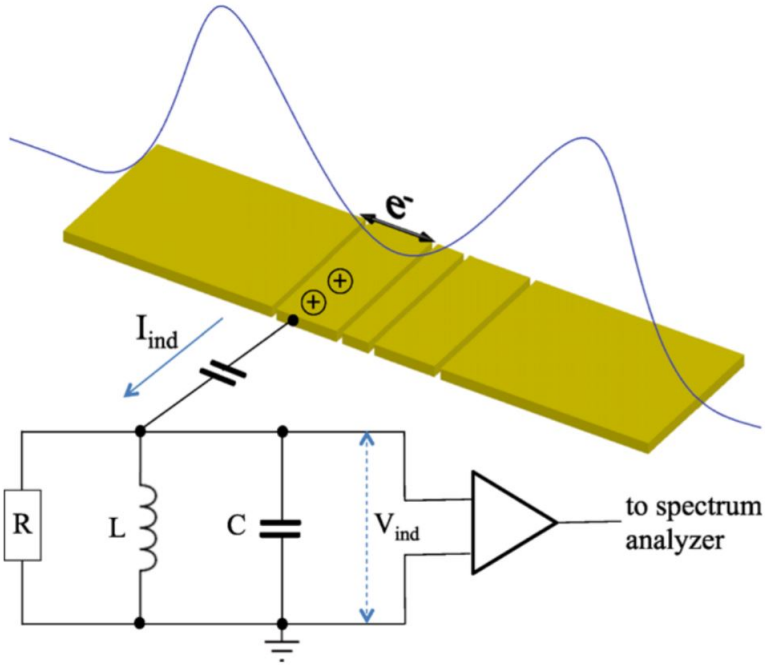

Figure 3.4: The full detection system consisting of a parallel tank circuit capacitively coupled to one of the electrodes of the Geonium Chip. The induced voltage is amplified in the cryogenic region and then passed to the room temperature amplifier and FFT [7].

The charge induced on each electrode can be found from the integration of the surface charge over the dimensions of the electrode. This leads to a complex dependence of the induced charge on the position of the particle at each point in time. This can be simplified using the 'effective coupling distance approximation' [7] which approximates the particle's position as its equilibrium position $(0, y_0, 0)$. This is because the particle's motion is small in comparison with the size of the electrodes. The coupling between the electron and a particular electrode can now be represented by an effective coupling vector, $\mathbf{D}_{\text{eff}}^{-1}$, which leads to an induced current of

$$I_{\text{ind}} = -\frac{q}{\mathbf{D}_{\text{eff}}^{-1}} \cdot \dot{\mathbf{r}}, \tag{3.3}$$

and therefore an induced voltage of [7]

$$V_{\text{ind}}(\omega) = -qZ(\omega)\mathbf{D}_{\text{eff}}^{-1} \cdot \dot{\mathbf{r}}. \tag{3.4}$$

The effective coupling vector has three components, D_{eff}^{i}, which have the dimensionality of a length and are known as effective coupling distances

$$\mathbf{D}_{\text{eff}}^{-1} = \left(\frac{1}{D_{\text{eff}}^{x}}, \frac{1}{D_{\text{eff}}^{y}}, \frac{1}{D_{\text{eff}}^{z}} \right). \tag{3.5}$$

This means that the induced voltage is a linear combination of the voltages induced by all three of the electron's frequencies. However, the tank circuit only presents a high impedance close to its resonance frequency, so any frequencies far from resonance will experience a negligible impedance. Therefore, the voltage induced by only one frequency of motion will be passed to the cryogenic amplifier and the rest of the detection system.

Physically the effective coupling vector is the normalised electric field ($\mathbf{E}$) produced by a particular electrode at the position of the trapped electron $(0, y_0, 0)$

$$\mathbf{D}_{\text{eff}}^{-1}(y_0, \Sigma) = \frac{1}{1\,\text{Volt}}\mathbf{E}_{\Sigma}(0, y_0, 0), \tag{3.6}$$

where Σ represents the dimensions of the electrode. As a result, each electrode will provide a different coupling vector. This has a direct consequence on the choice of pickup electrode. To detect the axial motion, whose information is contained within the z motion of the particle, the induced voltage must be maximised and therefore, from equation 3.4, D_{eff}^{z} must be minimised. For the ring electrode, $D_{\text{eff}}^{z} = \infty$ [4] so the most practical option is to detect the axial motion through one of the correction electrodes.

The information of the cyclotron motion is contained within the x and y motion of the particle. However, due to the symmetry of the trap along $\hat{u}_x$, $D_{\text{eff}}^{x} = \infty$ for all of the central electrodes. Therefore, the cyclotron motion must be detected through the particle's y motion and D_{eff}^{y} is at its lowest in the ring, so the ring is the best pickup electrode for measuring the cyclotron frequency. Although the electron's cyclotron frequency is very high (GHz) and no resonator can be built for this frequency, a microwave cavity can be used in its place.

3.1.2 Electronic Model Of An Electron Within The Trap

To build a full model of the trapped electron's interaction with the detection system the forces acting on the electron need to be considered. Firstly, consider the electron trapped axially in the potential well at an equilibrium point above the surface of the electrodes without the helical resonator attached to the chip. Here, the electron feels the restoring force of the harmonic trapping potential and a force due to the presence of the trap's electrodes acting as an effective capacitor. The axial equation of motion of the electron becomes [71]

$$m\ddot{z} = -m\omega_z^2 z - \frac{qV}{D_{\text{eff}}^{z}}, \tag{3.7}$$

where the first term contains the harmonic restoring force of the trapping potential and the second term contains the external force due to the trap's effective capacitance. Equation 3.7 can be re-arranged to find the voltage that the electron generates on the trap's electrodes

$$-V = m\ddot{z}\frac{D^z_{\text{eff}}}{q} + m\omega_z^2 z\frac{D^z_{\text{eff}}}{q}. \tag{3.8}$$

Remembering equation 3.3 for the current induced by the electron, equation 3.8 can be expressed as [72]

$$V = \underbrace{m\frac{(D^z_{\text{eff}})^2}{q^2}\dot{I}}_{\text{voltage drop over an inductor}} + \underbrace{m\omega_z^2\frac{(D^z_{\text{eff}})^2}{q^2}\int I(t)dt}_{\text{voltage drop of a capacitor}}. \tag{3.9}$$

Equation 3.9 shows that the voltage generated by the trapped electron is equivalent to that of an inductor in series with a capacitor. The voltage of an inductor is given by $V_L = L\frac{dI}{dt}$, so the inductance of the electron becomes $L^z_{\text{electron}} = m\frac{(D^z_{\text{eff}})^2}{q^2}$. Likewise the voltage of a capacitor is given by $V_C = \frac{1}{C}\int Idt$ and therefore the capacitance of the electron is given by $C^z_{\text{electron}} = \left[m\omega_z^2\frac{(D^z_{\text{eff}})^2}{q^2}\right]^{-1}$. The resonance of the electron's axial frequency therefore becomes $\omega_z = \frac{1}{\sqrt{L^z_{\text{electron}}C^z_{\text{electron}}}}$. This process can be repeated with the other motions of the electron to find their equivalent inductance and capacitance.

3.1.3 Resistive Cooling Of The Electron's Motion

Connecting the trapped electron to the detection system produces an additional force on the electron. The voltage induced by the electron in the helical resonator generates its own electric potential which acts back upon the electron. This potential creates a force proportional to the electron's velocity [7]

$$\mathbf{F}_{\text{ind}} = -q^2 Z(\omega)\mathbf{D}^{-1}_{\text{eff}}\cdot(\mathbf{D}^{-1}_{\text{eff}}\cdot\dot{\mathbf{r}}), \tag{3.10}$$

therefore making it dissipative and responsible for resistively cooling the electron [72]. Taking into account this additional force the electron's axial equation of motion now becomes

$$m\ddot{z} = -m\omega_z^2 z - \frac{qV}{D^z_{\text{eff}}} - \frac{q^2 Z(\omega)}{(D^z_{\text{eff}})^2}\dot{z}, \tag{3.11}$$

which can be re-arranged to form the equation of motion of a driven damped harmonic

oscillator

$$m\ddot{z} + \frac{q^2 Z(\omega)}{(D^z_{\text{eff}})^2}\dot{z} + m\omega_z^2 z = \frac{qV}{D^z_{\text{eff}}}, \tag{3.12}$$

with a damping constant $\gamma_z = \frac{q^2 Z(\omega)}{m(D^z_{\text{eff}})^2}$. The damped energy falls exponentially [73] as it is ohmically dissipated in the helical resonator [74]. The time for the initial axial energy to fall by $\frac{1}{e}$ is given by the time constant

$$\tau_z = \frac{1}{\gamma_z} = \frac{m}{q^2} \cdot \frac{1}{Z(\omega)} \cdot (D^z_{\text{eff}})^2. \tag{3.13}$$

Yet again the effective coupling distance plays an important role in the detection system. Equation 3.13 shows that to minimise the time it takes for the trapped electron to cool to the temperature of the helical resonator the effective coupling distance must be minimised and the impedance of the resonator must be maximised.

3.1.4 Thermal Noise Of The Helical Resonator And The Trapped Electron

Now that the full electronic model of the electron's interaction with the detection system is known, the voltage reaching the FFT can be considered. The thermal voltage of the helical resonator is given by the Johnson noise of a resistor [72]

$$V = \sqrt{4k_B T B R}, \tag{3.14}$$

where k_B is the Boltzmann constant, B is the bandwidth of the system, T is the temperature in Kelvin and R is the resistance. For a helical resonator the resistance is given by the real part of the frequency dependent impedance ($Z(\omega)$). As the resistance is frequency dependent, so is its thermal noise spectrum. Therefore, the resonator's thermal noise spectrum has the same shape as its impedance profile which has already been seen in figure 3.3.

Section 3.1.2 has introduced the electron as electrically equivalent to an inductor and capacitor connected in series. A series LC circuit provides the same voltage response as a parallel LCR circuit but with a π phase shift. This means that together the voltage response of the trapped electron and the helical resonator looks like that in figure 3.5 where the electron appears as a dip in the peak of the resonator's thermal voltage spectrum. This voltage spectrum is only valid if the axial frequency of the electron equals the resonance frequency of the helical resonator, $\omega_z = \omega_{LC}$. As previously seen in chapter 2, the axial

frequency can be tuned by the trapping voltages and brought into resonance with the helical resonator. This model also assumes that the electron is in thermal equilibrium with the rest of the detection system, if this is not the case then the electron is seen as a peak rather than a dip.

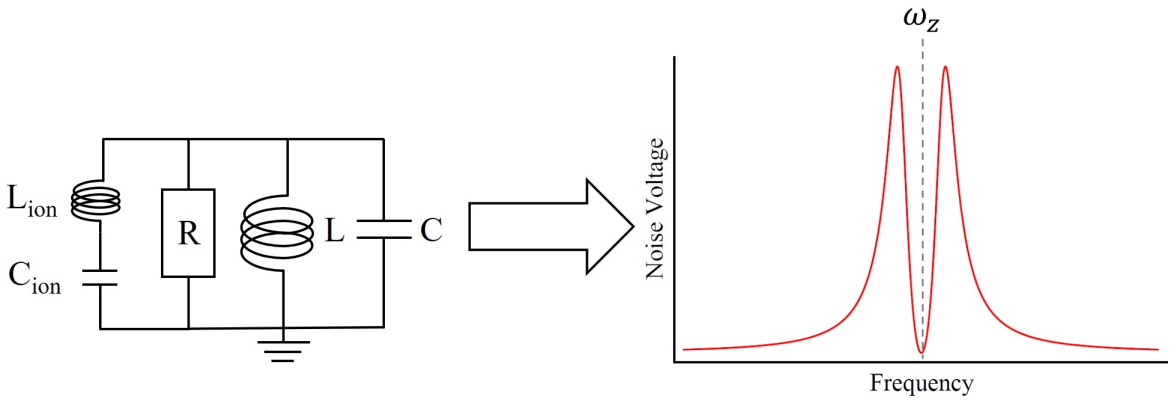

Figure 3.5: Left: Equivalent circuit of the trapped electron and helical resonator together. Right: Thermal noise voltage of the combined system with the electron's axial dip visible.

The width of the electron's axial dip (Δw_{Axial}) is inversely related to the cooling time constant, $\Delta w_{\text{Axial}} = 1/\tau_z$ [72]. Therefore, to be able to resolve the signal of a single electron the width of the dip needs to be wide enough to be observed on the FFT. As a result τ_z needs to be small, which in turn means that from equation 3.13, D^z_{eff} needs to minimised and $Re(Z(\omega))$ must be maximised. The minimisation D^z_{eff} has already been discussed. On resonance, the resonator's impedance $Re(Z(\omega)) = R_p$ and R_p is dependent upon the resonator's Q-factor (Q)[75]

$$R_p = \omega_{LC} L Q. \tag{3.15}$$

The Q-factor is a measure of the rate of energy loss in a resonator, with a higher Q-factor meaning that oscillations take longer to die out. The practical steps taken to maximise our resonator's Q-factor are discussed in chapter 6.

In summary, to detect and efficiently cool the electron's axial motion the pickup electrode must be carefully chosen to minimise the effective coupling distance and the chosen electrode must be connected to a high Q resonator which resonates at $\omega_{LC} = \omega_z$. For the electron's axial signal to pass from the chip to the resonator and then on to the amplifier, the resonator must be capacitively coupled to both the chip and the amplifier. The next section details the steps taken to choose the values of these capacitors and the loading effect that the chip has on the resonator.

3.2 Microwave Network Analysis Of The Detection System

When analysing low frequency circuits the components are small compared with the signal wavelength, which means that the circuit can be represented by lumped components and analysed with basic circuit theory. However, these techniques cannot be directly applied to high frequency circuits. Despite this, basic circuit theory can be extended using microwave network analysis which is simpler to apply than solving Maxwell's equations for every given situation [8]. This section uses microwave network analysis to optimise the design parameters of the detection system.

To optimise the detection system we must first identify the parameters that we wish to protect or maximise. We need:

- a helical resonator that resonates at the same frequency as the electron mode we are detecting.
- a voltage signal that is large enough to reach the cryogenic amplifier.
- an axial dip that is wide enough to be resolved on an FFT which has a resolution of 1 Hz.

3.2.1 Lumped Element Model Of The Detection System

The helical resonator is capacitively coupled to both the chip and the cryogenic amplifier which means that the parasitic capacitance of the chip and the input capacitance of the amplifier appear in parallel with the resonator (figure 3.6). These capacitances load the resonator and reduce its resonance frequency and as a result its Q-factor [76, 77]

$$Q_{\text{exp}} = Q_0 \sqrt{\frac{\omega_{\text{exp}}}{\omega_0}}, \tag{3.16}$$

where Q_0 and ω_0 are the unloaded Q-factor and resonance frequency and Q_{exp} and ω_{exp} are the corresponding values of the loaded resonator.

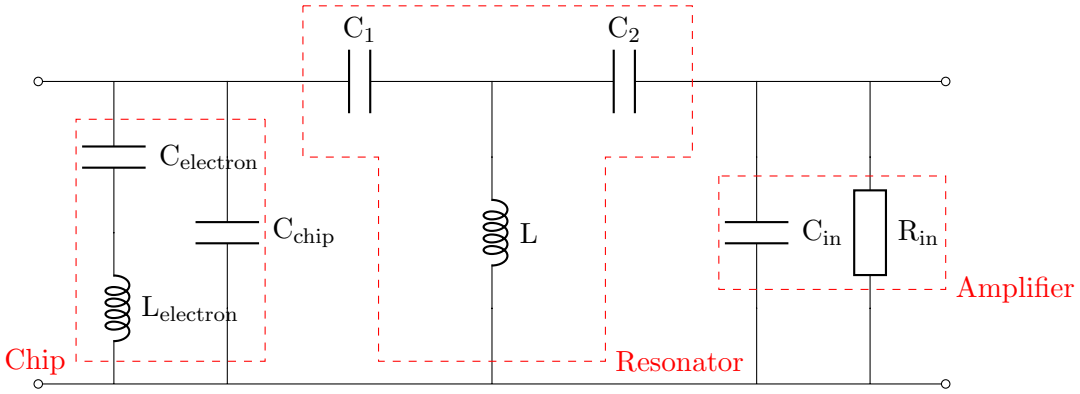

Figure 3.6: Lumped element model of the detection system which has been split into three sections; the chip, the resonator and the amplifier. C_1 and C_2 are coupling capacitors whose values can be optimised to prevent the chip and amplifier from the loading the resonator.

Reduction of the Q-factor would, from equation 3.15, reduce the resonator's impedance (R_p) and as a result the induced voltage passed to the amplifier and the width of the axial dip. Therefore, the best values for the coupling capacitors, C_1 and C_2, need to be investigated to minimise the loading effects of the chip and the amplifier on the resonator while keeping a good signal visible on the FFT.

Additionally, the voltage arriving at the gate of the amplifier's transistor needs to be maximised. The lumped element model of figure 3.6 can be considered as a black box (figure 3.7) allowing the focus to shift to the current and voltage at the input (Port 1) and output (Port 2) of the box.

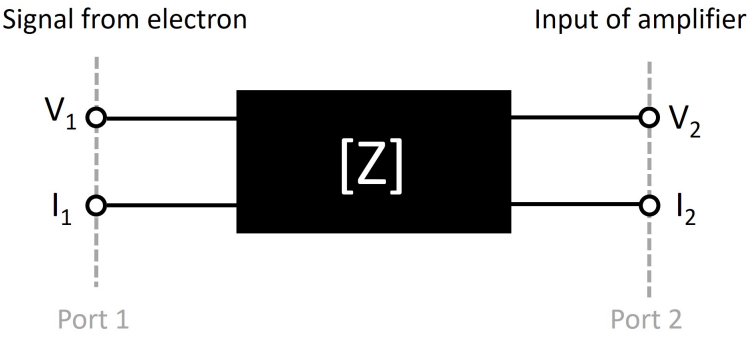

Figure 3.7: Treating the detection system as a black box which has two ports, the first at the position of the trapped electron and the second at the gate of the amplifier's transistor.

The box itself can be defined by an impedance matrix [Z] consisting of an input impedance, Z_{11}, an output impedance, Z_{22}, and the impedances between the ports, Z_{21} and

Z_{12}, where the order of the subscript denotes the direction of measurement. The voltages at port 1 (V_1) and port 2 (V_2) can be found from Ohm's law

$$\begin{pmatrix} V_1 \\ V_2 \end{pmatrix} = \begin{bmatrix} Z_{11} & Z_{12} \\ Z_{21} & Z_{22} \end{bmatrix} \begin{pmatrix} I_1 \\ I_2 \end{pmatrix}, \tag{3.17}$$

where I_1 is the current induced by the electron at port 1 and I_2 is the current input at port 2, the amplifier's gate. The cryogenic amplifier uses an Field Effect Transistor (FET) which means that $I_2 \approx 0$ [78]. Therefore, the signal delivered to the input of the transistor is

$$V_2 = Z_{21} I_1. \tag{3.18}$$

The voltage, V_1, provides the interaction between the electron and the coil and is therefore responsible for the resistive cooling of the electron's axial motion. From equation 3.17, $V_1 = I_1 Z_{11}$ meaning that the real part of Z_{11} provides the resistive cooling and as a result also controls the width of the axial dip

$$\Delta\omega_{\text{Axial}} = \frac{q^2}{m} \frac{1}{D_{\text{eff}}^2} \cdot \text{Re}(Z_{11}), \tag{3.19}$$

Consequently, to increase the visibility of the electron the detection system must provide a large $Re(Z_{11})$ and to maximise the signal at the input of the amplifier, a large $Re(Z_{21})$.

3.2.2 Transmission Matrices Of The Detection System

In order to determine the effect that the coupling capacitors, C_1 and C_2, have on Z_{11}, Z_{21} and the resonance frequency of the helical resonator, the inside of the 'black box' of figure 3.7 now needs to be investigated. Here, the cryogenic detection system can be split into three distinct sections; the chip with the trapped electron, the resonator with the coupling capacitors and the input of the amplifier as shown in figure 3.6. Each section can be characterised by its own impedance matrix. However, as the entire system is a cascade of these three sections it is more convenient to describe each section using a transmission matrix, an [ABCD] matrix [8], as shown in figure 3.8.

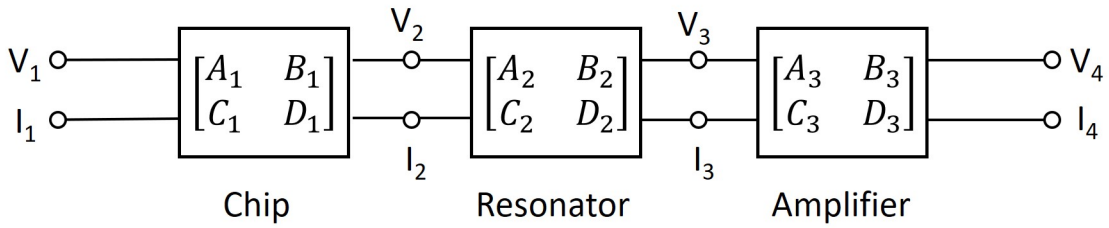

Figure 3.8: The cascade of ABCD transmission matrices that make up the cryogenic detection system.

The overall [ABCD] matrix of the system is then a multiplication of all of the individual sections' [ABCD] matrices

$$\begin{pmatrix} V_1 \\ I_1 \end{pmatrix} = \underbrace{\begin{bmatrix} A_1 & B_1 \\ C_1 & D_1 \end{bmatrix}}_{\text{Chip}} \underbrace{\begin{bmatrix} A_2 & B_2 \\ C_2 & D_2 \end{bmatrix}}_{\text{Resonator}} \underbrace{\begin{bmatrix} A_3 & B_3 \\ C_3 & D_3 \end{bmatrix}}_{\text{Amplifier}} \begin{pmatrix} V_4 \\ I_4 \end{pmatrix} \tag{3.20}$$

$$\begin{pmatrix} V_1 \\ I_1 \end{pmatrix} = \underbrace{\begin{bmatrix} A & B \\ C & D \end{bmatrix}}_{\text{Overall}} \begin{pmatrix} V_4 \\ I_4 \end{pmatrix} \tag{3.21}$$

The [ABCD] matrices of common two port systems are well known and the two networks needed in this analysis are the shunt admittance and T-Network which are both shown in figure 3.9.

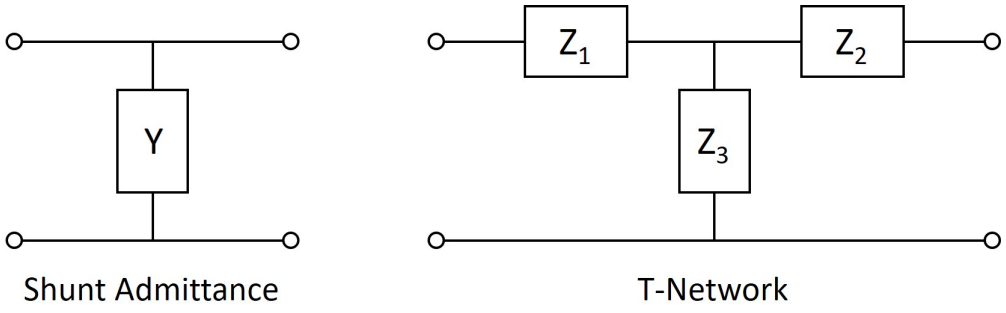

Figure 3.9: Two common two port networks; left - shunt admittance, right - T-Network.

The [ABCD] matrices for these two networks are [8]

$$[\text{ABCD}]_{\text{shunt}} = \begin{bmatrix} 1 & 0 \\ Y & 1 \end{bmatrix} \quad \text{and} \quad [\text{ABCD}]_{\text{T-Network}} = \begin{bmatrix} 1 + \frac{Z_1}{Z_3} & Z_1 + Z_2 + \frac{Z_1 Z_2}{Z_3} \\ \frac{1}{Z_3} & 1 + \frac{Z_2}{Z_3} \end{bmatrix}$$

The red dashed boxes in figure 3.6 show that the chip and the amplifier both follow the shunt admittance network in figure 3.9. Remembering that $Y = Z^{-1}$ their [ABCD] matrices can be given by

$$[\text{ABCD}]_{\text{chip}} = \begin{bmatrix} 1 & 0 \\ \frac{1}{Z_{\text{Chip}}} & 1 \end{bmatrix} \quad \text{and} \quad [\text{ABCD}]_{\text{amplifier}} = \begin{bmatrix} 1 & 0 \\ \frac{1}{Z_{\text{Amplifier}}} & 1 \end{bmatrix},$$

where $Z_{\text{Chip}} = \frac{1}{j\omega}\left(\frac{C_{\text{electron}}}{1-\omega^2 L_{\text{electron}} C_{\text{electron}}} + C_{\text{chip}}\right)^{-1}$ and $Z_{\text{Amplifier}} = \left[j\omega C_{\text{in}} + \frac{1}{R_{\text{in}}}\right]^{-1}$. Likewise, the resonator and coupling capacitors form a T-Network and therefore have an [ABCD] matrix of

$$[\text{ABCD}]_{\text{Resonator}} = \begin{bmatrix} 1 + \frac{Z_{\text{C}_1}}{Z_{\text{Coil}}} & Z_{\text{C}_1} + Z_2 + \frac{Z_{\text{C}_1} Z_{\text{C}_2}}{Z_{\text{Coil}}} \\ \frac{1}{Z_{\text{Coil}}} & 1 + \frac{Z_{\text{C}_2}}{Z_{\text{Coil}}} \end{bmatrix},$$

where $Z_{\text{coil}} = \left(\frac{1}{R_{\text{coil}}} + \frac{1}{j\omega L_{\text{coil}}} + j\omega C_{\text{coil}}\right)^{-1}$, $Z_{\text{C}_1} = \frac{1}{j\omega C_1}$ and $Z_{\text{C}_2} = \frac{1}{j]\omega C_2}$. The overall [ABCD] matrix (= $[\text{ABCD}]_{\text{chip}}[\text{ABCD}]_{\text{Resonator}}[\text{ABCD}]_{\text{amplifier}}$) is then transformed to [Z] using [8]

$$\begin{bmatrix} Z_{11} & Z_{12} \\ Z_{21} & Z_{22} \end{bmatrix} = \begin{bmatrix} \frac{A}{C} & \frac{AD-BC}{C} \\ \frac{1}{C} & \frac{D}{C} \end{bmatrix} \tag{3.22}$$

Once the overall [Z] matrix is known analytically the values of C_1 and C_2 can be varied to study their effect on the Q-factor and resonance frequency of the resonator, the size of the voltage reaching the cryogenic amplifier and the width of the axial dip. The results of which can be seen in the next section.

3.2.3 Results Of The Microwave Network Analysis

For all of the plots in this section the electron's axial frequency is set to be equal to the unloaded resonance frequency of the helical resonator (47.5 MHz). The electron's inductance is calculated from $L^z_{\text{electron}} = m\frac{(D^z_{\text{eff}})^2}{q^2}$ with D^z_{eff} set to that of the correction electrode ($D^z_{\text{eff, corr.}} = 2.08$ mm). The electron's capacitance is then calculated from its inductance and axial frequency using $\omega_z = \frac{1}{\sqrt{C^z_{\text{electron}} L^z_{\text{electron}}}}$. The impedance of the coil is calculated from the measured inductance value of the helical resonator (1.1 μH) manufactured for this experiment and its unloaded Q-factor measured at 4 K (34,100 $\pm$ 400), both of which are presented in chapter 6. The parasitic capacitance of the chip is set to the measured value of the capacitance between the correction electrode and ground (43.7 $\pm$ 0.3 pF), which is detailed in chapter 4. In each section two plots are presented, one where the

value of C_1 is fixed (to 30 pF) and C_2 is varied and one where the opposite case is true. From here on C_1 is referred to as the the coupling to the chip and C_2 is referred to as the coupling to the amplifier.

Resonance Frequency Of The Helical Resonator

Figure 3.10 shows how the resonance frequency ($\omega_{LC} = 2\pi\nu_{LC}$) of the helical resonator changes with the coupling capacitances. The coupling to the amplifier has a minor effect on the resonance frequency and can be considered insignificant but the coupling to the chip clearly has much more of an effect. The higher the capacitive coupling to the chip, the quicker the frequency reduces. However, once the capacitance is above 250 pF the resonance frequency levels off and only decreases very slightly with increasing capacitance. The value of the capacitor between the chip and the resonator should be carefully chosen so that the chip does not unduly load the resonator and reduce its resonance frequency to an unusable value.

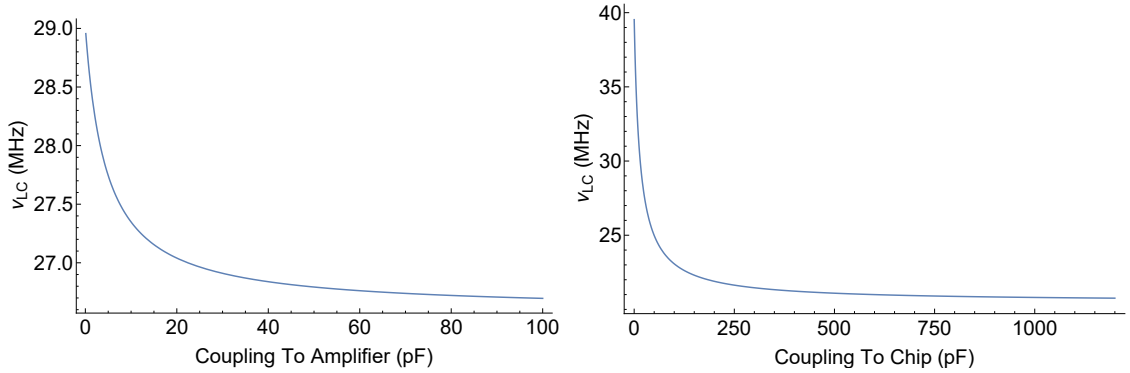

Figure 3.10: Effect of the coupling capacitors, C_1 (coupling to the chip) and C_2 (coupling to the amplifier), on the resonance frequency of the helical resonator. Left: Coupling to the chip is fixed at 30 pF whilst coupling to the amplifier is varied. Right: Coupling to the amplifier is fixed at 30 pF whilst coupling to the chip is varied.

Q-Factor Of The Helical Resonator

If the resonance frequency decreases then the quality factor of the coil also drops according to equation 3.16. Figure 3.11 shows the resulting decrease in Q-factor with the increasing coupling capacitors. As expected the coupling to the chip has a more prevalent effect on reducing the Q-factor.

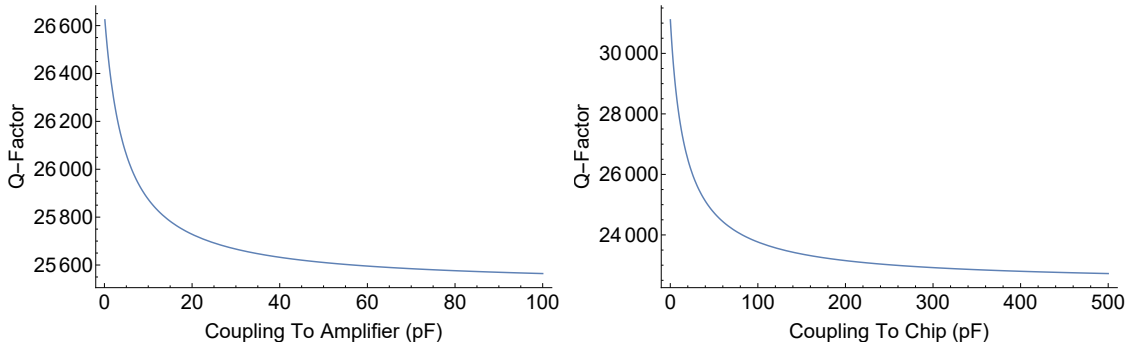

Figure 3.11: Effect of the coupling capacitors on the Q-factor of the helical resonator. Left: Coupling to the chip is fixed at 30 pF whilst coupling to the amplifier is varied. Right: Coupling to the amplifier is fixed at 30 pF whilst coupling to the chip is varied.

Voltage Signal Of The Electron

As explained in equation 3.18 the voltage signal which reaches the input of the amplifier depends upon the Z_{21} impedance value of the system. Z_{21} needs to be kept high to maintain a high signal to noise ratio. Figure 3.12 shows that increasing the coupling to both the amplifier and the chip maximises the value of $Re(Z_{21})$. Therefore, using high value capacitors either side of the resonator would achieve the maximum voltage signal.

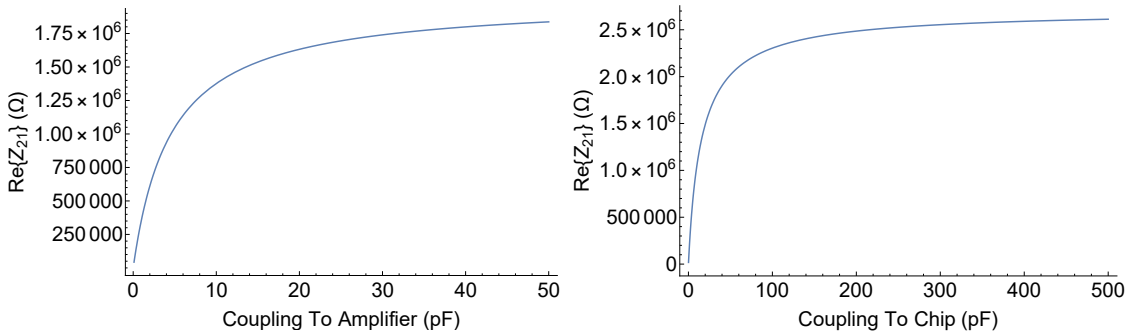

Figure 3.12: Effect of the coupling capacitors on $Re(Z_{21})$ of the detection system. Left: Coupling to the chip is fixed at 30 pF whilst coupling to the amplifier is varied. Right: Coupling to the amplifier is fixed at 30 pF whilst coupling to the chip is varied.

Width Of The Axial Dip

Equation 3.19 showed that the width of the axial dip of the electron is linearly dependent upon $Re(Z_{11})$. Figure 3.13 shows how the real part of Z_{11} changes with the two coupling capacitors. It is clear that Z_{11} slowly decreases with an increased coupling to the amplifier but increases quickly with an increased coupling capacitor to the chip. Therefore, to maintain a large $Re(Z_{11})$ a large coupling capacitor to the chip should be used.

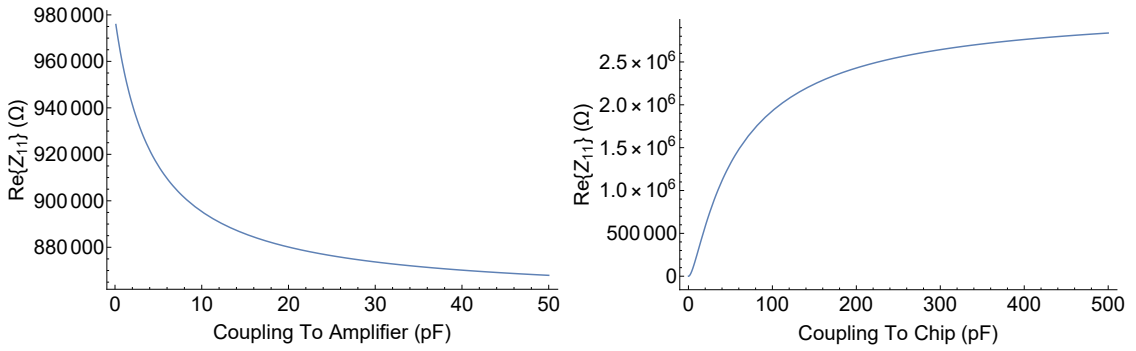

Figure 3.13: Effect of the coupling capacitors on $Re(Z_{11})$ of the detection system. Left: Coupling to the chip is fixed at 30 pF whilst coupling to the amplifier is varied. Right: Coupling to the amplifier is fixed at 30 pF whilst coupling to the chip is varied.

Finally, the expected width of the electron dip can be seen in figure 3.14. Again, the coupling to the amplifier plays a minor role but the width of the dip increases with the coupling to the chip making the signal from one electron easier to resolve.

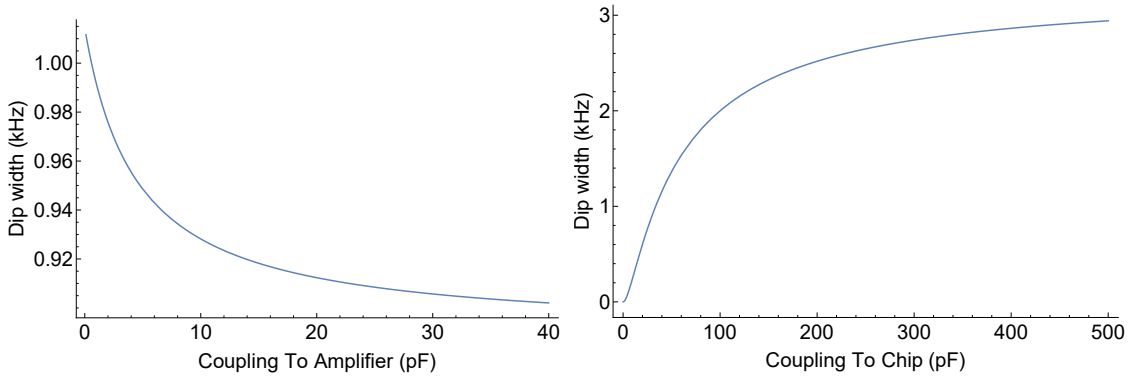

Figure 3.14: Effect of the coupling capacitors on the width of the axial electron dip. Left: Coupling to the chip is fixed at 30 pF whilst coupling to the amplifier is varied. Right: Coupling to the amplifier is fixed at 30 pF whilst coupling to the chip is varied.

Conclusion

In conclusion, although the Q-factor and the resonance frequency of the helical resonator will decrease, large coupling capacitors of ≥ 250 pF should be used on either side of the resonator. Although the coupling to the chip is not investigated above 100 pF it is clear from the plateaus in the plots that capacitances higher than 100 pF will have little effect. Additionally, choosing both capacitors to be the same value means that physically only one capacitor is required at the top of the coil. The capacitor will maximise not only Z_{11} and as a result widen the axial dip, but also Z_{21}, ensuring that the maximum possible voltage reaches the amplifier.

3.2.4 Final Considerations

To connect the Geonium chip to the resonator a short cable is required. This cable is outside of the on-chip vacuum chamber (introduced in section 2.2 and described in more detail in section 4.5) and should therefore be shielded against noise. To achieve this a coaxial cable is used rather than just a simple copper wire. However, the length of any coaxial cables connected to the resonator will affect its resonance. Using the model in figure 3.15 this can be theoretically explained by multiplying the [ABCD] matrix for a coaxial line [8] with that of a coil to give

$$[ABCD]_{\text{Total}} = \begin{bmatrix} \cosh(\gamma L_{\text{coax}}) & Z_0 \sinh(\gamma L_{\text{coax}}) \\ \frac{1}{Z_0}\sinh(\gamma L_{\text{coax}}) & \cosh(\gamma L_{\text{coax}}) \end{bmatrix} \begin{bmatrix} 1 & 0 \\ \frac{1}{Z_{\text{coil}}} & 1 \end{bmatrix},$$

where L_{coax} is the length of the line, Z_0 is its characteristic impedance and γ is its propagation constant. γ is a complex value whose real part quantifies the losses in the conductors and dielectric, while the imaginary part contains its inductance and capacitance per unit length [8].

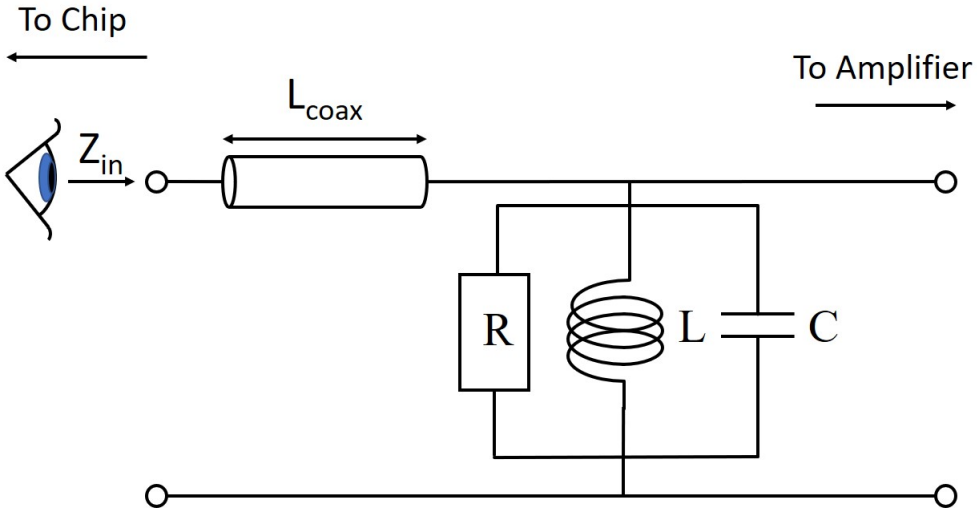

Figure 3.15: Simple model to investigate the effect that a coaxial cable of length L_{coax} can have on a helical resonator modelled as a parallel LCR circuit.

Transforming the above [ABCD] matrix to a [Z] matrix gives the impedance seen at the input to the coaxial cable (Z_{11} of the [Z] matrix)

$$Z_{\text{in}}(\omega) = \frac{Z_0(Z_{\text{coil}}(\omega)\coth(\gamma L_{\text{coax}}) + Z_0)}{Z_0\coth(\gamma L_{\text{coax}}) + Z_{\text{coil}}(\omega)}. \tag{3.23}$$

Figure 3.16 shows how the resonance frequency and the real part of the impedance of the helical resonator change with three different lengths of coaxial line where the ca-

pacitance per unit length was chosen to be similar to known values of cryogenic coaxial cables[1]. The resonance frequency is reduced dramatically as the length of the coaxial line increases. The reductions in Q and resonance resistance are caused by losses in the real part of the propagation constant. As this resonance resistance will be presented to the electron this will also reduce the induced voltage which is passed to the amplifier.

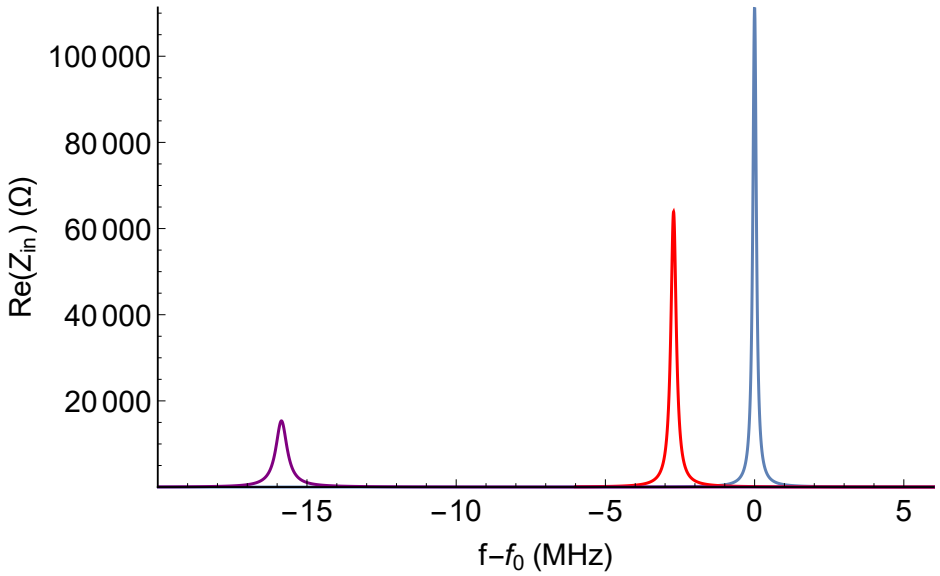

Figure 3.16: The effects of different lengths of coaxial cable on the helical resonator's Q-factor, resistance presented to the electron (Z_{in}) and resonance frequency where $f - f_0$ gives the shift of the resonance frequency from its original unloaded frequency. The lengths of the coaxial cable are; 0cm (blue), 1cm (red) and 10cm (purple).

To reduce these losses, short coaxial cables with low conductor surface resistance and low dielectric losses should be used. Therefore, we have manufactured a superconducting transmission line from single core niobium titanium wire, which can be seen in section 6.4.

3.3 Requirements For Detection

This chapter has introduced the necessary requirements for detection of a trapped electron using the Geonium Chip. To summarise, the requirements are:

- A helical resonator which blocks the effect of the output capacitance of the chip, resonates at the same frequency as the electron and provides a high impedance on resonance.
- A pick-up electrode with a small effective coupling distance.

[1] Allectra 50 Ω coaxial kapton cables with 115 pF/m

- A large coupling capacitor between the chip and the resonator to maximise both the signal to noise ratio and the visibility of the electron dip.
- A large coupling capacitor between the resonator and the amplifier to maximise the voltage passed to the input of the amplifier.
- A short superconducting transmission line between the chip and the resonator that has a minimal effect on the resonator and shields the signal against noise.

All of these criteria will be implemented in our experiment as described in the following chapters.

Chapter 4

The Geonium Chip

Chapter 2 has introduced the Geonium Chip as a series of five central electrodes with two side electrodes surrounded by a large ground plane as seen in figure 2.2. This design has a series of manufacturing requirements that are necessary to maintain a harmonic trapping potential. The electrodes must be symmetric and their dimensions must not differ from those used in the calculation of the harmonic trapping potential [4]. Additionally, the gaps between the electrodes must be small enough to prevent charge accumulation on the underlying dielectric. Any charge accumulated in the gaps would modify the electrostatic potential [36]. However, these charges can be screened by the metallic surface of the electrodes. This screening factor grows exponentially with the aspect ratio between the depth of the gap and its width [36]. The metallic surface of the chip must also be as smooth as possible to prevent patch potentials from forming and again modifying the trap's electrostatic potential. Finally, as stated in chapter 3 the parasitic capacitances of the chip need to be small so that they can be tuned out by the detection system. If the capacitances are too large then it will be impossible to measure the electron's axial frequency. All of these requirements lead towards the decision to manufacture the Geonium Chip using microfabrication techniques.

This chapter will detail the fabrication of the first generation Geonium Chip before focussing on its testing at high frequencies. The high frequency analysis is required to determine the chip's parasitic capacitances which have a direct effect on the performance of the detection system. As a result, two separate methods of connecting to the chip are explored in an attempt to reduce the parasitic capacitances seen by the detection system. This leads to a discussion of the limitations of the first generation Geonium Chip and the improvements that can be made in future iterations. Finally, the transmissivity of the chip is explored as a potential coupling mechanism for the cyclotron mode and the on-chip

vacuum chamber which doubles as a microwave cavity is discussed.

4.1 Microfabrication Of The First Generation Geonium Chip

Figure 4.1 shows a cross-section of the chip manufactured by MIR Enterprises[1] using standard microfabrication techniques. The materials and dimensions were chosen based upon numerous conversations between MIR Enterprises and the Geonium team, in particular J. Pinder. The design of the chip will be briefly discussed here but for more detail see [1].

The Geonium chip consists of:

- a metallisation layer which contains the electrodes and contact pads.
- buried wires which connect the pads to the electrodes by way of vias.
- insulating regions which isolate the buried wires from the electrodes.
- a substrate upon which the rest of the chip sits.

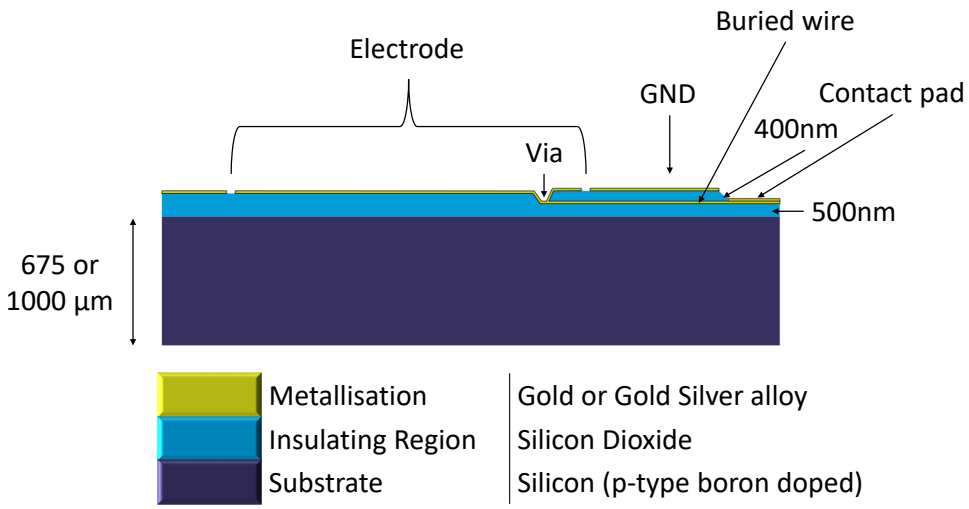

Figure 4.1: Cross-section of the Geonium Chip showing the thicknesses and materials used in each layer.

The first order of Geonium chips consisted of twenty separate chips with varying substrate thickness, metallisation thickness and metallisation purity. Sixteen chips were ordered with a substrate thickness of 675 μm so that the magnetic field source beneath

[1] http://mir-enterprises.com

the chip could be as close to the trapping region as possible. However, there was a concern about the fragility of a substrate this thin. Therefore, four chips with a substrate thickness of 1000 μm were also ordered as a fail safe. To date the thinner chips have not proven to be too fragile and have survived multiple thermal cycles from 300 K to 4 K and back again to room temperature without any observed cracking.

The metallisation layer was ordered in three different variations; 300 nm of pure gold, 300 nm of gold silver alloy and 100 nm of a gold silver alloy, both of which had a ratio of 80:20 respectively. The silver was added to the gold to increase its resistivity at 4 K and therefore increase its skin depth at microwave frequencies. This allows microwaves to pass through the chip and potentially couple to a transmission line beneath. As already discussed in chapter 2 the cyclotron frequency is in the GHz region meaning that the cyclotron motion could be detected directly through the chip. This would replace picking up the current the electron induces on the chip's electrodes or using an explicit antenna which could distort the electrostatic potential. This novel approach of using the transparency of the chip to microwaves, would simplify the detection electronics for the cyclotron mode. As a result, the extent to which the microwaves can pass through the chip was measured by J.Lacy and is discussed further in section 4.4.

The dimensions of the electrodes are chosen so that the optimal tuning ratio T_c^{opt} falls within a desired useful trapping interval. This interval is chosen to suit the intended application of the Geonium chip. For mass spectrometry, trapping intervals further from the surface of the chip may be required for larger molecules. Once the useful trapping interval has been chosen, the electrodes dimensions are calculated numerically and there may be more than one solution. The length of the compensation electrodes can then be varied to find an optimal solution where electrostatic anharmonicities are cancelled up to the sixth order [85].

The size of the electrodes remain the same on all of the chips (figure 4.2), regardless of substrate or metallisation layer. The gaps between the electrodes were chosen to be as small as possible whilst still ensuring that the breakdown voltage of the chip was much higher than the voltages required to trap the electron. The 10 μm gaps allow 30 V between the electrodes (in air) before breakdown occurs and upwards of 150 V in vacuum [1].

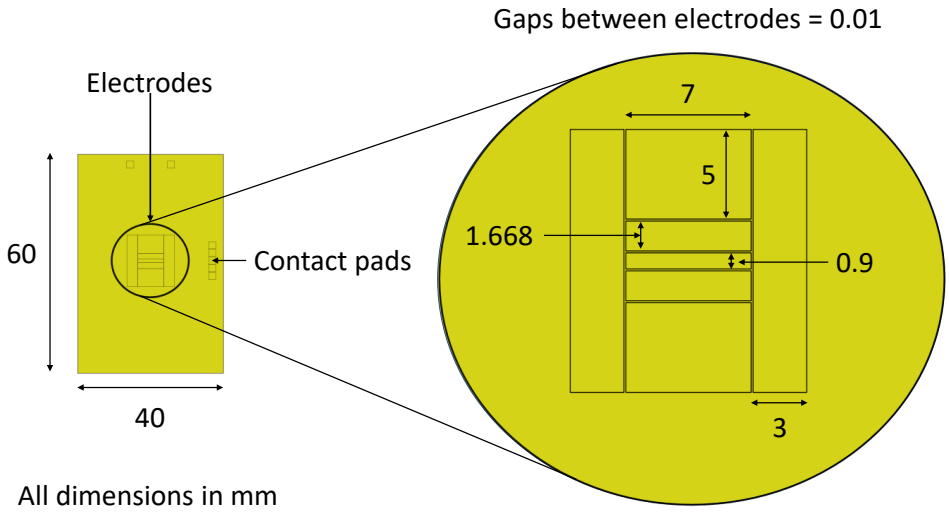

Figure 4.2: Electrode dimensions of the first generation Geonium Chip

The buried wires are tracks of pure gold that are 3 μm wide and insulated by 400 nm of silicon dioxide. The ratio of the width to the insulating region could not be any smaller, otherwise connecting the vias to the wires would have become difficult and more likely to be subject to manufacturing defects. To ensure that the trapping potential above the surface of the chip was unaffected by the buried wires they were chosen to have a thickness of 100 nm. If they were any thicker then they would have deformed the surface of the chip and distorted the potential.

4.2 High Frequency Analysis Of The Geonium Chip

To determine the chip's parasitic capacitances the chip's response to RF and MW frequencies must be investigated. Section 3.2 has already introduced the idea of using network parameters to turn a complex system into a black box to simplify its investigation. However, this was purely a model with which to optimise the detection system and none of the network parameters were physically measured. To determine each component of a [Z] matrix Z_{ij} is found from [8]

$$Z_{ij} = \left.\frac{V_i}{I_j}\right|_{I_k=0 \text{ for } k\neq j}, \tag{4.1}$$

so in other words Z_{ij} is found by measuring the voltage at port i when port j is driven by current I_j and all the other ports of the system are open-circuited. Likewise, the

components of the [Y] matrix are found by measuring [8]

$$Y_{ij} = \left.\frac{I_i}{V_j}\right|_{V_k=0 \text{ for } k\neq j}, \tag{4.2}$$

which means measuring the current at port i when port j is driven by a voltage V_j and all the other ports are short-circuited. At RF and MW frequencies both short-circuits and open-circuits are hard to achieve. Open circuits are not ideal due to parasitic capacitances and radiation at these frequencies. Likewise, short-circuits are difficult due to finite inductance at high frequencies [79]. As a result, measuring either the [Z] or [Y] matrix becomes more and more difficult as the frequency rises. However, another set of network parameters known as the S-parameters can be easily measured at RF and MW frequencies. The scattering or S-parameters relate the voltage waves that enter the ports to those that are reflected back from them [80]. A component of the [S] matrix is measured using [8]

$$S_{ij} = \left.\frac{V_i^-}{V_j^+}\right|_{V_k^+=0 \text{ for } k\neq j}, \tag{4.3}$$

where V_i^- is the amplitude of the voltage wave reflected back from port i and V_j^+ is the amplitude of the voltage wave applied to port j whilst all other ports are terminated with matched impedance loads to prevent reflections from those ports. This makes S-parameters much easier to measure accurately at high frequencies than Z or Y-parameters. In the case of a two port system, such as that shown in figure 4.3, the [S] matrix is made of four components; S_{11} and S_{22} which are the reflection coefficients at the two ports and S_{12} and S_{21} which are the transmission coefficients.

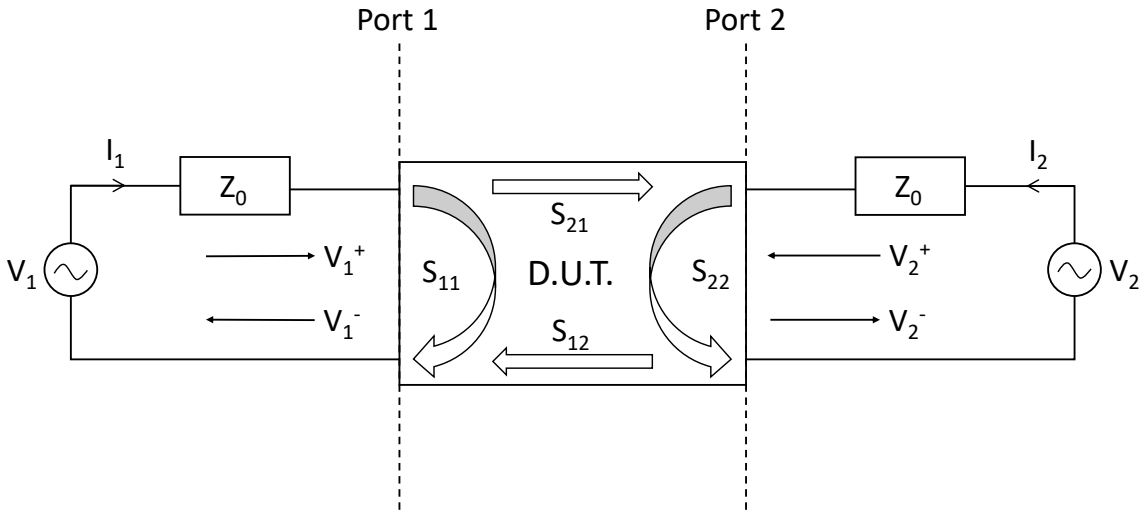

Figure 4.3: Schematic representation of the S-parameters of a device under test (D.U.T.) where the ports are terminated with the device's characteristic impedance (Z_0). Voltages with the superscript + are incident upon the ports and voltages with the superscript - are reflected back from the ports.

Each component of the [S] matrix is measured using

$$S_{11} = \frac{V_1^-}{V_1^+}\Big|_{V_2^+=0} \qquad S_{21} = \frac{V_2^-}{V_1^+}\Big|_{V_2^+=0}$$

$$S_{12} = \frac{V_1^-}{V_2^+}\Big|_{V_1^+=0} \qquad S_{22} = \frac{V_2^-}{V_2^+}\Big|_{V_1^+=0}$$

$$\begin{pmatrix} V_1^- \\ V_2^- \end{pmatrix} = \begin{bmatrix} S_{11} & S_{12} \\ S_{21} & S_{22} \end{bmatrix} \begin{pmatrix} V_1^+ \\ V_2^+ \end{pmatrix}$$

Once the [S] matrix has been measured it can be transformed to the more intuitive [Y] or [Z] matrices for further study. The measurement of the [S] matrix of the Geonium Chip is undertaken using a Vector Network Analyser (VNA) and the measurement setup is described in the next section.

4.2.1 Measuring The S-Parameters Of The Geonium Chip

Before the S-parameters of the Geonium Chip can be measured the chip's contact pads must be connected to the VNA, which is not a trivial process. Initially, it was thought

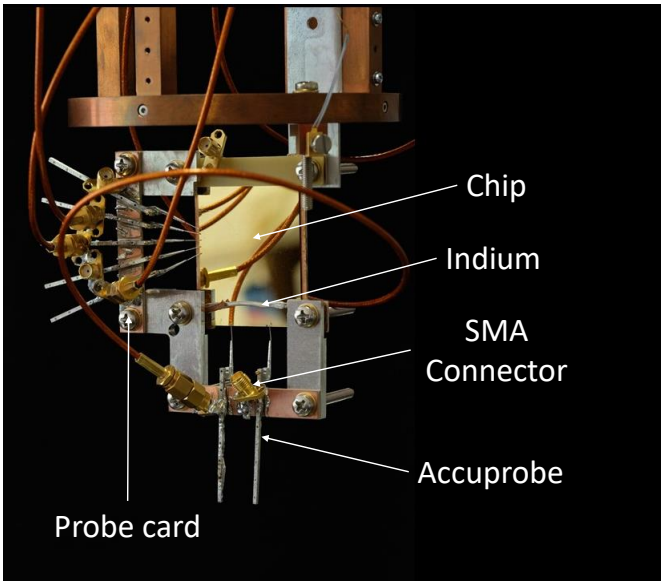

Figure 4.4: Wafer probe setup for measuring the high frequency response of the Geonium Chip. The ground plane of the chip is connected to the ground plane of the probe card using indium wire compressed between the probe card holder and the surface of the chip.

that the metallisation layer on the surface of the chip was too thin to survive the standard wire bonding technique, which requires a minimum pad thickness of 300 nm [81], so the first attempt to contact the chip was made using height adjustable wafer probes[2]. These probes were soldered to a supporting probe card and then positioned so that the tip of the probe touched the surface of the chip's contact pads, as shown in figure 4.4. This contacting technique is non-permanent, making it more flexible, but also sub-optimal as the wafer probes were designed for DC connections and therefore will be subject to parasitic inductances and capacitances at higher frequencies. There are probes that are designed for operation at higher frequencies[3] but these have a much higher capital outlay and, while they may be considered for use in the future, they are not used in the following measurements.

Later work with this wafer probe contact technique raised concerns that when cooled to cryogenic temperatures the probes may contract and lift from the surface of the chip. Therefore, wire bonding was also attempted as an alternative method of connecting to the chip's contact pads. The process was successful using a wedge-bond ultrasonic wire bonder at room temperature with aluminium wire of 25.4 μm diameter. Figure 4.5 shows

[2] Accuprobe Inc Z-Adjustable Probes
[3] Cascade Microtech - Cryogenic Probes for RF

the chip wire bonded to a single sided circuit board with the SMA connectors required to connect to the VNA.

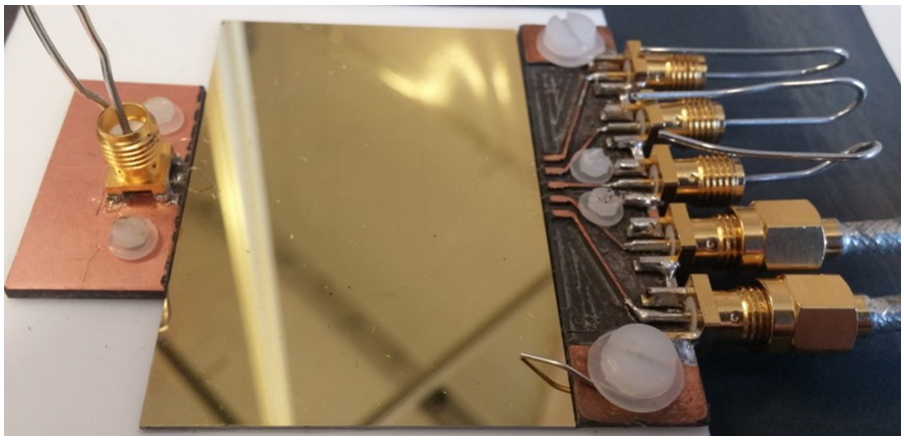

Figure 4.5: Wire bonded setup for contacting the Geonium Chip where the wire bonds are visible on the right hand side and the chip's electrodes are visible in the centre.

The high frequency response of the Geonium Chip alone is impossible to measure directly. It must always be coupled to a contacting system which allows the VNA to measure the S-parameters. Therefore, all the following measurements of the S-parameters include the Geonium Chip and either a wafer probe contact system (figure 4.4) or a wire bonded contact system (figure 4.5). The results for both systems are stated in sections 4.2.3 and 4.2.4.

Prior to obtaining the S-parameters the VNA was calibrated using a full 2-port calibration over the frequency range 2 MHz to 1.8 GHz using 3001 datapoints. The VNA was then connected to each setup using high quality cables[4] and the real and imaginary parts of the S-parameters were measured.

4.2.2 Data Analysis Of The High Frequency Response Of The Geonium Chip

Once the S-parameters have been measured the first analysis undertaken was to investigate whether the chip was reciprocal. A network is reciprocal if a voltage measured at port 1 caused by a current applied at port 2 is the same as the voltage measured at port 2 when the same current is applied at port 1. This is the reciprocity principle and is true for any passive network, i.e. a network that does not include any magnetically biased components like ferrites or any active devices such as an amplifier [82]. Therefore, if the chip's response is reciprocal, i.e. $S_{21} = S_{12}$, then it can be modelled by a series of passive components. A

[4] Allectra semi-rigid cables valid to 18 GHz

comparison of the chip's S_{21} and S_{12} for both the wafer probe setup and the wire bonded setup can be seen in figure 4.6.

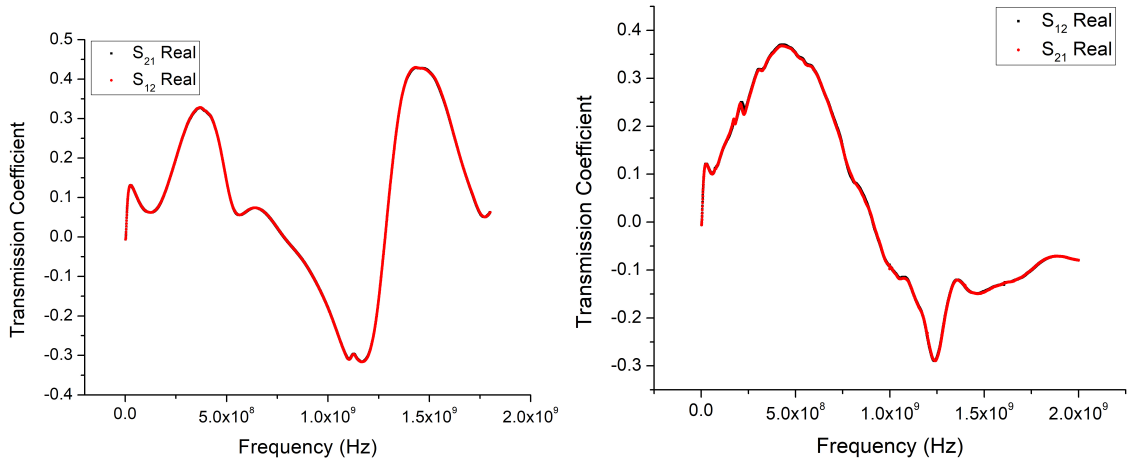

(a) Wafer probe setup (b) Wire bonded setup

Figure 4.6: Transmission coefficients, S_{21} and S_{12}, where port one is the right endcap and port two is the right compensation electrode. Left is the wafer probe and right is the wire bonded setup.

Figure 4.6 shows that S_{21} and S_{12} are equal for both the wafer probe setup and the wire bonded setup. Therefore, the chip is reciprocal in nature and can be modelled by a series of passive components. Using the reciprocity principle, all passive linear networks can either be modelled as a T-Network using Z-parameters or as a π-Network using Y-parameters, as shown in figure 4.7 [8].

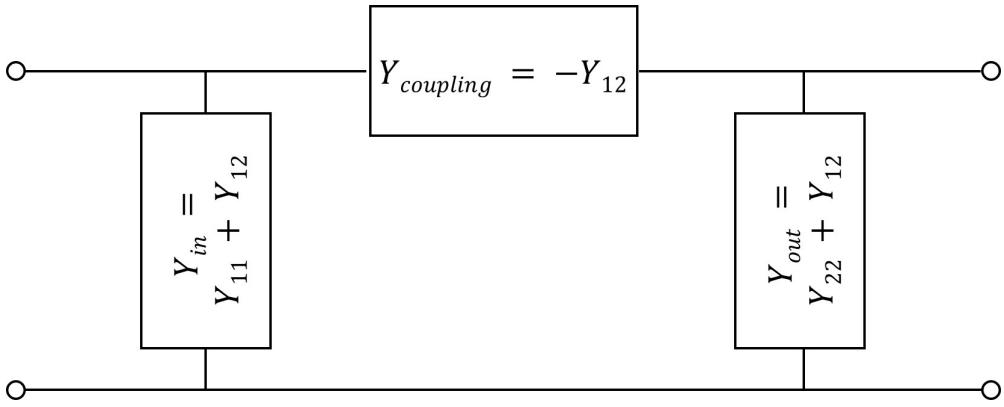

Figure 4.7: π-network model which can be used to represent reciprocal networks like the Geonium Chip [8]

To investigate whether the π-network was suitable for the Geonium Chip the S-parameters were transformed to admittance (Y) parameters using the equations 4.4. An

in-house python program was written to complete the conversion due to the large number of datapoints. The values for Y_{in} and Y_{out} were then calculated using the expressions in figure 4.7.

$$[Y] = \begin{bmatrix} Y_{11} & Y_{12} \\ Y_{21} & Y_{22} \end{bmatrix} \quad \text{Admittance Matrix} \tag{4.4}$$

$$Y_{11} = Y_0 \frac{(1 - S_{11})(1 + S_{22}) + S_{12}S_{21}}{(1 + S_{11})(1 + S_{22}) - S_{12}S_{21}}$$

$$Y_{12} = Y_0 \frac{-2S_{12}}{(1 + S_{11})(1 + S_{22}) - S_{12}S_{21}}$$

$$Y_{21} = Y_0 \frac{-2S_{21}}{(1 + S_{11})(1 + S_{22}) - S_{12}S_{21}}$$

$$Y_{22} = Y_0 \frac{(1 + S_{11})(1 - S_{22}) + S_{12}S_{21}}{(1 + S_{11})(1 + S_{22}) - S_{12}S_{21}}$$

where $Y_0 = \frac{1}{Z_0}$ and Z_0 is the characteristic impedance of the coaxial cables (50 Ω).

The following analysis focusses on the Y-parameters for one set of electrodes, where port one is set as the right endcap and port two is set as the right compensation electrode. Figure 4.8 shows the real and imaginary parts of Y_{in} for the wafer probe setup and Y_{out} has a very similar profile. The task now is to determine which combination of passive components produces this admittance profile.

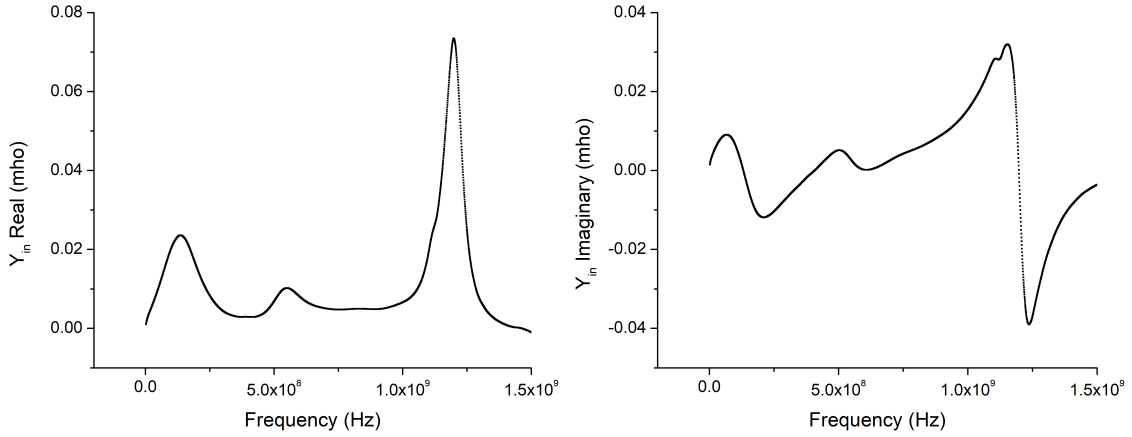

(a) Y_{in} Real (b) Y_{in} Imaginary

Figure 4.8: Y_{in} parameters of the Geonium chip where the input port was set to the right endcap and the output port was set to the right compensation electrode.

The peaks in the plot of the real part of Y_{in} appear at the same frequency as the points where the imaginary part of Y_{in} crosses the zero on the y-axis, implying that they are three distinct resonances. There are losses in the system so the resonances cannot be modelled using ideal components. Therefore, they must be modelled with 'real' components that

include losses and parasitic elements. Figure 4.9 shows the parasitics included in the models of a 'real' capacitor and inductor [9]. The capacitor model includes any inductance between the plates and leads (L), an insulation resistance (R_p) and a series resistance (R_s), which models the losses in the system. The inductor model includes the wire resistance (R_s) and a distributed capacitance (C_d).

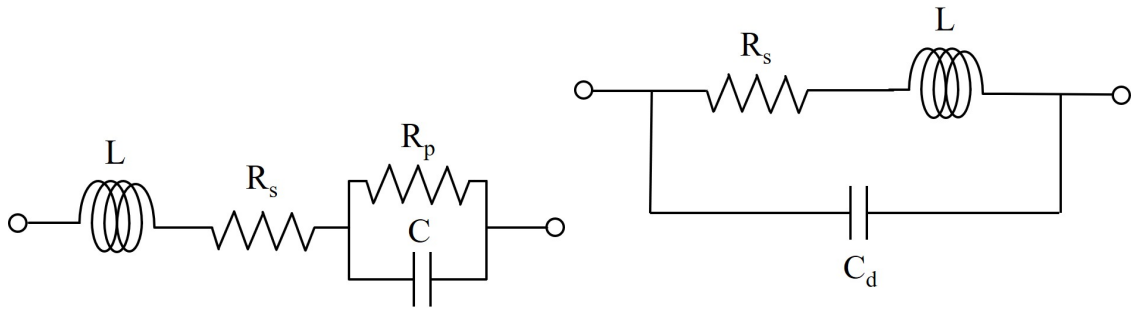

(a) Equivalent circuit of a 'real' capacitor (b) Equivalent circuit of a 'real' inductor

Figure 4.9: Equivalent circuits for how a capacitor and inductor appear at RF frequencies [9].

To discern which passive components could have produced the Y_{in} response of the chip, three possible combinations of 'real' capacitors and inductors, that could feasibly exist in the chip, were considered. These are explored in the next few sections.

Two Capacitors In Series

The first model considered is that of two 'real' capacitors connected in series, as shown in figure 4.10.

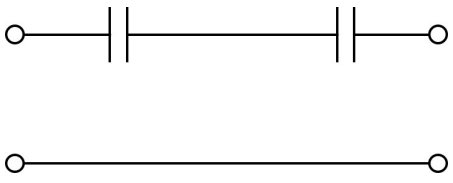

Figure 4.10: Model of two 'real' capacitors connected in series

This model gives the admittances seen in figure 4.11. Here, only one combined resonance is seen rather than two separate resonances, one for each capacitor. This is therefore not a suitable model for Y_{in} which shows a series of resonances.

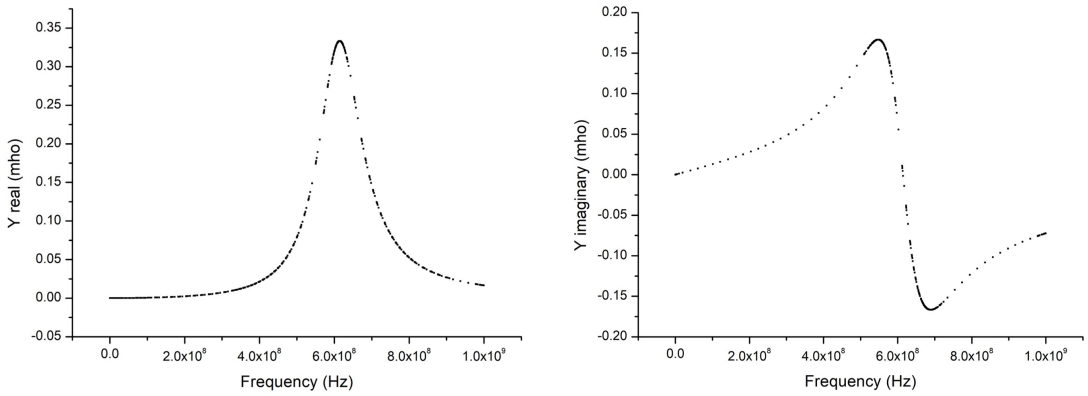

(a) Real component (b) Imaginary component

Figure 4.11: The admittance of two 'real' capacitors connected in series

Inductor And Capacitor In Series

The second model considered is that of a 'real' inductor in series with a 'real' capacitor, as shown in figure 4.12.

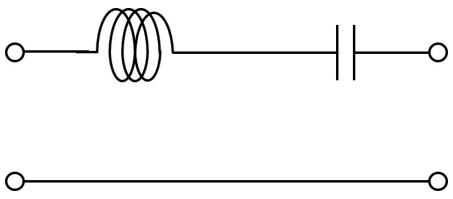

Figure 4.12: Model of an 'real' inductor in series with a 'real' capacitor

This model does give two resonance peaks in the admittance plots in figure 4.13. However, they are not the separately distinct peaks seen in Y_{in} and cannot therefore describe the response of the chip.

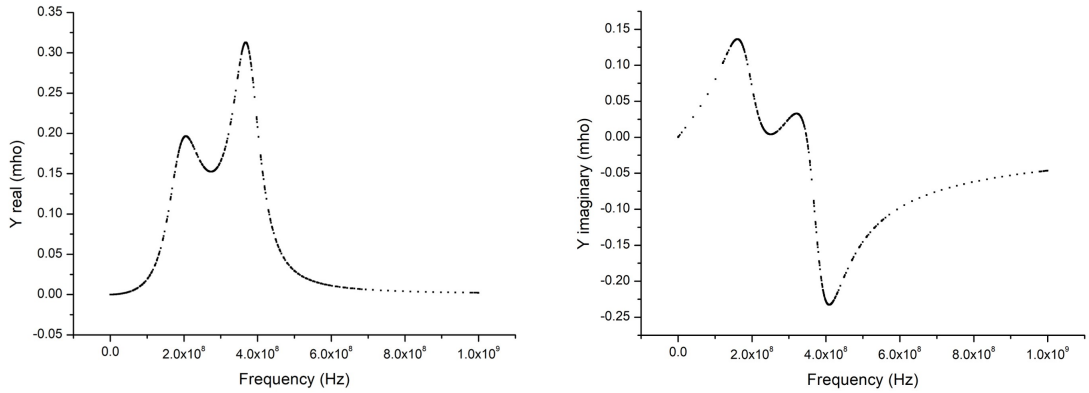

(a) Real component (b) Imaginary component

Figure 4.13: The admittance of a 'real' inductor connected in series with a 'real' capacitor

Two Capacitors In Parallel

The final model considered is that of two 'real' capacitors connected in parallel as shown in figure 4.14.

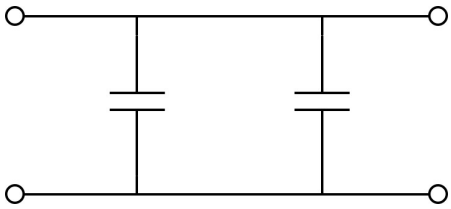

Figure 4.14: Model of two capacitors connected in parallel

This model gives two distinct resonances, as seen in figure 4.15, which match the resonance pattern seen in the admittance plot of Y_{in}.

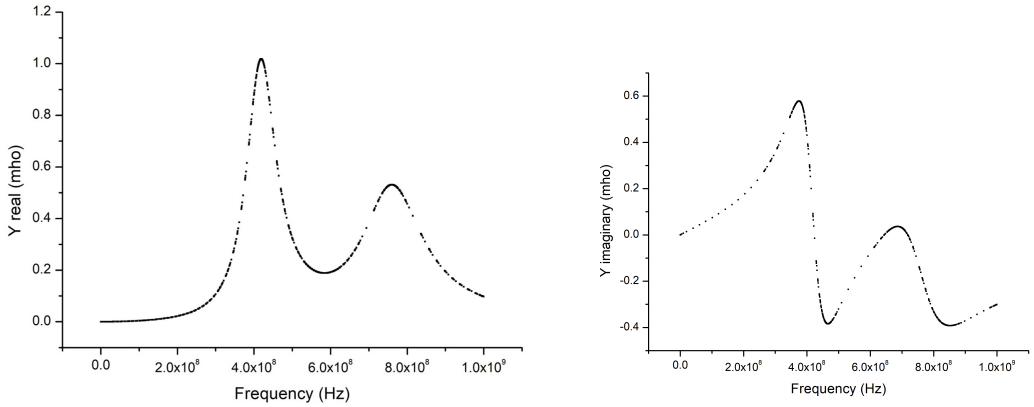

(a) Real component

(b) Imaginary component

Figure 4.15: Admittance of two 'real' capacitors connected in parallel

However, over the frequency range of interest Y_{in} had three distinct resonances so the model that will be used to investigate Y_{in} is that of three 'real' capacitors in parallel. Y_{out} has the same admittance profile so it can also be modelled by three 'real' capacitors. This leaves $Y_{coupling}$ to be investigated. The π-network model gives $Y_{coupling}$ as equal to $-Y_{12}$ which is plotted in figure 4.16a.

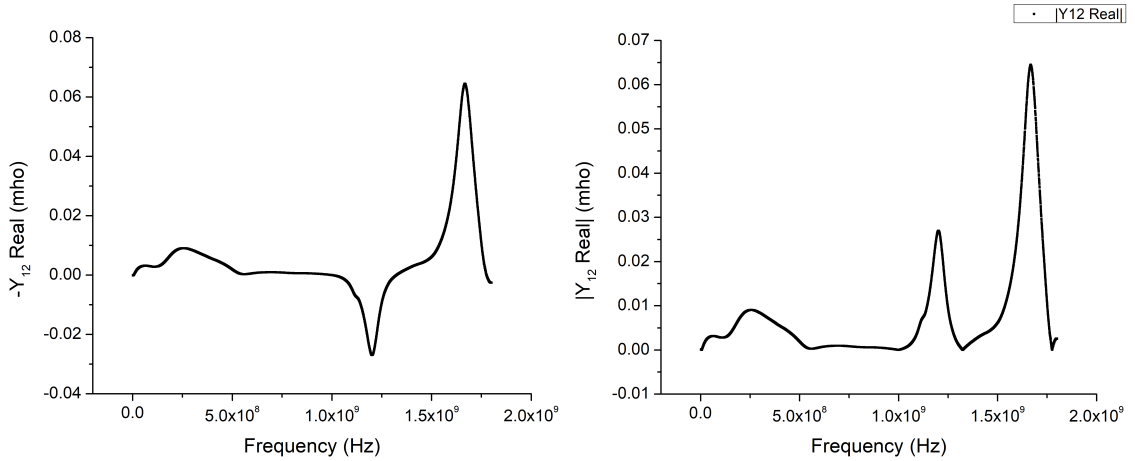

(a) $-Y_{12}$ Real (b) Absolute Y_{12} Real

Figure 4.16: Comparison of $-Y_{12}$ and absolute Y_{12} where port one is the right endcap and port two is the right compensation electrode.

Plotting -Y_{12} does not appear to follow the capacitor model of Y_{in} and Y_{out}. However, the absolute value can be taken to recover the expected admittance of three capacitors connected in parallel. Now Y_{in}, Y_{out} and $Y_{coupling}$ can all be fitted with the admittance of three capacitors connected in parallel, where Y_{in} and Y_{out} give the capacitances between the electrodes and ground and $Y_{coupling}$ gives the inter-electrode capacitance.

The admittance of one 'real' capacitor (modelled in figure 4.9a) is

$$Y = \frac{1}{R_s + j\omega L + \left(\frac{1}{R_p} + j\omega C\right)^{-1}} \tag{4.5}$$

where Y is a complex number, R_s is the series resistance, L is the inductance, C is the capacitance and R_p is the parallel resistance as previously seen in figure 4.9a. Since the capacitors are connected in parallel the overall admittance will be a sum of their individual admittances $Y_{\text{Total}} = Y_1 + Y_2 + Y_3$. The real and imaginary parts were fitted separately and the values for R_s, L and C were extracted from the fit. R_p was fixed because it represents the resistance of the substrate (whose bulk resistivity is 17 - 23 Ω cm at 300 K [1]) and once this value is above ≈ 1 kΩ it no longer has an effect on the admittance profile. Examples of a fit to the real and imaginary data for one electrode pairing can be found in figures B.1 and B.2 in Appendix B.

4.2.3 Results Of The Wafer Probe Setup

To model the entire chip all of the possible π-networks must be measured which means measuring the S-parameters of all the possible electrode pairings. Figure 4.17 shows all

the possible π-networks in the chip which sum to 28 different configurations if the ground plane is considered as a separate port.

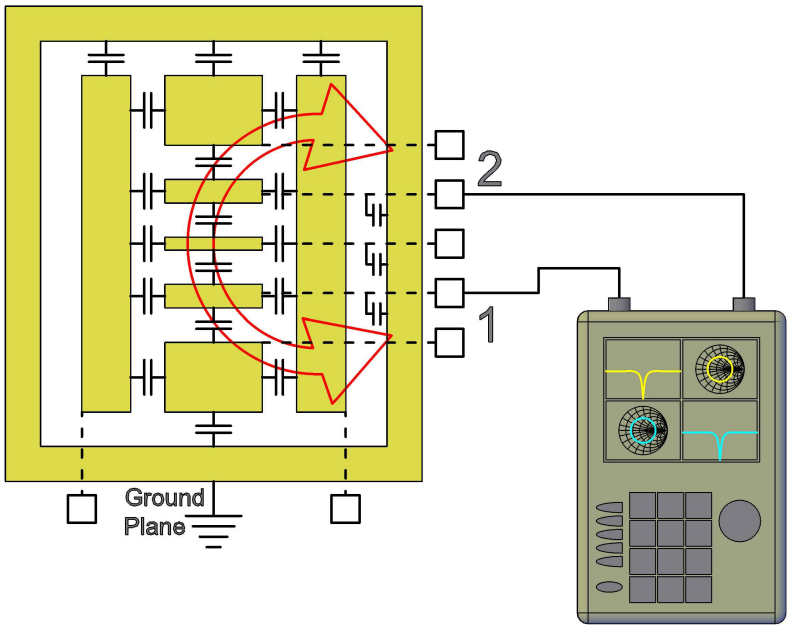

Figure 4.17: A schematic of all the possible π-networks that exist in the Geonium Chip [1] where the red arrow indicates the electrodes used as ports in the VNA measurement.

Analysis of the data from the S-parameters of the wafer probe setup revealed that the first resonances shown in figures 4.8 and 4.16b gave rise to the largest capacitances. As a result only the values extracted from the fits of the first capacitive modes are discussed in this section and shown in table 4.1. The rest of the data is included in Appendix B for reference. For each electrode, two sets of real fit parameters and two sets of imaginary fit parameters were used to calculate a weighted average for the chip's R_s, L and C. It is the capacitances extracted from the fits to $\mathrm{Y_{in}}$ and $\mathrm{Y_{out}}$ that appear in parallel with the helical resonator and influence the detection system. The capacitance values given in table 4.1 while large, are still small enough to be tuned out by the helical resonator. Theoretically the endcaps should have a larger input capacitance than the correction electrodes but the values in table 4.1 also include the capacitances caused by the wafer probe setup.

The inter-electrode capacitances were calculated from the real parts of $|\mathrm{Y_{12}}|$ and $|\mathrm{Y_{21}}|$, with the same weighted average applied. Again, only the first capacitive mode is shown in table 4.2 and the rest of the data can be seen in Appendix B. Table 4.2 shows that similar

Table 4.1: Parameters extracted from fits to the Y_{in} and Y_{out} data of all central electrodes using the wafer probe setup

Electrode	Value ± Error		
	R_s (Ω)	L (nH)	C (pF)
Right Endcap	38.0 ± 0.1	34.9 ± 0.1	43.7 ± 0.3
Right Compensation	37.8 ± 0.1	42.0 ± 0.2	43.7 ± 0.3
Ring	39.5 ± 0.1	51.3 ± 0.3	36.6 ± 0.3
Left Compensation	37.8 ± 0.1	42.0 ± 0.2	43.7 ± 0.3
Left Endcap	37.2 ± 0.2	44.3 ± 0.3	42.4 ± 0.4

Table 4.2: Inter-electrode capacitances between the central electrodes using the wafer probe setup

Electrode	Value ± Error		
	R_s (Ω)	L (nH)	C (pF)
Right Compensation to Right Endcap	344 ± 20	502 ± 57	20 ± 3
Right Endcap to Ring	137.9 ± 0.9	116 ± 1	3.50 ± 0.03
Right Compensation to Ring	359 ± 14	815 ± 46	17.9 ± 1.4
Left Compensation to Right Compensation	120 ± 1	103 ± 1	4.0 ± 0.5
Left Compensation to Ring	363 ± 13	838 ± 44	17.6 ± 1.3
Left Endcap to Ring	132.3 ± 0.9	107.7 ± 0.9	3.74 ± 0.04
Left Endcap to Right Endcap	196 ± 4	182 ± 4	2.02 ± 0.05
Left Compensation to Left Endcap	361 ± 18	555 ± 49	20 ± 2

pairings of electrodes give rise to similar inter-electrode capacitances as would be expected for a symmetrical chip. For example, the capacitance from the right endcap to the ring is (3.50 ± 0.03) pF and the capacitance from the left endcap to the ring is (3.74 ± 0.05) pF. The capacitances from the compensation electrodes to their neighbouring electrodes are particularly large and the implications of this are discussed in section 4.3.

4.2.4 Results Of The Wire Bonded Setup

The wire bonded setup was measured and analysed in the same manner as the wafer probe setup and the values extracted from the data fits can be seen in tables 4.3 and 4.4.

Again, the inter-electrode capacitances from one side of the chip to the other are generally symmetrical. However, the capacitances from the compensation electrodes to

Table 4.3: Parameters extracted from fits to the Y_{in} and Y_{out} data of all central electrodes using the wire bonded setup

Electrode	Value ± Error		
	R_s (Ω)	L (nH)	C (pF)
Right Endcap	53.6 ± 0.1	37.42 ± 0.08	80.0 ± 0.4
Right Compensation	51.1 ± 0.1	29.77 ± 0.06	65.8 ± 0.3
Ring	54.3 ± 0.1	25.25 ± 0.30.05	53.1 ± 0.2
Left Compensation	50.08 ± 0.02	24.83 ± 0.06	43.7 ± 0.3
Left Endcap	48.76 ± 0.1	25.38 ± 0.08	52.7 ± 0.4

Table 4.4: Inter-electrode capacitances between the central electrodes using the wire bonded setup

Electrode	Value ± Error		
	R_s (Ω)	L (nH)	C (pF)
Right Compensation to Right Endcap	99.6 ± 0.4	44.4 ± 0.2	10.8 ± 0.08
Right Endcap to Ring	160 ± 0.8	74.2 ± 0.4	4.24 ± 0.03
Right Compensation to Ring	116.4 ± 0.6	40.0 ± 0.2	7.99 ± 0.08
Left Compensation to Right Compensation	161.3 ± 0.7	78.7 ± 0.3	3.69 ± 0.02
Left Compensation to Ring	120.9 ± 0.6	43.9 ± 0.2	6.77 ± 0.06
Left Endcap to Ring	216 ± 3	75.8 ± 0.1	3.20 ± 0.07
Left Endcap to Right Endcap	297 ± 1	247 ± 1	2.98 ± 0.02
Left Compensation to Left Endcap	108.2 ± 0.5	54.5 ± 0.1	6.52 ± 0.05

their neighbouring electrodes are much smaller. By contrast the output capacitances are of the same order of magnitude as those seen with the wafer probe setup, with most being higher with the wire bonded setup. The values in table 4.3 are not as consistent as those in table 4.1. For example, when using the wafer probe setup the output capacitance from the left compensation was exactly the same as that from the right compensation. However, when using the wire bonded setup these two values are quite different. This suggests that the wire bonded setup should be re-measured and re-analysed to ensure that these deviations are not merely a measurement artefact. These wire bonded measurements confirm that the inter-electrode capacitances are affected by the method of contacting the chip but the input capacitances are not greatly affected. Therefore, the Geonium Chip itself must have $\sim$ (40 - 50) pF of capacitance between each of the electrode pads and

ground. It also confirms that the losses represented by R_s are between $(40-50)$ Ω at 300 K, the implications of this are discussed in the next section.

4.3 Limitations Of The First Generation Geonium Chip

As explained in chapter 3 the parasitic capacitance of the chip has a negative effect on the performance of the detection system. The chip's output capacitance (C_T) modifies the resonance frequency of the helical resonator by adding to the coil's own self capacitance (C_{coil}) via

$$\omega_{LC} = \frac{1}{\sqrt{(C_T + C_{\text{coil}})L_{\text{coil}}}}. \tag{4.6}$$

This reduces the resonance frequency of the loaded coil. From equation 3.16 this also means that the resonator's Q-factor reduces. Therefore, the output capacitances of the Geonium Chip place a limitation on the Q-factor of the detection system seen by the electron.

In addition to the output capacitances, the inter-electrode capacitances mean that the resonator 'sees' the output capacitance of the pickup electrode and the output capacitances of all the other electrodes. These inter-electrode capacitances are lower in the wire bonded setup and therefore moving to this contact method should be seriously considered in future iterations.

Lastly, the equivalent circuit of a 'real' capacitor includes a series resistance (R_s) which models all of the losses in the system. In the Geonium Chip these losses are substantial at 300 K. They are so large that when the chip is directly connected to the resonator at room temperature the resonance cannot be seen without excitation. Part of these losses stem from the resistance of the buried wires which connect the electrodes to the contact pads on the edge of the chip. The room temperature resistance of these wires is 1.75 kΩ which drops to 950 Ω at 77 K. Theoretically a larger drop of a fifth of the room temperature resistance would have been expected [2]. Consequently, the group is currently trying to measure this buried wire resistance at 4 K to determine how much the losses of the Geonium Chip reduce at cryogenic temperatures. The losses need to reduce by two to three orders of magnitude of their 300 K value for the resonator to be visible when attached to the chip at 4 K, without the need for excitation.

For future designs of the Geonium Chip the buried wire resistance must be reduced by increasing their cross-sectional area. Additionally, the output capacitances of the chip must be as small as possible. These can be reduced by increasing the insulating gaps

between the electrodes and by choosing a substrate with a lower dielectric constant, such as sapphire. However, care must be taken to ensure that the gaps are not too large that charge builds up in the insulating gaps and distorts the trapping potential.

Overall, care should be taken when designing a system to connect to the chip's contact pads so that any parasitic capacitances of the chip are not increased. To avoid the issues of the chip's capacitances loading the resonator a completely different approach can be considered when trying to detect the electron's cyclotron frequency. This is discussed in the next section.

4.4 Transmissivity

As discussed earlier in section 4.1 the Geonium chip was ordered with two different thicknesses of gold silver alloy and a pure gold metallisation. The alloys were designed to allow MW frequencies to pass through the chip as adding silver to the gold increases its resistivity. Table 4.5 shows that the alloy maintains a much higher resisitvity at 4 K than pure gold. Increasing the resistivity increases the material's skin depth (δ) as,

$$\delta = \frac{2\rho}{\omega\mu} \tag{4.7}$$

where $\mu = \mu_r\mu_0$, μ_r is the relative magnetic permeability of the conductor, μ_0 is the permeability of free space and ρ is the material's resistivity.

Table 4.5: Resistivities of pure gold and 80:20 gold silver alloy at 300 K and 4.2 K [1]

Resistivity (x$10^{-8}\,\Omega m$)		
	300 K	4.2 K
Au	2.271	0.022
AuAg 80:20	9.55	7.3

The skin depth is the surface thickness of the conductor through which the majority of the AC current flows. Therefore, the larger the skin depth of the chip, the deeper the current flows (for a particular frequency) and the more transparent the chip becomes. This feature will allow the electron's cyclotron frequency to couple to a waveguide beneath the chip. Which means that not only is direct detection of the cyclotron frequency possible but also importantly, resistive cooling of the cyclotron mode.

The strength of the microwaves that pass through the chip has been measured by J. Lacy. The experimental setup can be seen in figure 4.18 where the chip is placed above

a co-planar waveguide which is terminated at one end by a short and connected to a microwave generator at the other. An antenna was made from a male SMA connector suspended above the chip and connected to a signal analyser. The antenna was fixed to the spindle holder of a CNC machine which means that the antenna can be moved across the surface of the chip using the CNC.

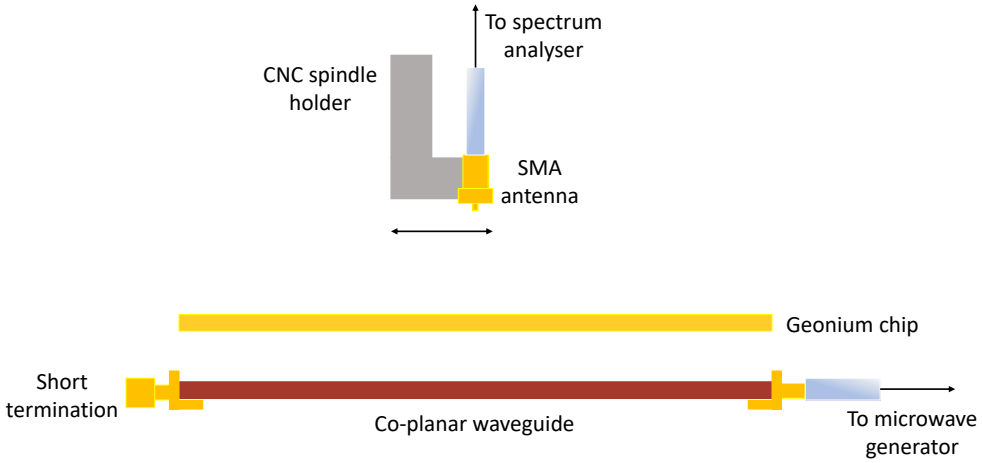

Figure 4.18: Setup for testing the transmissivity of the Geonium chip

Figure 4.19 shows the signal detected above the waveguide with and without a Geonium Chip with a metalisation layer of 300 nm of gold. The signal passes through the chip at room temperature, with some attenuation. However, the resistivity of gold reduces greatly at cryogenic temperatures and so the signal would be blocked from passing through the chip. Repeating this experiment with the gold silver alloy at 300 K and 77 K and combining the results with theory leads to the expected transmission percentages in table 4.6 [1].

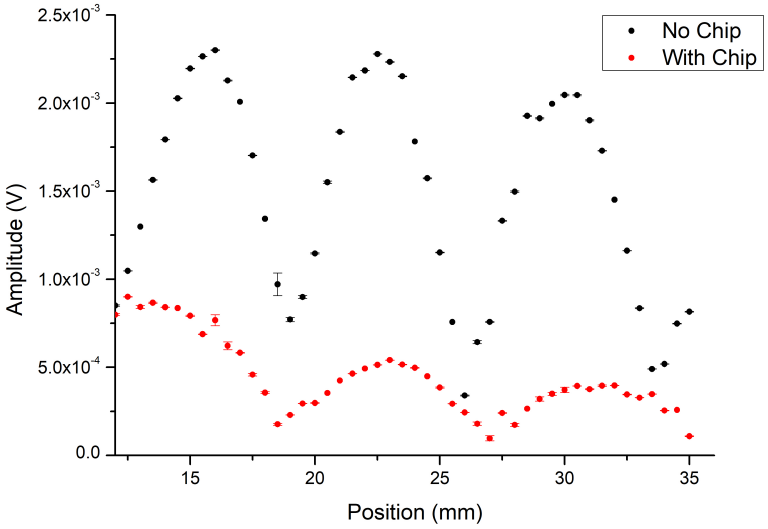

Figure 4.19: 18 GHz microwaves detected on the co-planar waveguide with and without the chip containing a 300 nm gold metalisation layer

Table 4.6: Expected transmission of microwaves through the Geonium chip [1]

Percentage transmission of 14 GHz		
	300 K	4.2 K
Au 300 nm	62.6 %	0.85 %
AuAg 300 nm	79.6 %	77 ± 5 %
AuAg 100nm	92.7 %	91.7 ± 5 %

Table 4.6 shows that while the gold layer would allow the cyclotron signal to pass through the chip at room temperature, it would be greatly attenuated at 4 K. However, the 100 nm gold silver alloy would allow 91.7% of the signal to pass at 4 K. Therefore, when the focus of the group turns to the measurement of the cyclotron frequency, the measurements should be made with the Geonium Chips which carry a gold silver metalisation layer of 100 nm.

4.5 Microwave Chamber

The final section of this chapter concerns the microwave chamber which was introduced in section 2.2. Once an electron is trapped above the surface of the chip optimisation steps can be taken to improve the harmonicity of the trapping region thereby leading to a more accurate measurement of the axial frequency. However, this requires the electron to have a long enough lifetime in the trap. Therefore, a cryogenic vacuum chamber is required

around the trapping region to prevent the electron from interacting with any other particles which may cause it to leave the trap. The design of our cryogenic vacuum chamber was inspired by the on chip design of Wilpers et al [83]. The benefit of securing the vacuum chamber to the chip is that the contact pads can remain outside the chamber. This negates the need for bulky feedthroughs which distort the performance of the detection system with their parasitic properties. In addition, the dimensions of the chamber have been designed to act as an off-resonant microwave chamber. This will inhibit the spontaneous emission of the cyclotron mode via the Purcell effect [84] and therefore increase the lifetime of the trapped electron.

The first microwave chamber (figure 4.20) was manufactured in-house and was therefore subject to the manufacturing limitations at the time. The chamber was milled from aluminium which is more cost effective and easier to mill than oxygen free copper. The aluminium was gold plated to maximise the conductivity of its surfaces and prevent oxides forming. The process of gold plating aluminium requires many steps to achieve a good surface finish, the details of which can be found in [1].

The electrons are loaded into the trap using the photoelectric effect so the chamber requires optical access for the UV generation of photoelectrons. This was provided with the use of a quartz window. However, this window then presents a dielectric surface to the trapping region. Therefore a gold plated mesh was installed on the inside surface of the window. This mesh provides an 85% open area to the UV source but screens the trapping region from stray microwaves and radio frequency signals. In addition, the chamber also required a pinch-off tube through which the chamber could be evacuated and then sealed. Due to the dimensions of the chamber the pinch-off tube could not be directly welded to the chamber. It was therefore welded to a flange which was then sealed to the chamber. This means that there are three seals (the chip, the window and the pinch-off) that have to be made to ensure that the chamber holds a vacuum. All three seals were initially made using an indium cold weld. However, this did not always create a sufficient seal. As such the seals around the window and the pinch-off tube were reinforced with cryogenic Stycast epoxy. The seal to the chip remained as a pure indium cold weld that was sealed under clean room conditions.

Once sealed the chamber was pumped out to a pressure of 10^{-6} mbar, which is expected to drop at cryogenic temperatures. As there is no pressure gauge attached to the chamber, its pressure at cryogenic temperatures can only be estimated using the lifetime of the electron.

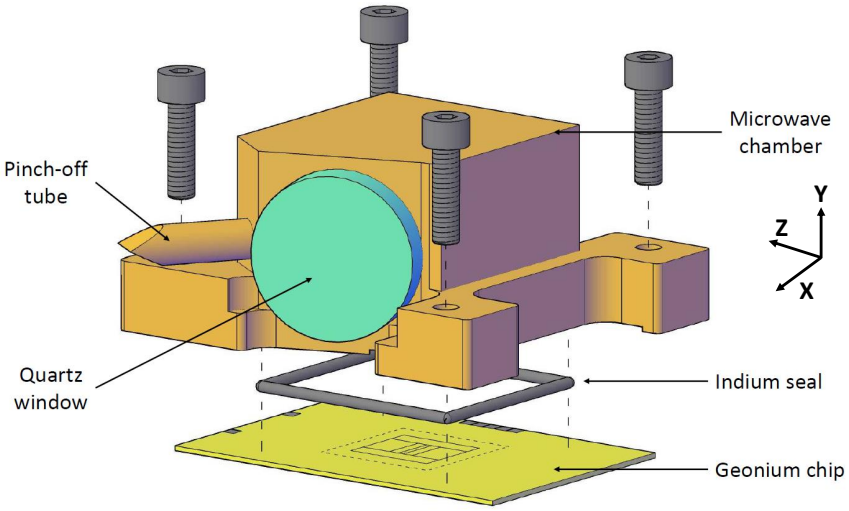

(a) CAD drawing of the microwave chamber

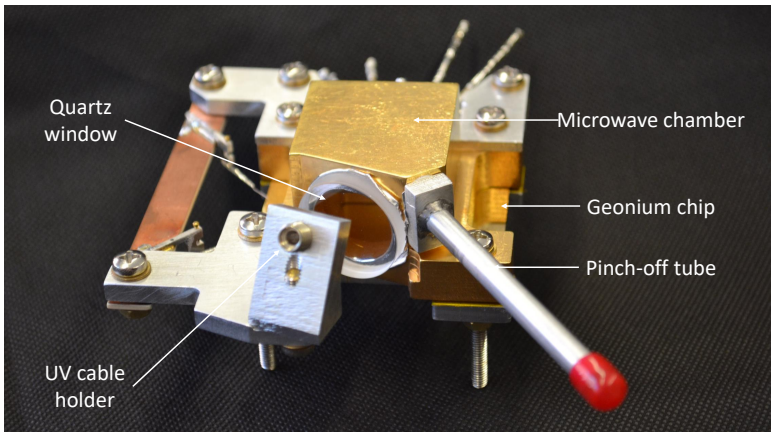

(b) Finished microwave chamber

Figure 4.20: The microwave chamber designed and manufactured by J. Pinder

Chapter 5

The Planar Magnetic Field Source

In order to trap and detect the electron we require a homogeneous magnetic field across the trapping region. The homogeneous field is orientated along the z-axis of the trap with a field strength B_0 such that $\vec{B} = B_0 \cdot \hat{u}_z$. It therefore has no gradient, curvature or higher derivatives of the magnetic field. Ordinarily in Penning trap experiments this field is provided by a large superconducting solenoid. However, these solenoids are expensive and not suitable for a fully scalable system. Therefore, we have designed and built a planar magnetic field source which locally produces a homogeneous field at the trapping position, $(0,\ y_0,\ 0)$. This chapter details the theory behind creating a homogeneous field from a planar source, the initial prototype manufacture, its characterisation at room temperature and its testing at 4 K.

5.1 Magnetic Inhomogeneities

Inhomogeneities such as the gradient and curvature of the magnetic field can prevent the electron from being detected by causing energy dependent fluctuations in the electron's eigenfrequencies [4]. Due to the symmetry of our magnetic field source the most relevant and dangerous inhomogeneities are those formed along the y-axis, which extends upwards from the surface of the chip. The axes used in this chapter are the same as those defined in figure 2.2.

The linear perturbations of the frequencies with energy can be expressed as frequency shifts matrices, in the same manner as those detailed in section 2.2.2 for the electric anharmonicities. A calculated example of the frequency shifts caused by inhomogeneities in the magnetic field can be seen in [4]. The result of these inhomogeneities is shown in figure 5.1 where the magnetic field gradient in the y-direction is affecting the visibility of

the axial dip. Small gradients can distort the axial dip but still allow detection, whereas large gradients in the mT/mm range prevent detection completely by shifting the axial frequency away from resonance with the detection system. Figure 5.1 shows an example electron dip where only one current carrying wire has been simulated beneath the chip [4].

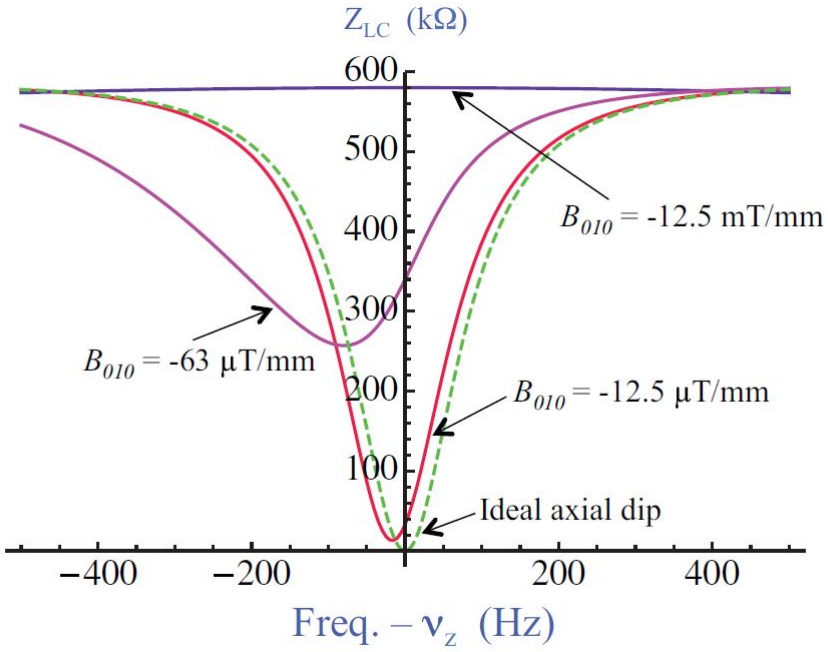

Figure 5.1: Calculated axial dip of a trapped electron in various magnetic field gradients in the y-direction (B_{010}) [4]. The magnetic field is provided by one current carrying wire which gives a field strength of 0.5 T at 1.45 mm above the surface of the chip.

The gradient, curvature and higher order inhomogeneities can be reduced by placing pairs of wires on either side of the main wire to form shims, as shown in figure 5.2. Adjusting the currents through the shim wires can reduce B_{010} (the magnetic field gradient in the y-direction) to a few μT/mm and B_{020} (the magnetic field curvature in the y-direction) to a few μT/mm^2 [4]. To calculate the currents required in the shim wires the inhomogeneities of the main current carrying wire are found from the series expansion of the axial component of the magnetic field at the trapping position

$$B_z = B_0 + B_{z,010}(y - y_0) + B_{z,020}(y - y_0)^2 + B_{z,030}(y - y_0)^3 + \cdots , \tag{5.1}$$

where the magnetic inhomogeneities are

$$B_{z,ijk} = \frac{1}{i!j!k!} \cdot \frac{\partial B_z}{\partial x^i \partial y^j \partial z^k}\bigg|_{(0,y_0,0)} . \tag{5.2}$$

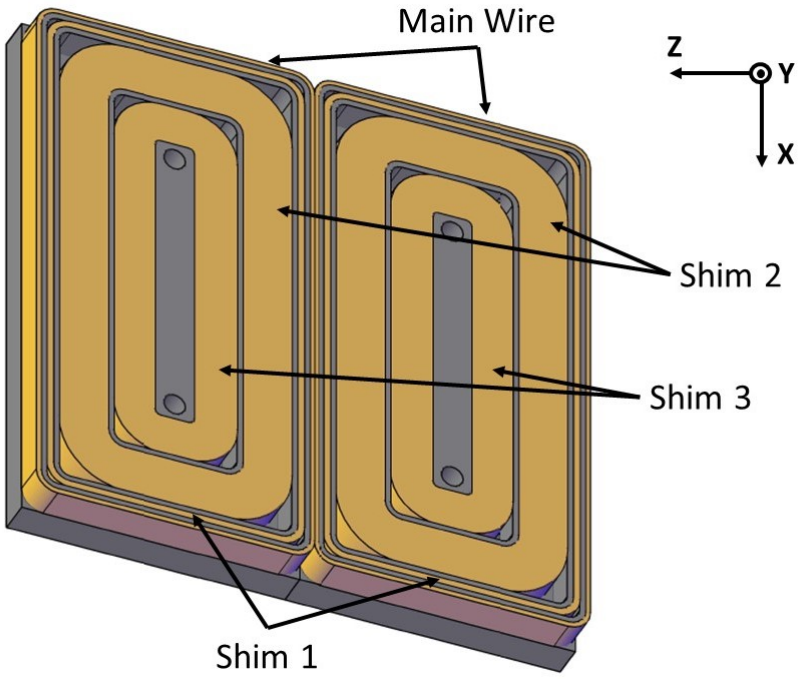

Figure 5.2: CAD design of the magnetic field source showing the shim pairs with respect to the main wire

The currents in the shim wires need to be chosen so that their inhomogeneities combine to cancel those created by the main wire. In our magnetic field source three shim pairs are used and due to the additive nature of the magnetic field the overall axial component of the magnetic field from all four wires is

$$B_z = B_{z,0} + \left.\frac{\partial B_z}{\partial y}\right|_{y_0} (y - y_0) + \left.\frac{\partial^2 B_z}{\partial y^2}\right|_{y_0} (y - y_0)^2 + \left.\frac{\partial^3 B_z}{\partial y^3}\right|_{y_0} (y - y_0)^3 + \cdots , \tag{5.3}$$

where

$$B_{z,0} = B_z^0 + B_z^1 + B_z^2 + B_z^3 \tag{5.4}$$

$$\left.\frac{\partial B_z}{\partial y}\right|_{y_0} = \left.\frac{\partial B_z^0}{\partial y}\right|_{y_0} + \left.\frac{\partial B_z^1}{\partial y}\right|_{y_0} + \left.\frac{\partial B_z^2}{\partial y}\right|_{y_0} + \left.\frac{\partial B_z^3}{\partial y}\right|_{y_0} \tag{5.5}$$

$$\left.\frac{\partial^2 B_z}{\partial y^2}\right|_{y_0} = \left.\frac{\partial^2 B_z^0}{\partial y^2}\right|_{y_0} + \left.\frac{\partial^2 B_z^1}{\partial y^2}\right|_{y_0} + \left.\frac{\partial^2 B_z^2}{\partial y^2}\right|_{y_0} + \left.\frac{\partial^2 B_z^3}{\partial y^2}\right|_{y_0} , \tag{5.6}$$

and the superscripts denote which wire provides each component; 0 for the main, 1 for shim one, 2 for shim to and 3 for shim three. These components can then jointly be

expressed as a matrix

$$\Gamma = \begin{pmatrix} B_{z0} & B_{z1} & B_{z2} & B_{z3} \\ \partial_y B_{z0} & \partial_y B_{z1} & \partial_y B_{z2} & \partial_y B_{z3} \\ \partial^2_{y^2} B_{z0} & \partial^2_{y^2} B_{z1} & \partial^2_{y^2} B_{z2} & \partial^2_{y^2} B_{z3} \\ \partial^2_{z^2} B_{z0} & \partial^2_{z^2} B_{z1} & \partial^2_{z^2} B_{z2} & \partial^2_{z^2} B_{z3} \end{pmatrix}, \tag{5.7}$$

where the notation has been changed to maintain clarity. The last line has been has been set to target the inhomogeneity caused by the curvature of the magnetic field along z because such a curvature combined with a curvature in the y-direction would create a magnetic bottle. Whilst a magnetic bottle will be required in the detection of single microwave photons, as explained in section 1.2.1, it is a hindrance in the accurate measurement of our first trapped electrons. Once the Γ matrix is known, the currents for the main wire and the shims can be calculated to give any arbitrary magnetic field distribution

$$\begin{pmatrix} I_0 \\ I_1 \\ I_2 \\ I_3 \end{pmatrix} = \Gamma^{-1} \begin{pmatrix} B_0 \\ B_1 \\ B_2 \\ B_3 \end{pmatrix}, \tag{5.8}$$

where I refers to the current in each wire, B_0 is the strength of the magnetic field, B_1 is the gradient in y, B_2 is the curvature in y and B_3 is the curvature in z. Therefore, a homogeneous field can be found from

$$\begin{pmatrix} I_0 \\ I_1 \\ I_2 \\ I_3 \end{pmatrix} = \Gamma^{-1} \begin{pmatrix} B_0 \\ 0 \\ 0 \\ 0 \end{pmatrix}. \tag{5.9}$$

The determination of all of the components in the Γ matrix is discussed in section 5.3.

5.2 NbTi Prototype

The initial magnetic field source is a hand-wound set of niobium titanium (NbTi) coils, designed and manufactured by Dr J.Pinder. The wire has a diameter of 0.4 mm and is copper coated single filament NbTi wire from Supercon Inc. Each shim is wound as a pair around an aluminium forma which was made using our CNC machine. The formas were designed to sit one inside another as seen in figure 5.3.

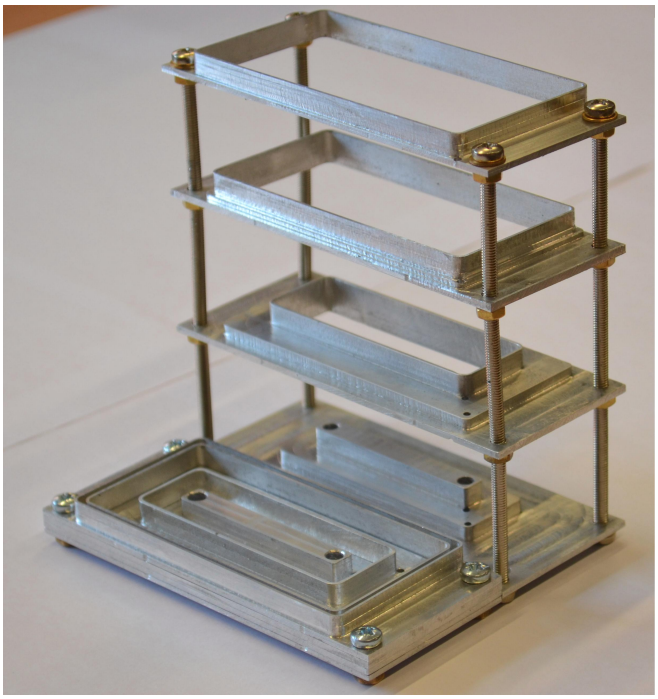

Figure 5.3: Magnetic field formas - with the left hand side collapsed and the right hand side open to show how they are nested together

The cross-sections of each shim pair were calculated by Dr J. Verdu using the principles set out in [85] and then the maximum number of turns was wound into the space available. The cross-sections of each wire and number of turns can be seen in table 5.1. The NbTi wire was wet wound with Styecast epoxy using a lathe and rotation counter. Once cured at room temperature for 24 hours the coils formas were screwed together to form the prototype magnetic field source seen in figure 5.4.

Table 5.1: Dimensions of the prototype coils

Coil	Cross-section (width x height) mm	No. of turns
Main	0.8 x 6	38
Shim 1	1.2 x 6	42
Shim 2	8.8 x 6	400
Shim 3	7.5 x 6	376

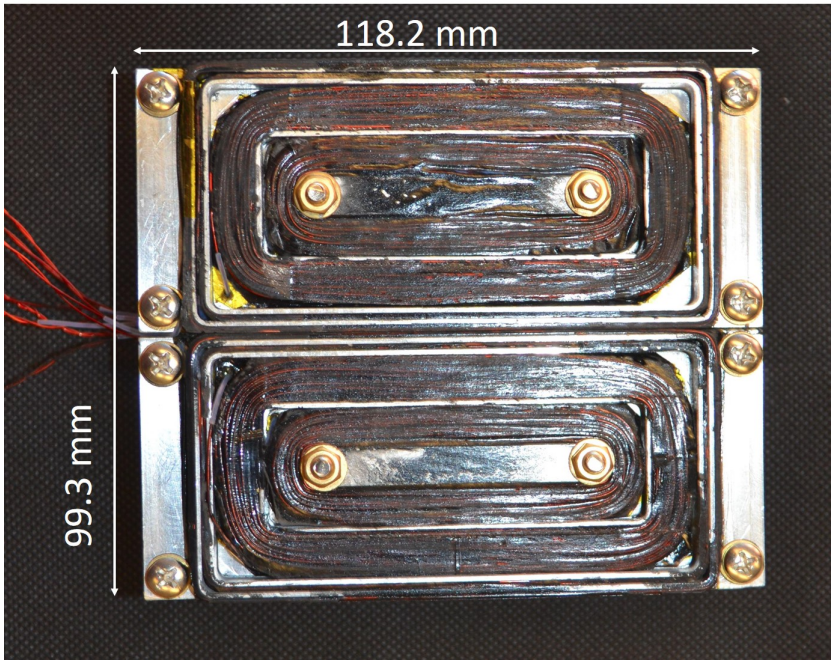

Figure 5.4: Magnetic field source prototype

5.3 Characterisation

To characterise the planar magnetic field source its Γ matrix was ascertained at room temperature. An example of obtaining one component of the Γ matrix is described below with a similar approach used for all the other matrix components.

The second row of the Γ matrix is made up of the components of the magnetic field gradient produced by each wire. It is not possible to measure each of these components individually, only the total magnetic field due to all of the wires can be measured. To find the magnetic field gradient contribution from shim one a set of currents are passed through all four of the wires and the total magnetic field is measured over a continuous range of y values. The total magnetic field gradient $\left(\frac{\partial B_z}{\partial y}\right)$ is extracted from a polynomial fit using equation 5.3. The current through shim one is then increased whilst keeping all the other currents the same. The process of measuring the magnetic field over a height interval is repeated and the new total magnetic field gradient is extracted from the polynomial fit. This new total magnetic field gradient now includes an additional term $\left(\Delta\frac{\partial B_z^1}{\partial y}\right)$ which is the increase in the gradient caused by shim one's increase in current

$$\left.\frac{\partial B_z}{\partial y}\right|_{y_0} = \left.\frac{\partial B_z^0}{\partial y}\right|_{y_0} + \left(\left.\frac{\partial B_z^1}{\partial y}\right|_{y_0} + \Delta\left.\frac{\partial B_z^1}{\partial y}\right|_{y_0}\right) + \left.\frac{\partial B_z^2}{\partial y}\right|_{y_0} + \left.\frac{\partial B_z^3}{\partial y}\right|_{y_0}. \tag{5.10}$$

Subtracting the initial total magnetic field gradient from the final total magnetic field

gradient gives $\Delta\frac{\partial B_z^1}{\partial y}$. The Γ matrix component due to the gradient caused solely by shim one is found from

$$\Gamma_{2,2} = \Delta\frac{\partial B_z^1}{\partial y}/\Delta I, \tag{5.11}$$

where ΔI is the change in the current supplied to shim one. This process is repeated with the rest of the wires, changing the current in one wire at a time. The measurements and analysis were performed by J.Lacy using a Hall probe attached to the spindle holder of our CNC machine. The setup can be seen in figure 5.5. Further details of the measurement technique can be found in the PhD thesis of J.Lacy [86]. The room temperature results for the Γ matrix, with $y_0 = 1.6$ mm, are

$$\Gamma_{300\text{ K}} = \begin{pmatrix} (-2008 \pm 8) & (1464 \pm 8) & (-4560 \pm 10) & (930 \pm 10) & \mu\text{T} \\ (490 \pm 10) & (-120 \pm 10) & (-340 \pm 20) & (160 \pm 10) & \mu\text{T.mm}^{-1} \\ (-130 \pm 20) & (-7 \pm 9) & (100 \pm 10) & (-10 \pm 10) & \mu\text{T.mm}^{-2} \\ (123 \pm 6) & (24 \pm 5) & (-83 \pm 8) & (8 \pm 4) & \mu\text{T.mm}^{-2}. \end{pmatrix} \tag{5.12}$$

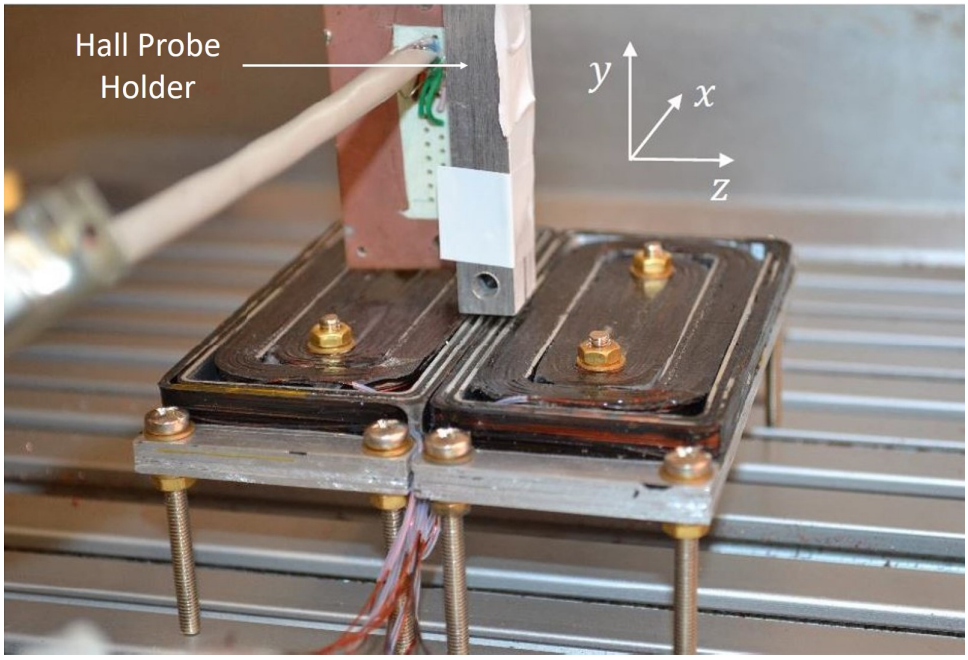

Figure 5.5: Setup to measure the gamma matrix of the prototype magnetic field source

Now that the matrix is known it can be used to find the shim currents required for a particular magnetic field, where all derivatives have been set to zero to eliminate inhomo-

geneities.

$$\begin{pmatrix} 0.1\,\mathrm{mT} \\ 0 \\ 0 \\ 0 \end{pmatrix} \Gamma^{-1} = \begin{pmatrix} I_0 \\ I_1 \\ I_2 \\ I_3 \end{pmatrix} = \begin{pmatrix} 18.6 \\ 73.0 \\ 63.5 \\ 128.7 \end{pmatrix} \mathrm{mA} \tag{5.13}$$

Re-measuring the magnetic field with these currents gave

$$B_z = \begin{pmatrix} -0.098 \pm 0.002 \\ -0.004 \pm 0.001 \\ 0.002 \pm 0.001 \\ -0.004 \pm 0.002 \end{pmatrix} \begin{matrix} \mathrm{mT} \\ \mathrm{mT.mm^{-1}} \\ \mathrm{mT.mm^{-2}} \\ \mathrm{mT.mm^{-2}}, \end{matrix} \tag{5.14}$$

which shows that the Γ matrix does provide a homogeneous field within the error bars.

5.4 4 K Measurements

Once the magnetic field source had been tested at room temperature it was installed in the cryostat and cooled to 4 K. The wiring that transfers the current from the supply to the magnetic field source consists of three stages; thick copper wires either side of the cryostat flange, high temperature superconducting (HTS) tapes from the first cooling stage to the second cooling stage and NbTi wires from the second cooling stage to the magnetic field source. The wiring is discussed in more detail in section 7.2.3. The HTS tape is copper stabilised and the NbTi wires are copper coated, meaning that above the superconducting transition temperature copper dominates the resistance of the current path. The currents are provided by the Hameg HMP4040 in constant current mode. This mode adjusts the voltage output to maintain the specified current. Therefore, as the temperature decreases, the resistance of the prototype decreases and the voltage drawn from the supply decreases. This directly relates the temperature to the voltage of the source which can then be used to calculate the resistance of the current path as the current is known a priori. This is depicted in figure 5.6 where the resistance follows the behaviour expected by the Bloch-Grüneisen formula [87] for the change in a metal's resistivity with temperature (T). The formula states that at higher temperatures ($\mathrm{T} > \frac{\Theta_R}{2}$) the resistivity decreases linearly with temperature and at lower temperatures ($\mathrm{T} < \frac{\Theta_R}{10}$) the resistivity has a T^5 behaviour, where Θ_R is the Debye temperature [88]. Once the temperature decreases further the superconducting transition of the NbTi wire can be seen at ~ 5 K in figures 5.6a and 5.6b.

This transition temperature does not agree with the known transition point of 9 K for NbTi due to the placement of the temperature sensor which was not directly on the coil array but attached to the copper plate of the second cooling stage.

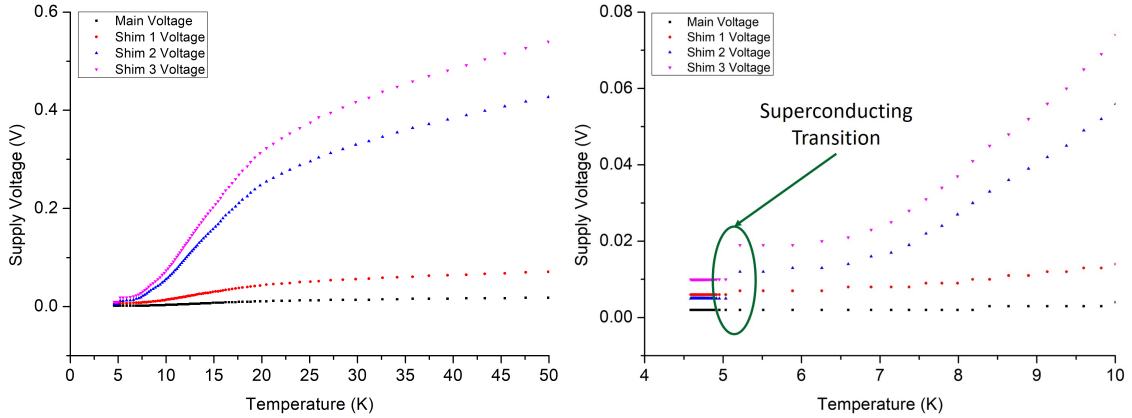

(a) 50 K to 4 K

(b) 10 K to 4 K

Figure 5.6: Voltage drawn by the magnetic field protoype from the current supply as the temperature decreases

The residual resistances of each wire were calculated from the voltage drawn from the current supply at 4 K and the applied current. These residual resistances are due to the purely copper sections of the current path and the six solder joints in each loop. These residual resistances can be seen in table 5.2.

Table 5.2: Residual resistances of the current path to and from the magnetic field prototype whilst the prototype is superconducting

Wire	Residual Resistance (Ω)
Main	0.1075
Shim 1	0.0822
Shim 2	0.0787
Shim 3	0.0781

The shift from conducting to superconducting not only affects the resistance of the current path but also the magnetic field of the source. Figure 5.7 shows the change in the magnetic field before and after the superconducting transition temperature. This data was taken with a 3-axis hall probe from *Arepoc* which was secured 1.6 mm above the surface of the magnetic field source. Channel 0 of the hall probe is aligned with the z-direction of the co-ordinate system shown in figure 5.5, channel 1 was aligned with the y-direction

and channel 2 with the x-direction.

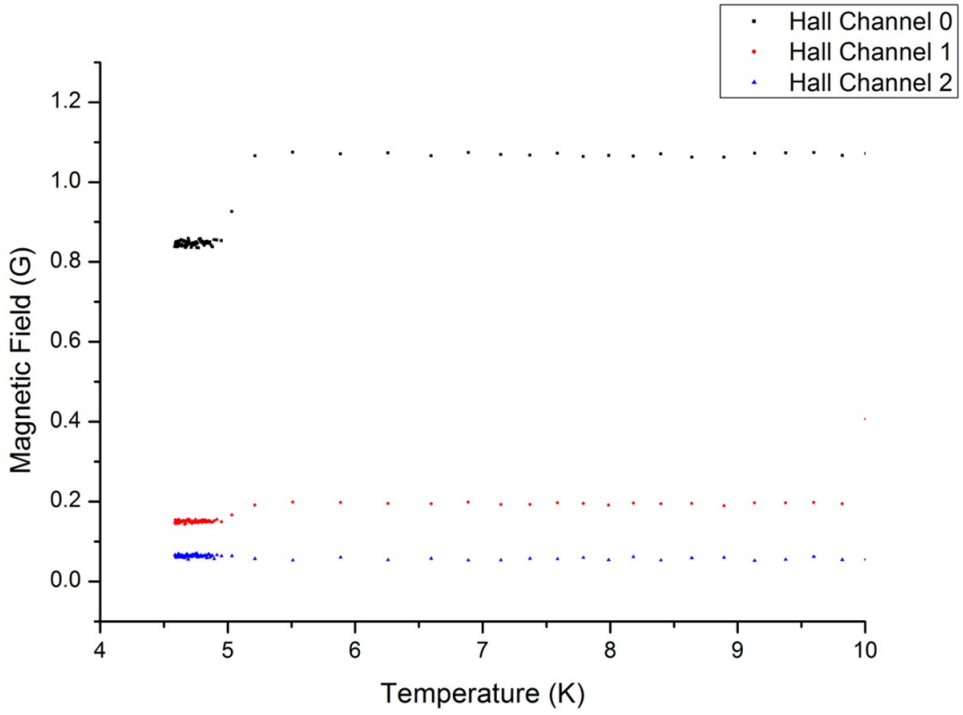

Figure 5.7: Magnetic field before and after superconducting transition. The currents used to make this measurement were 18.6 mA in the main wire, 73 mA in shim 1, 63.5 mA in shim 2 and 128.7 mA in shim 3.

The magnetic field changes after the superconducting transition point because the current is now mainly running in the superconductor and not through the copper casing. This changes the current density and, in accordance with the Biot-Savart law, the magnetic field produced by the NbTi wires. Since the magnetic field changes, the gamma matrix, which was measured at 300 K, must also be adjusted so that it remains an accurate way of calculating the currents required for a particular magnetic field configuration. To calculate the adjustments that must be applied to the gamma matrix, each wire was investigated separately. A current was put through one wire and the temperature was slowly increased using a resistor as a heater. The temperature was allowed to settle before the magnetic field was measured using a Hall sensor. The voltage applied to the resistor was then slowly decreased and the magnetic field was re-measured as the temperature fell. For each wire this gave plots similar to those in figure 5.8 where figure 5.8b shows the magnetic field as the temperature is increasing and figure 5.8a shows it whilst the temperature is decreasing. A linear fit was used either side of the transition temperature to find the magnetic field strength above the transition temperature (A) and below the transition temperature (B).

The percentage change (Δ) was then calculated for each graph using

$$\Delta = \frac{A - B}{A}. \tag{5.15}$$

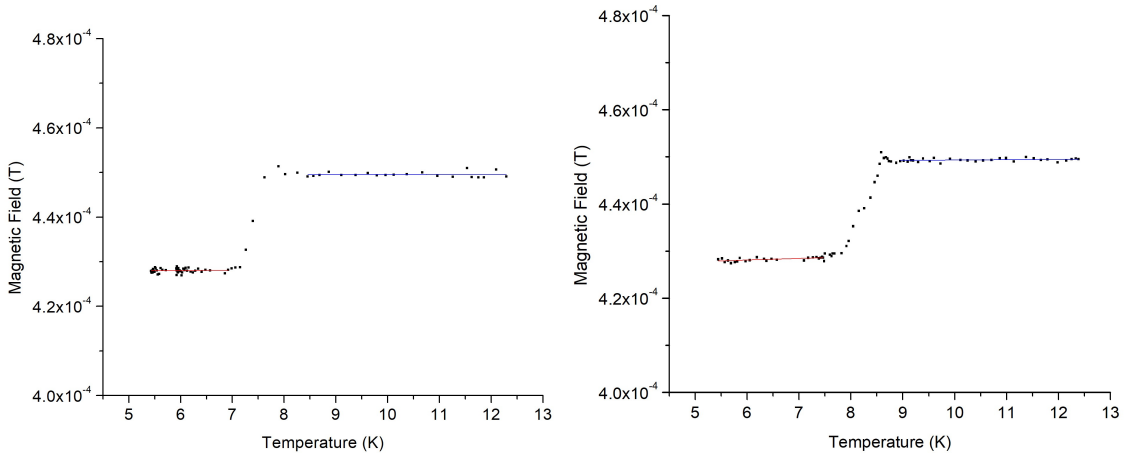

(a) Decreasing temperature

(b) Increasing temperature

Figure 5.8: An example magnetic field produced solely by shim two when the temperature is increased and decreased. Shim two was supplied with 100 mA during this measurement. Similar results are obtained for all the other wires that make up the magnetic field source.

The overall percentage change for each wire was calculated from a weighted fit of the change calculated when the temperature was decreasing and when it was increasing. The Δs calculated for each wire can be seen in table 5.3. The factor applied to each column of the gamma matrix is $1 - \Delta$ if the magnetic field due to that wire decreased below the transition temperature and $1 + \Delta$ if the magnetic field increased below the transition temperature. In the case seen in figure 5.8, which shows the behaviour of shim two, the temperature decreases below the transition temperature so column three of the gamma matrix is multiplied by $1 - \Delta$.

Table 5.3: Adjustments to the gamma matrix at cryogenic temperatures

Wire	Δ
Main	0.0690
Shim 1	0.0577
Shim 2	0.0478
Shim 3	0.0332

When these adjustments are calculated for each wire and applied to the gamma matrix

measured at room temperature, a cryogenic gamma matrix is formed

$$\Gamma_{4\,\mathrm{K}} = \begin{pmatrix} (-1869 \pm 8) & (1548 \pm 8) & (-4342 \pm 10) & (899 \pm 10) \\ (456 \pm 10) & (-127 \pm 10) & (-324 \pm 20) & (155 \pm 10) \\ (-121 \pm 20) & (-7 \pm 9) & (95 \pm 10) & (-10 \pm 10) \\ (115 \pm 6) & (25 \pm 5) & (-79 \pm 8) & (8 \pm 4) \end{pmatrix} \begin{matrix} \mathrm{mT} \\ \mathrm{mT.mm^{-1}} \\ \mathrm{mT.mm^{-2}} \\ \mathrm{mT.mm^{-2}}. \end{matrix} \tag{5.16}$$

This matrix can be used to calculate the currents required for particular magnetic field configurations at 4 K.

5.5 Alternative definition of the Γ matrix

When the currents for 0.1 mT (see equation 5.13) were calculated the Γ matrix elements were given to six decimal places. This did not take into account the size of the errors. Once the errors were calculated the Γ matrix elements were rounded to the correct number of decimal places and the currents for 0.1 mT were re-calculated. The currents were now given as (10.47, -8.92, 11.57, -14.17) mA. This clearly does not agree with those stated in equation 5.13. The reason for this was that the last two lines of the Γ matrix were almost equal to negative one times the other, making the matrix nearly non-invertible. This can be explained using Maxwell's equations which state that $\frac{\partial^2 B_z}{\partial x^2} + \frac{\partial^2 B_z}{\partial y^2} + \frac{\partial^2 B_z}{\partial z^2} = 0$ is always true and since $\frac{\partial^2 B_z}{\partial x^2} \simeq 0$, due to the symmetry of the chip, then $\frac{\partial^2 B_z}{\partial y^2} \simeq -\frac{\partial^2 B_z}{\partial z^2}$ [85]. A non-invertible matrix would give an infinite number of current configurations for the same magnetic field distribution. This made the process of calculating the currents for a given field non-repeatable.

To address this problem the last line of the matrix was changed to target the third order derivative of the magnetic field in the y-direction $\left(\frac{\partial^3 B_z}{\partial y^3}\right)$. The inversion of the Γ matrix is now repeatable. This is very important for maintaining repeatability of trapping attempts but it has also led to much lower current solutions for a given magnetic field strength. This allows us to reach higher magnetic fields than the previous current configuration (before the current limit of the of cryostat's feedthroughs are reached).

The final test at 4 K was to investigate how the temperature of the cryogenic region increased with the current input to the magnetic field source. Thermalisation methods to prevent the temperature from rising above the critical temperature of NbTi are discussed in section 7.2.3 and are constantly being improved upon. The magnetic field source itself does not limit the current supplied to it as the NbTi wires have a critical current of 175

A in a 3 T field [89]. However, the power feedthroughs used to supply the current to the cryostat are limited to 25 A. We therefore limited our investigation to the maximum current of 20 A which was supplied by two HMP4040 current supplies connected in parallel. The initial currents used were those for a 0.1 mT homogeneous field, (10.47, -8.92, 11.57, -14.17) mA, and this was increased until the largest current reached 20 A. At each point the temperature was allowed to stabilise before a reading was taken and the current increased again. The plot of the temperature increase caused by these currents can be seen in figure 5.9. This shows that we can reach a 0.14 T field with only an increase of 0.347 K which is more than adequate for our initial trapping attempts.

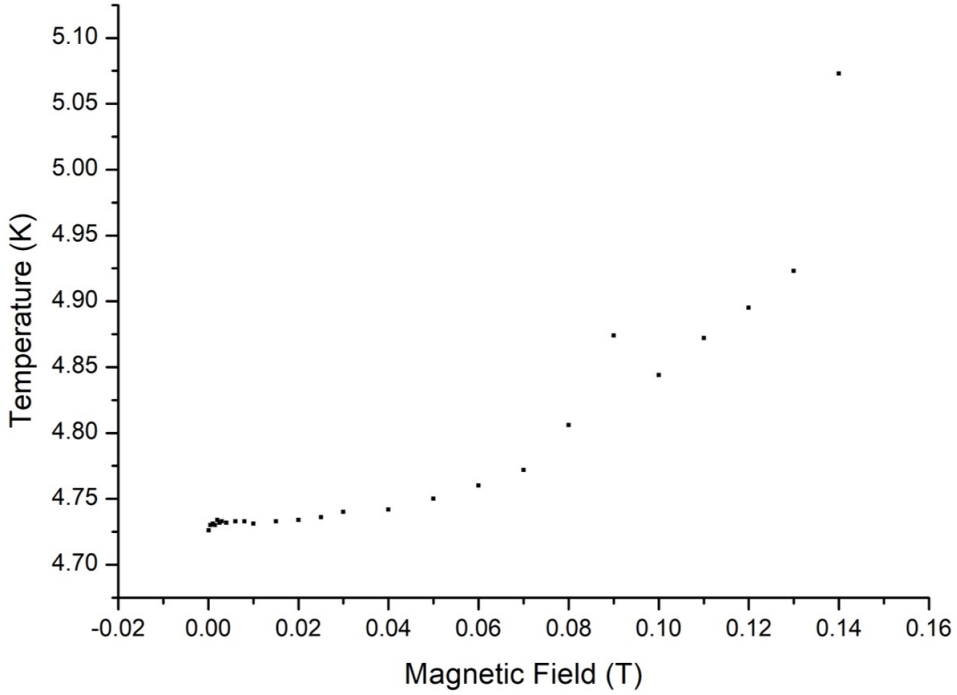

Figure 5.9: The increase in the temperature of the 4 K region of the cryostat with the increase in current supplied to the magnetic field source

5.6 Magnetic field currents for trapping

The Geonium Chip and microwave chamber sit directly above the magnetic field prototype as seen in figure 5.10. However, whilst the chip and chamber were being installed the chip cracked when the screws were tightened. Therefore, an additional washer was added between the surface of the magnetic field source and the bottom of the chip. The washer was insulated with kapton to prevent the coils of the array from shorting.

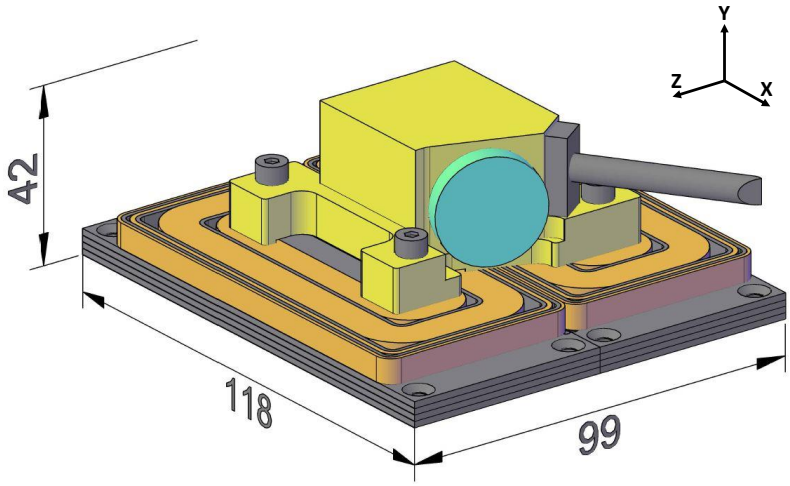

Figure 5.10: Position of the Geonium chip and MW chamber with respect to the magnetic field where the all the dimensions are given in mm.

Adding the washer however, produces a problem. The Γ matrix was measured at 1.6 mm above the surface of the magnetic field source because this coincided with the optimal electrostatic trapping height [4]. This optimal position is now 1.8 mm above the surface of the magnetic field source and the measured Γ matrix is no longer accurate. This misalignment of the optimal position of electric and magnetic fields could eventually make the axial electron dip undetectable. To calculate the new currents needed to maintain the same magnetic field distribution but at the new trapping height a Taylor expansion for a small displacement in y ($\delta y = y - y_0$) can be used

$$\Gamma(y) \approx \Gamma(y_0) + \left.\frac{\partial \Gamma}{\partial y}\right|_{y_0} (y - y_0), \tag{5.17}$$

where $\Gamma(y_0)$ is the original measured Γ matrix and the differential becomes

$$\left.\frac{\partial \Gamma}{\partial y}\right|_{y_0} = \begin{pmatrix} \partial_y B_{z0} & \partial_y B_{z1} & \partial_y B_{z2} & \partial_y B_{z3} \\ \partial^2_{y^2} B_{z0} & \partial^2_{y^2} B_{z1} & \partial^2_{y^2} B_{z2} & \partial^2_{y^2} B_{z3} \\ \partial^3_{y^3} B_{z0} & \partial^3_{y^3} B_{z1} & \partial^3_{y^3} B_{z2} & \partial^3_{y^3} B_{z3} \\ \partial^4_{y^4} B_{z0} & \partial^4_{y^4} B_{z1} & \partial^4_{y^4} B_{z2} & \partial^4_{y^4} B_{z3} \end{pmatrix}. \tag{5.18}$$

The new currents now vary with y according to

$$I(y) \approx \left[\Gamma(y_0) + \left.\frac{\partial \Gamma}{\partial y}\right|_{y_0} (y - y_0)\right]^{-1} \cdot B(y_0), \tag{5.19}$$

where $B(y_0)$ is the desired magnetic field distribution at the trapping height. Using the new currents the magnetic field over a range of y values can be calculated and compared

with a measured magnetic field variation with y. Figure 5.11a shows that the Taylor expansion is a valid method for calculating currents for homogeneous fields within a range of ± 0.5 mm of the originally measured Γ matrix, however figure 5.11b shows that this approximation does not hold at higher or lower heights. The new currents that provide a specified homogeneous field, 0.2 mm above the original measurement point can now be calculated.

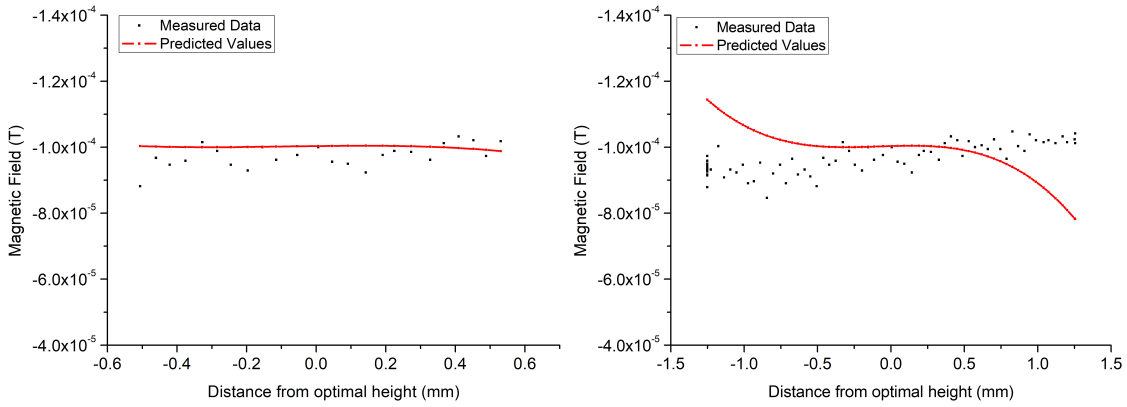

(a) Small range (b) Larger range

Figure 5.11: Comparison between the measured magnetic field and that predicted by the Taylor expansion

Chapter 6

Building The Detection System

The theoretical requirements of the detection system were investigated in chapter 3 and stated in section 3.3. In addition to a high Q-factor helical resonator, a cryogenic amplifier and superconducting transmission line were required. These were both fabricated in-house using a CNC machine and this chapter discusses not only their manufacture but also their testing at 300 K and 4 K. The optimisation of the Q-factor of the helical resonator is also explored. Finally, the separate parts of the detection system; the resonator, amplifier and transmission line are operated together and then coupled to the Geonium Chip.

6.1 Optimisation Of The Q-Factor Of The Helical Resonator

Chapter 3 has discussed the necessity of having a helical resonator with a high impedance on resonance. It is required to not only induce a large voltage signal from the electron but also to reduce the time it takes for the electron's motion to resistively cool. On resonance the impedance is linearly related to the resonator's Q-factor through equation 3.15. Therefore, to provide a large impedance to the current induced by the electron's axial motion, a resonator with a large Q-factor is required. This section describes the practical steps taken to achieve a Q-factor of 34,100 $\pm$ 400 at a temperature of 2.6 K.

The Q-factor of a helical resonator is related to the residual surface resistance (R_{res}) of both the coil and its shield via [76]

$$Q = \frac{\omega_{LC} L}{R_{\text{res}}}. \tag{6.1}$$

Therefore, to achieve a high Q-factor it is preferable to build the resonator from a superconducting material. Most cryogenic Penning trap experiments use resonators made from niobium titanium (NbTi), such as [75], because the magnetic fields that they employ

are above the critical field of pure niobium. However, the Geonium Chip experiment does not use large magnetic fields and the magnetic fields that are used are localised to the trapping region. As a result, the helical resonator used in this experiment has been built from 99.96% niobium which has a residual surface resistance that is 5-20 times smaller than NbTi [90]. The resonator was designed using the principles set out by Macalpine and Schildnecht [77] and machined by the Sussex University Workshop. The dimensions of the resonator, shown in figure 6.1, were chosen to give as large a Q-factor as possible whilst remaining within the dimensional constraints of the cryostat. The thickness of the coil was chosen to ensure that it was stable enough that it could keep its shape without a dielectric core. Using a dielectric would have increased the resonator's self-capacitance and therefore decreased its resonance frequency as well as introducing dielectric losses which would have reduced the Q-factor.

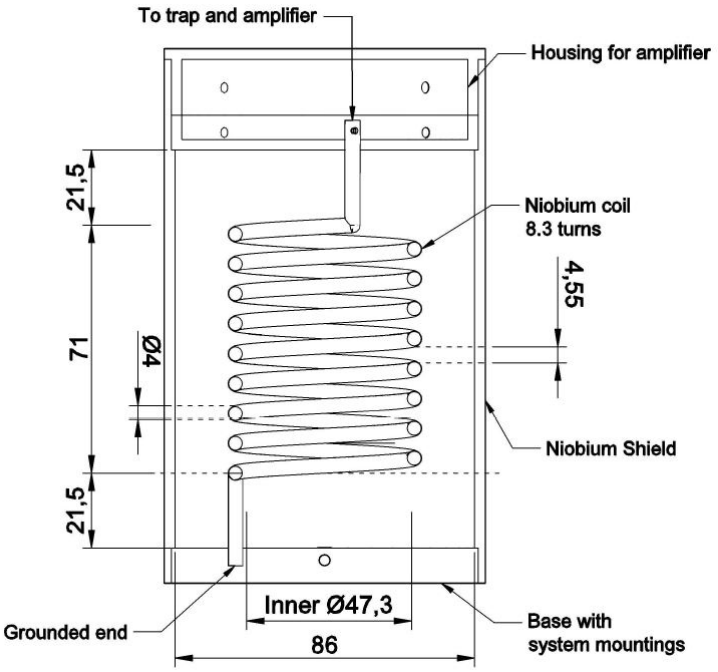

Figure 6.1: Dimensions of the axial resonator machined from niobium [1]

To measure the Q-factor of the machined resonator, its impedance with frequency must be measured using a Vector Network Analyser (VNA). The VNA measures with a standard characteristic impedance of 50 Ω at each of its ports which if directly connected to the resonator would load the resonator reducing both its resonance frequency and Q-factor [9]. This can be prevented by weakly coupling the resonator to the VNA through a 0.3 pF air capacitor made from two pieces of copper wire as seen in figure 6.2. Here the top of the resonator's coil is screwed to a metal tube which in turn is soldered to a circuit

board containing the air gap capacitor and SMA connector to the VNA.

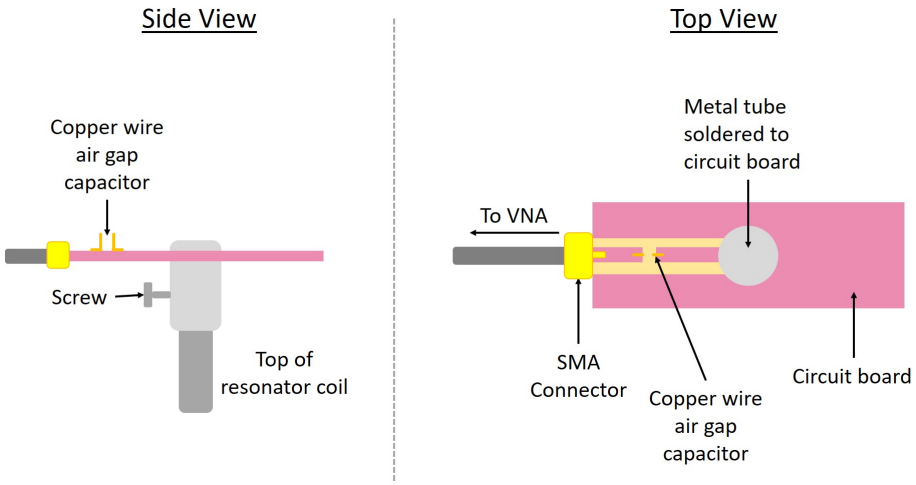

Figure 6.2: Circuit board for weakly coupling the helical resonator to the VNA

The resonator's reflection coefficient (S_{11}) was measured using Keysight's FieldFox Handheld Analyser and transformed to an impedance measurement using the VNA's internal conversion functions[1]. As previously seen in figure 3.3, the resonator's impedance follows a Lorentzian profile. From the fit of a Lorentz peak function to the VNA data, the peak frequency and full width at half maximum (FWHM) can be extracted. The Q-Factor and its associated error can then be calculated from

$$Q = \frac{\nu_0}{\text{FWHM}}. \tag{6.2}$$

The first impedance measurements conducted at 300 K and 6 K can be seen in figure 6.3, where each has been fitted with a Lorentz peak profile. The cryogenic measurement was limited to 6 K due to difficulties with thermalisation of the cryostat which prevented it from reaching its base temperature. These difficulties and their resolution are discussed further in section 7.1.1. As expected the peak narrows at lower temperatures due to the decrease in the resistivity of niobium, thereby increasing the Q-factor. This increase is controlled by the surface resistance of niobium which drops greatly below its critical temperature. However, the Q-factor increase from 302 ± 6 at 300 K to 1013.933 ± 0.002 at 6 K is not as large as expected and therefore steps to optimise the Q-factor were investigated. It is likely that part or all of the coil was above the critical temperature of niobium due to thermalisation issues.

[1] $Z_{\text{in}}(\text{Real}) = Z_0 \left(\frac{1-R^2-X^2}{(1-R)^2+X^2}\right)$ where $S_{11} = R + jX$

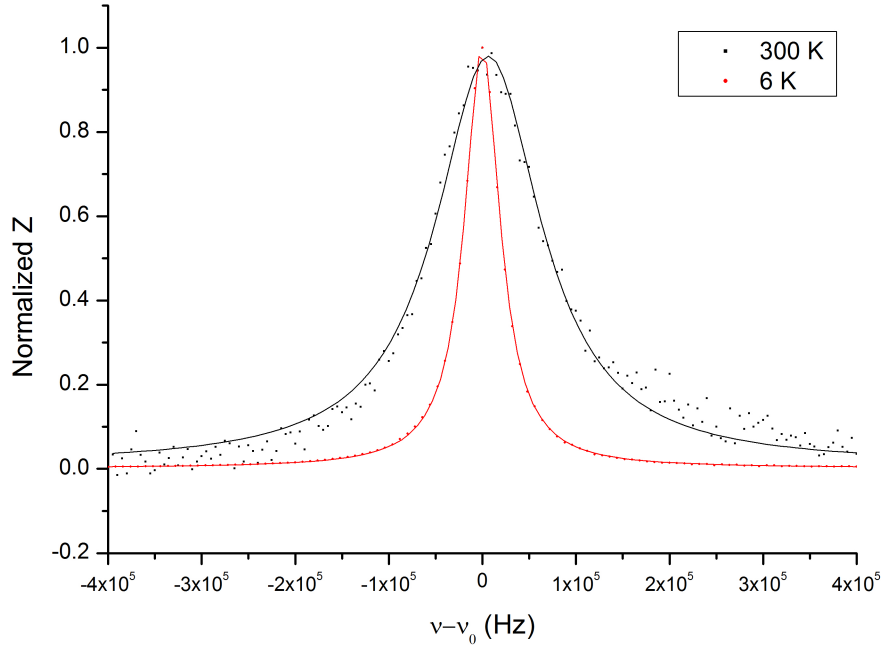

Figure 6.3: Resonance peaks at 300 K and 6 K, both fitted with a Lorentzian peak function. The cryogenic measurement was limited to 6 K due to difficulties with thermalisation that are discussed in section 7.1.1.

One way to improve the Q-factor is to polish the coil and the inner shield, thereby lowering its surface resistance [76]. The mechanical polishing steps carried out on the resonator are discussed in [1] and figure 6.4 shows the difference between the polished and the unpolished niobium.

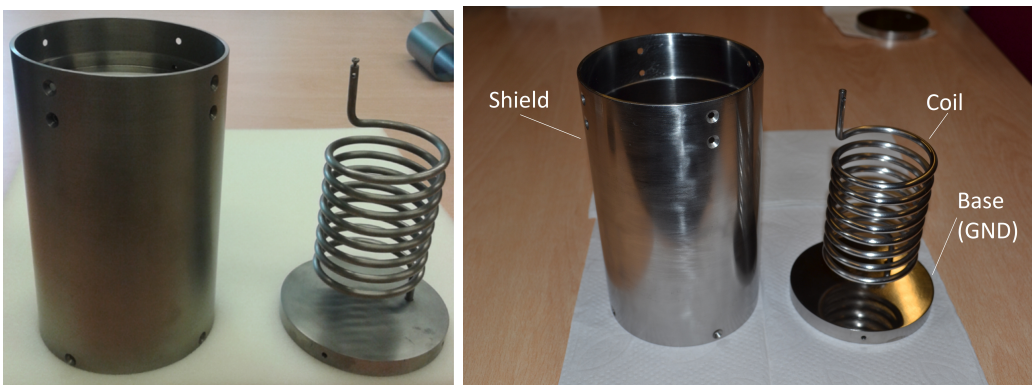

(a) Unpolished resonator (b) Mechanically polished resonator

Figure 6.4: Axial resonator made from pure niobium

The Q-factor was then remeasured at room temperature and found to have increased

from 302 ± 6 to 366 ± 4, an increase of 21%. However, a more robust connection board had been introduced and the resonance frequency was 7 MHz lower than the expected value of 47 MHz. On measuring the capacitance of the new board it was found that the board was adding $\sim$ 4.2 pF of capacitance from the signal path to ground. This capacitance appears in parallel with the coil's self capacitance thereby reducing the coil's resonance frequency. To minimise this parasitic capacitance the ground planes were stripped from the top and bottom of the board and the ground of the SMA connector was then explicitly connected to the ground of the resonator (the shield) via copper wires. The capacitance of the board was remeasured to be $\sim$ 1.9 pF, the Q-factor increased to 426 ± 1 and the resonance frequency returned to 47 MHz. Figure 6.5 shows the effect of the optimisation steps on the width of the resonance peak.

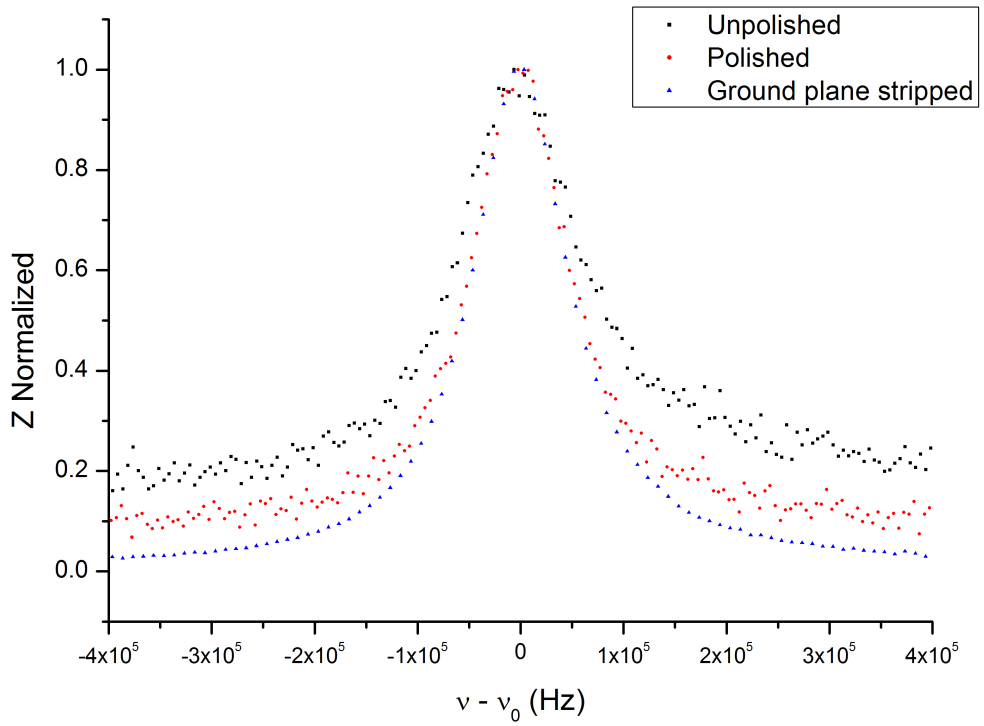

Figure 6.5: Optimisation steps to increase the Q-factor of the axial resonator

Striping the ground planes of the circuit board and using explicit grounding wires has also reduced the noise in the impedance measurement, as shown by the clean response in figure 6.5. This shows that ensuring the VNA ground is connected to the resonator ground is an important aspect of the measurement.

6.1.1 2.6 K Measurement

Once the optimisation of the resonator was completed and the thermalisation difficulties had been resolved the resonator was remeasured in the cryostat. To thermalise the coaxial cables that connect the resonator to the room temperature flange of the cryostat, 1 dB attenuators were used at the 60 K and 4 K temperature stages. These attenuators thermalise both the inner and outer conductors of the cables using a π-network or resistors between the inner and outer conductor to ensure that any heat travelling down the inner conductor is sunk at the higher temperature stage where there is more cooling power. The attenuators were wrapped in a copper jacket (see figure 6.6) and screwed to a copper L bracket, both of which were gold plated. Copper is a good thermal conductor and gold plating prevents the formation of copper oxides which would reduce the heat flow across the material boundaries. Indium was used to ensure a good thermal connection between the attenuator and the jacket. *N grease*[2] was then applied between the L bracket and the mounting strut to increase the surface area at the interface and again increase the heat flow across the boundary.

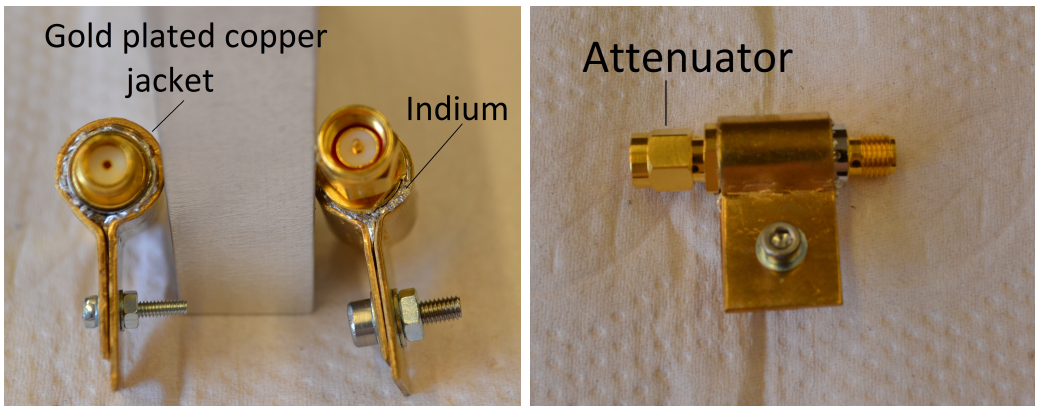

(a) Top view (b) Side view

Figure 6.6: Attenuator jacket used to thermalise the 1 dB attenuators which ensure that the inner and outer conductors of coaxial cables are thermalised.

The VNA calibration cable must pass through all the same interfaces as the measurement cable and as a result also passes through both of the 1 dB attenuators before reaching the 4 K section where it is connected to an open standard. The calibration used is only a one port reflection calibration rather than the preferred full two port calibration. A two port calibration is possible at cryogenic temperatures [91] but it is prohibitively time consuming and involves either expensive components or multiple cooldowns, and was

[2] Apezion N Grease for cryogenic high vacuum applications

therefore not undertaken for the cryogenic measurements of the helical resonator. Once a calibration is complete then the measurement can be taken in the same manner as those at room temperature. For this test the cryostat cooled to 2.6 K and the Q-factor was found to have increased to 34,100 ± 400. This is more than adequate to detect the signal of one electron. The comparison between the new 2.6 K measurement and the previous 6 K measurement can be seen in figure 6.7. The Q-factor could be further increased if the inner coil and its shield are electropolished to further reduce its surface resistance.

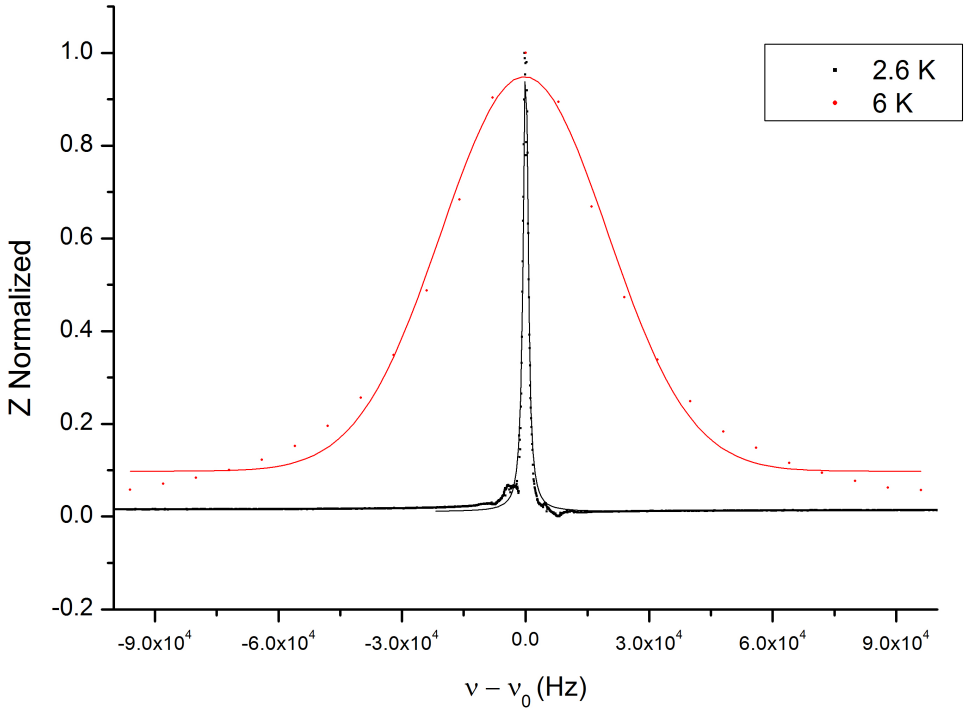

Figure 6.7: A comparison between the 6 K measurement of the unpolished coil and the 2.6 K measurement of the polished coil

6.2 Axial Amplifier

The current induced by the electron is in the order of femtoamps and, once the resonator has transformed this signal into a voltage, a cryogenic amplifier is needed before the signal can be observed on the FFT. This amplifier needs to be as close to the trap as possible to maintain a high signal to noise ratio. This axial amplifier must be capable of operating at cryogenic temperatures and survive thermal cycling (300 K - 4 K - 300 K). This puts limits on the components available for use in building the amplifier. Active

components like transistors cannot be made from silicon as it suffers from carrier freezeout and therefore gallium arsenide substrates, which do not suffer from this problem, must be used [92]. Capacitors can also change their capacitance values greatly from room temperature to 4 K. A natural choice is to use capacitors with ceramic dielectrics as these have low temperature co-efficients [93]. However, not all multilayer ceramic dielectrics are stable over a large temperature range. For example, types X7R and Y5V have been shown to lose more than 95% of their capacitance at 4K [94]. The most stable ceramics are those that meet the NP0 industrial standard (or the equivalent C0G). Unfortunately, large value capacitors (e.g. 1 μF) are not available with these dielectrics and therefore the next best option of polypheylene sulphide (PPS) film capacitors have to be used. Resistors must also be carefully selected as carbon and ceramic composition resistors have been shown to suffer from large percentage changes in their resistance after thermal cycling [95]. Companies like Vishay Precision Resistors are known to produce products that are stable at cryogenic temperatures however their cost can often be a prohibitive feature. Lamb [93] found that inexpensive thin film resistors are suitable for moderate accuracy at cryogenic temperatures. As a result most resistors used in this thesis are thin film resistors, except where high resistances are required and thick film resistors have to be used. In these cases the products with the lowest temperature co-efficients have been selected. A full list of the components can be found in Appendix C.

All the components used in this thesis are surface mount devices (SMD) as these packages have the lowest parasitic capacitances and inductances. The components are re-flow soldered onto a low loss dielectric circuit board from Rogers. The tracks are kept as short as possible and have been milled using our CNC machine. The initial reasoning behind milling the circuit boards was to prevent etching chemicals from altering the dielectric properties of the substrate [96]. No improvements in circuit performance have been seen by using milling rather than etching but the CNC makes prototyping complex boards quick, accurate and easy to replicate.

The amplifier circuit design (see figure 6.8) is based upon that in [75] as we are operating at a similar frequency. The design consists of two GaAs transistors, the first of which is a dual gate MESFET (NE25139). This transistor consists of two identical FETs in cascode formation. This reduces the feedback capacitance from drain to gate (Miller capacitance), ultimately reducing the input capacitance of the amplifier [97]. The MESFET provides the gain and a high input impedance of 48 MΩ [75] which is needed to ensure that the amplifier does not load the resonator, as the amplifier's input impedance

appears in parallel with the resonator. The second transistor is a pHEMT (ATF35143) in common-drain configuration. As such, it does not provide voltage gain but acts as an impedance transformer. It takes the high output impedance of the MESFET and reduces it to match the 50 Ω of the coaxial output line. Without this impedance transformation very little signal would pass from the output of the amplifier to the rest of the detection system as most of the power would be reflected at the connection to the 50Ω cable.

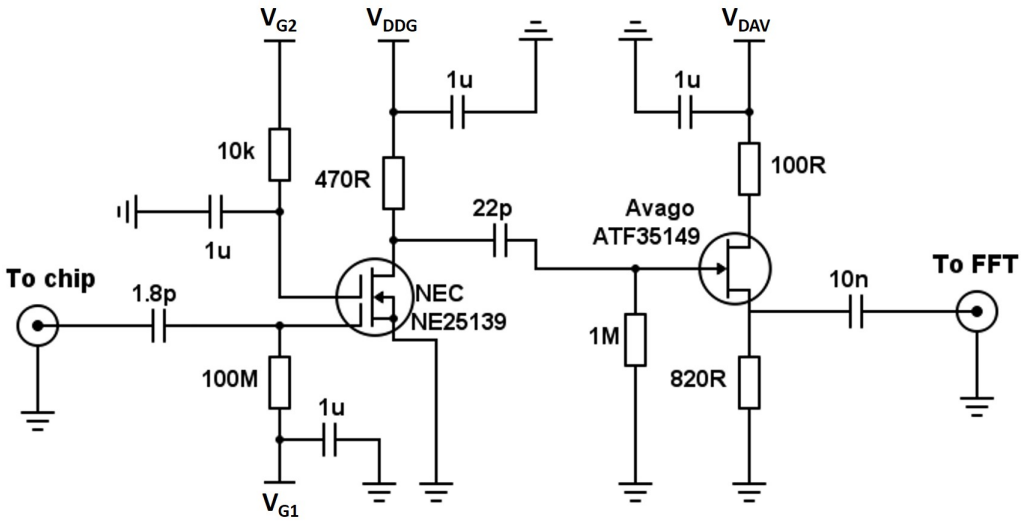

Figure 6.8: Cryogenic amplifier schematic where V_{DDG} is the voltage applied to the drain of the dual gate MESFET, V_{G1} is the gate one voltage, V_{G2} is the gate two voltage and V_{DAV} is the voltage applied to the drain of the pHEMPT transistor.

The final amplifier board (figure 6.9) is designed to fit into the top of the resonator housing so that it is shielded from external noise. The board contains the maximum number of vias possible in the space available to reduce the overall input capacitance of the board by shorting the top ground plane to the bottom ground plane.

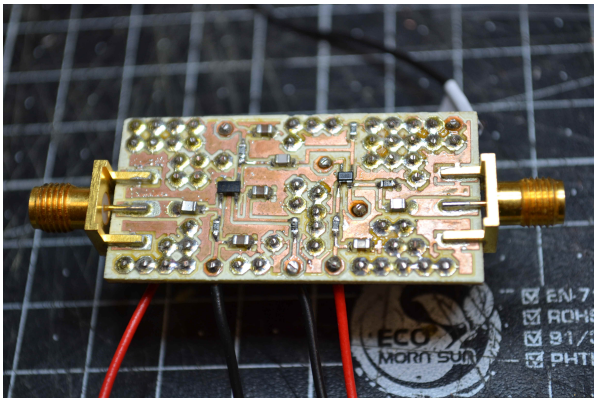

Figure 6.9: Completed cryogenic amplifier

The input and output characteristics of the amplifier were modelled by treating it as a hybrid π-network [98]. The input capacitance was calculated from the input admittance of the amplifier, $\mathrm{Y}_{\text{Amplifier In}} = Y_{11} + Y_{12}$ where the imaginary part of $\mathrm{Y}_{\text{Amplifier In}}$ is shown in figure 6.10. A fit to the equation of a 'real' capacitor gave an input capacitance of (5.2 ± 0.1) pF. At 30 MHz the output impedance, Z_{out}, was calculated as $(48 \pm 14)\ \Omega$ using

$$Z_{\text{out}} = Z_0 \frac{1 + \Gamma_{\text{out}}}{1 - \Gamma_{\text{out}}} \tag{6.3}$$

where

$$\Gamma_{\text{out}} = S_{22} + \frac{S_{12} S_{21} \Gamma_S}{1 - S_{11} \Gamma_S} \tag{6.4}$$

and Γ_S is the source reflection.

The voltage gain was measured as 11.48 dB using the S_{21} of the amplifier. All of these measurements were taken at 300 K with $\mathrm{V}_{DDG} = 8$ V, $\mathrm{V}_{G1} = -0.8$ V, $\mathrm{V}_{G2} = -0.2$ V and $\mathrm{V}_{DAV} = 2.1$ V.

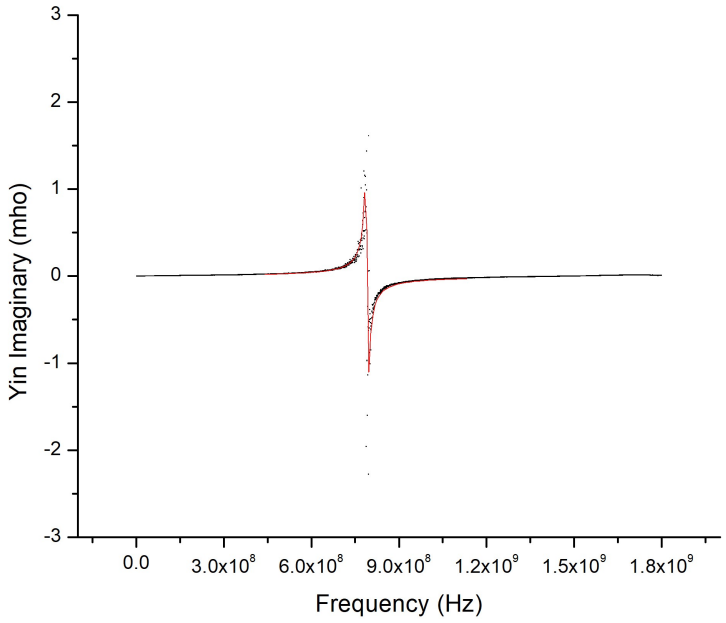

Figure 6.10: Imaginary part of the input admittance ($\mathrm{Y}_{\text{Amplifier In}}$) of the cryogenic amplifier

6.3 Resonator With Amplifer

From section 3.2 we know that the amplifier's input capacitance and impedance will load the resonator. This section investigates how much the amplifier loads the resonator and

if an optimal solution can be found. All of the plots in this section present the voltage response of the helical resonator without any external excitation and use the experimental setup in figure 6.11, where an additional amplifier is used at room temperature and the voltage is measured on a spectrum analyser. The 470 pF capacitor is used to maintain both a high Z_{21} which maximises the voltage signal of the electron and a high Z_{11} which maximises the width of the electron's axial dip. 470 pF was chosen as it matched the condition of being larger than the 250 pF threshold chosen in Chapter 3 and had previously been shown to work in [75].

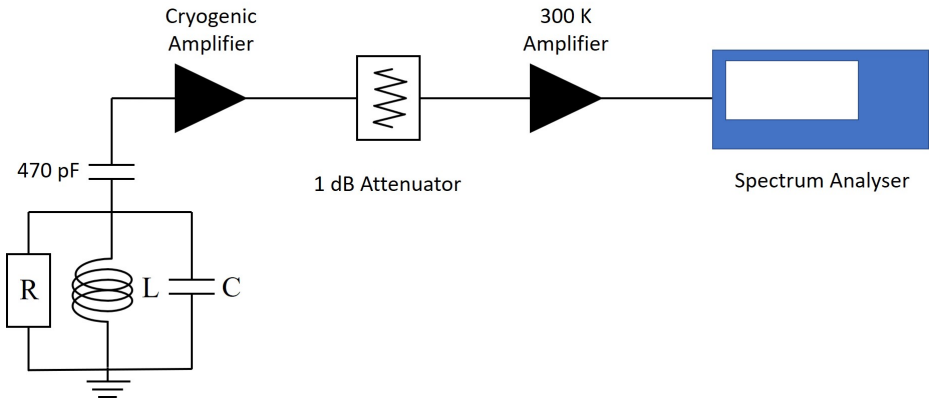

Figure 6.11: Connection of the helical resonator (represented as a parallel LCR circuit) to the cryogenic amplifier and room temperature electronics

The results of the voltage response of the resonator attached to the amplifier at 300 K and 4 K can be seen in figure 6.12. At room temperature the amplifier was biased with $V_{DDG} = 7.5$ V, $V_{G1} = -3.61$ V, $V_{G2} = -0.2$ V and $V_{DAV} = 4.95$ V. At 4 K the gate one biasing was adjusted to -1.51 V to maintain a good signal to noise ratio.

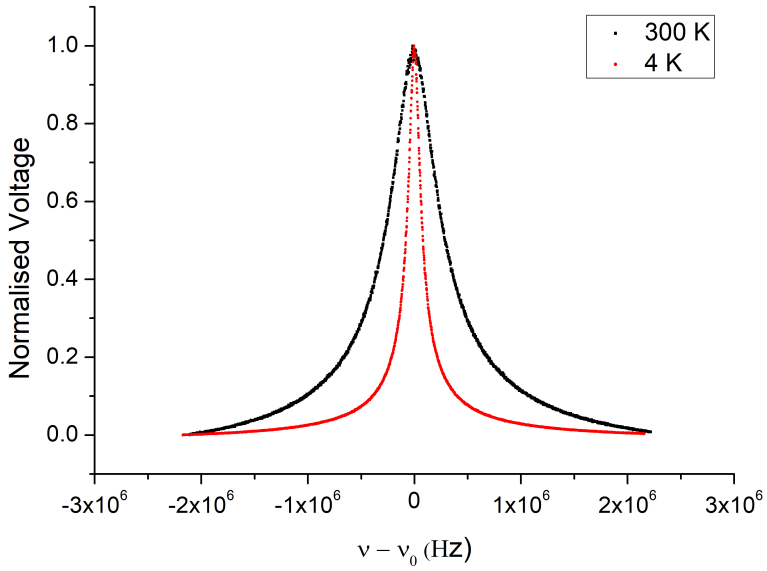

Figure 6.12: Resonator's voltage response when connected to the cryogenic amplifier at both 300 K and 4 K.

From the Lorentz fits to the data in figure 6.12 the loaded Q-factor of the resonator connected to the amplifier at 300 K is 86.45 and this increases to 455.79 at 4 K. This is much lower than the unloaded Q-factor of the resonator. To investigate this reduction the next section details the variation of the explicit capacitor at the input of the amplifier and section 6.3.2 explores the biasing of the dual gate transistor.

6.3.1 Investigating The Input Capacitance Of The Amplifier

The explicit surface mount capacitor placed at the input to the cryogenic amplifier PCB is investigated in this section. In figure 6.8 this is given as 1.8 pF. This in not the same as C_{in} in figure 3.6. Six different capacitors (100, 68, 43, 10, 5, 1.8) pF were used to investigate the effect of the input capacitor on the resonator's resonance frequency and Q-factor, which is depicted in figure 6.13.

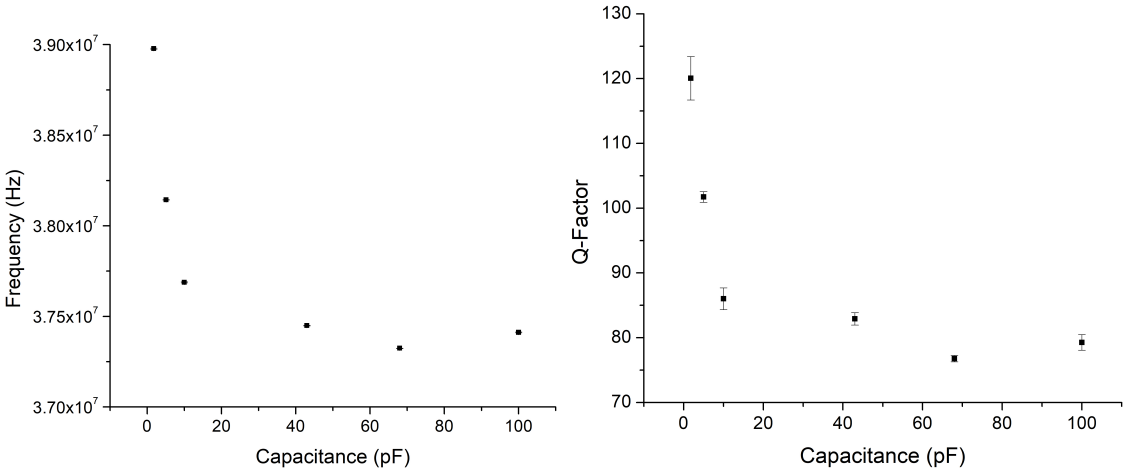

(a) Resonance frequency (b) Q-factor

Figure 6.13: Effect of the varying the cryogenic amplifier's explicit input capacitance on the helical resonator's resonance frequency and Q-factor. The data displayed here was taken at 300 K.

As the size of the capacitor increases, the frequency and Q-factor drops exponentially, in the same manner as that found in figures 3.10 and 3.11. This capacitor appears in series with the 470 pF capacitor at the top of the resonator, reducing the overall capacitive coupling between the resonator and the amplifier and therefore reducing the overall Z_{21} of the detection system. Despite this, in the short term, the input capacitor has been kept low at 5 pF to give a higher Q-factor but once the system is working this should be re-visited to find a better compromise which would lead to a higher Z_{21}.

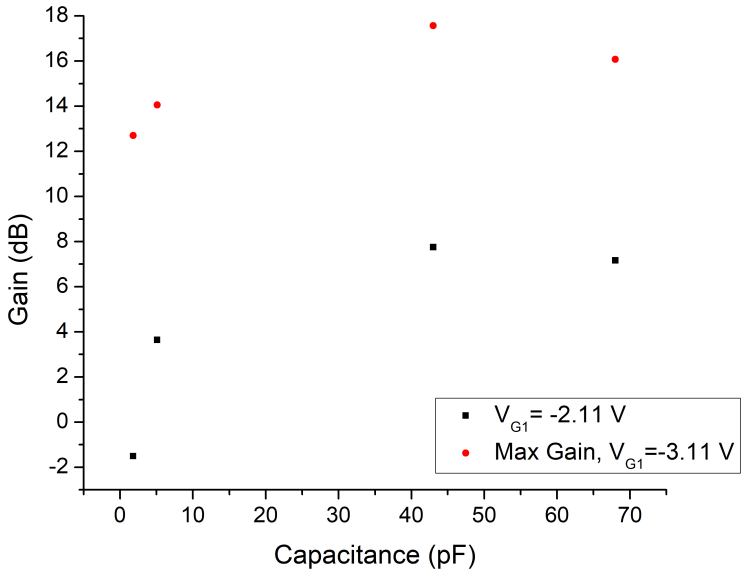

Figure 6.14: Effect of the varying the cryogenic amplifier's explicit input capacitance on the voltage gain with two different biasing conditions

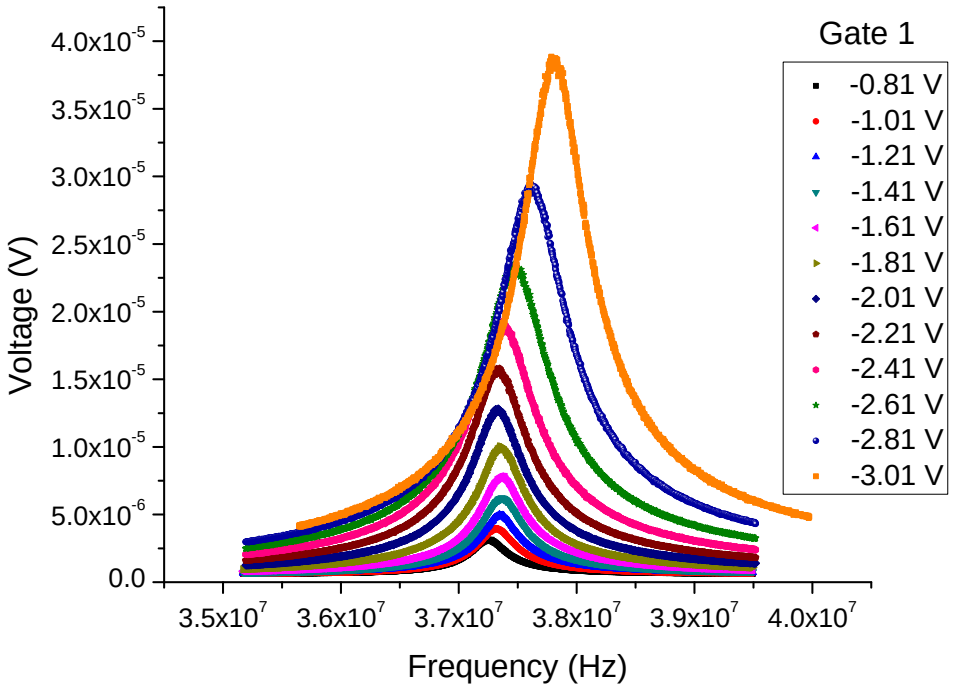

Figure 6.15: Effect of changing gate one on the voltage response of the helical resonator

Figure 6.14 shows the effect of changing the input capacitor on the voltage gain of the amplifier. The voltage gain is also dependent upon the biasing of the amplifier and therefore two different biasing conditions are shown. The highest gain was achieved with higher input capacitors but a gain of $\sim$ 14 dB with a 5 pF capacitor is sufficient to observe the voltage response of the helical resonator at both 300 K and 4 K.

6.3.2 Investigating Gate 1

The voltage applied to gate one of the dual gate transistor not only affects the gain of the amplifier but also the resonance frequency of the helical resonator. Figure 6.15 shows the voltage response when gate one was varied and all other biasing was kept the same. Figures 6.16a and 6.16b show the effect of changing gate one more explicitly.

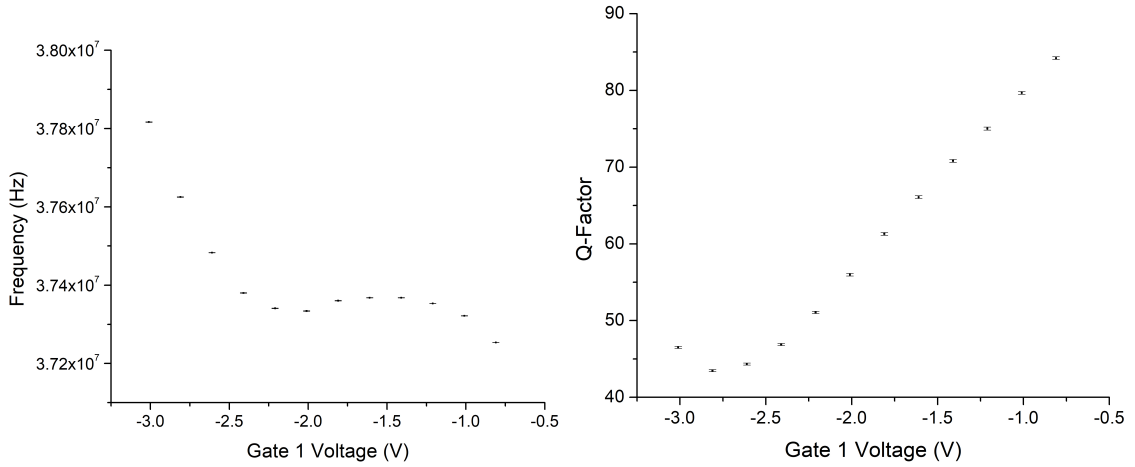

(a) Resonance frequency (b) Q-factor

Figure 6.16: Effect of the voltage applied to gate one of the dual gate transistor on the resonance frequency and Q-factor of the helical resonator

As the gate one voltage becomes more negative the resonance frequency increases slightly but the Q-factor drops by almost half. Therefore, a compromise must be chosen to choose a gate one voltage which maximises the Q-factor even though it decreases the resonance frequency slightly. All of the data presented in this section was taken at room temperature but similar results are seen at 4 K.

These results are explained by the channel of gate one closing as the voltage applied to it becomes more negative. This increases the drain to source resistance which is seen by the resonator due to a small gate to drain capacitance, which is described by the Miller effect. The result on the detection system is that the drain to source resistance appears in parallel with the effective resistance of the resonator, reducing the overall Q-factor of the system.

6.4 Superconducting Transmission Line

Once the helical resonator has been coupled to the cryogenic amplifier it must be prepared to be coupled to the Geonium Chip. Chapter 3 stated that the connection was to be made with a superconducting transmission line and this section describes the manufacture and testing of such a line.

The fabricated short superconducting transmission line is based upon the design in [99]. The first design (shown in figure 6.17) of our transmission line consists of eleven NbTi wires[3] of 250 μm diameter, one central wire is the signal path and all the other

[3]Supercon 1.5:1 monofilament T48B-M

wires form a shield. Each wire was stripped of its enamel and copper cladding before being encased in PTFE heat shrink[4]. The dielectric of the transmission line was made from three layers of PTFE with grooves milled out for the wires. The wires and the layers are glued together using Permabond POP Primer and Permabond 2050 Cyanoacrylate. The primer is particularly important as PTFE is a notoriously difficult material with which to create bonds. Once constructed the capacitance was measured, using an LCR meter, to be 21.75 pF/m. This is almost five times lower than standard cryogenic coaxial cables[5] used in rest of the experimental setup.

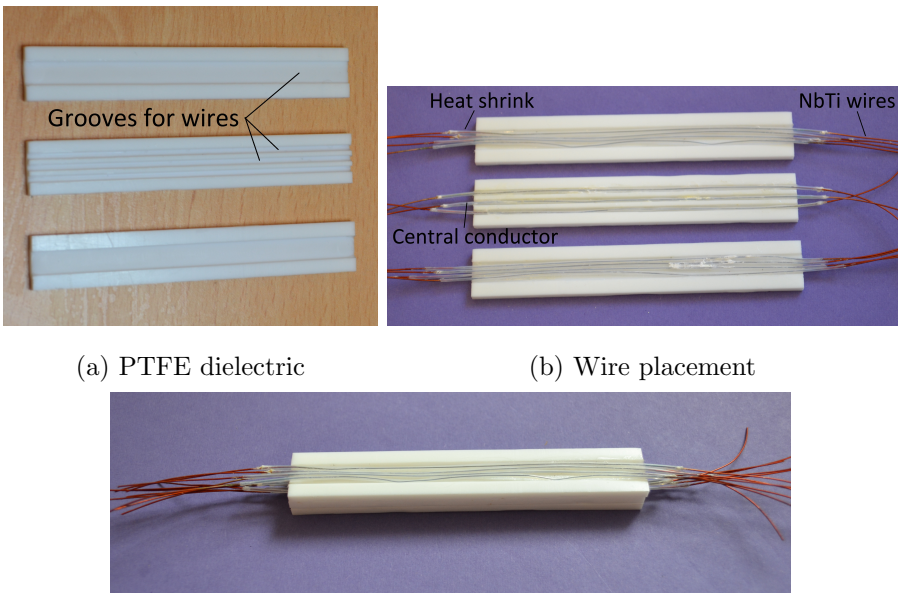

(a) PTFE dielectric (b) Wire placement

(c) Completed transmission line

Figure 6.17: Superconducting transmission line

However, a design such as this is very restrictive due to its rigidity and the lack of space in our cryostat. Therefore, the design was improved by J.Pinder to the more flexible approach shown in figure 6.18. In this design the PTFE is machined into discs through which the NbTi wires are threaded. The transmission line can now be manipulated into any shape and in the next section it is tested with the resonator and cryogenic amplifier.

[4] Adtech HST30T/R

[5] Allectra coaxial cables with 115 pF/m

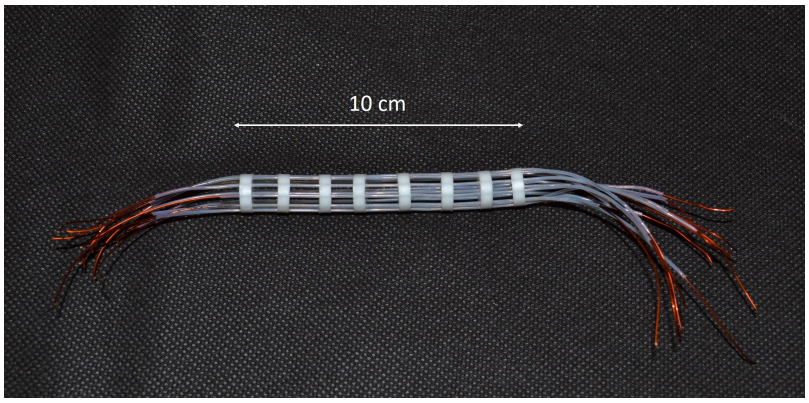

Figure 6.18: Flexible superconducting transmission line designed and manufactured by J.Pinder

6.4.1 Transmission Line With Resonator And Amplifier

Figure 6.19 shows the effect of connecting the transmission line to the resonator and placing the lid on the resonator housing which contains the cryogenic amplifier. The transmission line causes a frequency reduction due to its intrinsic capacitance (ΔC) which can be calculated from the the reduced frequency (f_2) and the original frequency (f) using

$$\Delta C = C\left(\frac{f_2^2}{f^2} - 1\right), \tag{6.5}$$

where C is the capacitance of the system before the connection to the transmission line was made. This equation assumes that the frequency shift is caused purely by the capacitive load of the transmission line, which is an oversimplification as the transmission line will also have an intrinsic inductance which contributes to the change in frequency. However, it allows an estimation of the capacitance added to the system, which using equation 6.5 gives the capacitance of the new flexible transmission line as 4.74 pF. This means that its capacitance per unit length is 23.7 pF/m which is slightly larger than the initial design but an acceptable price to pay for the added flexibility that it provides.

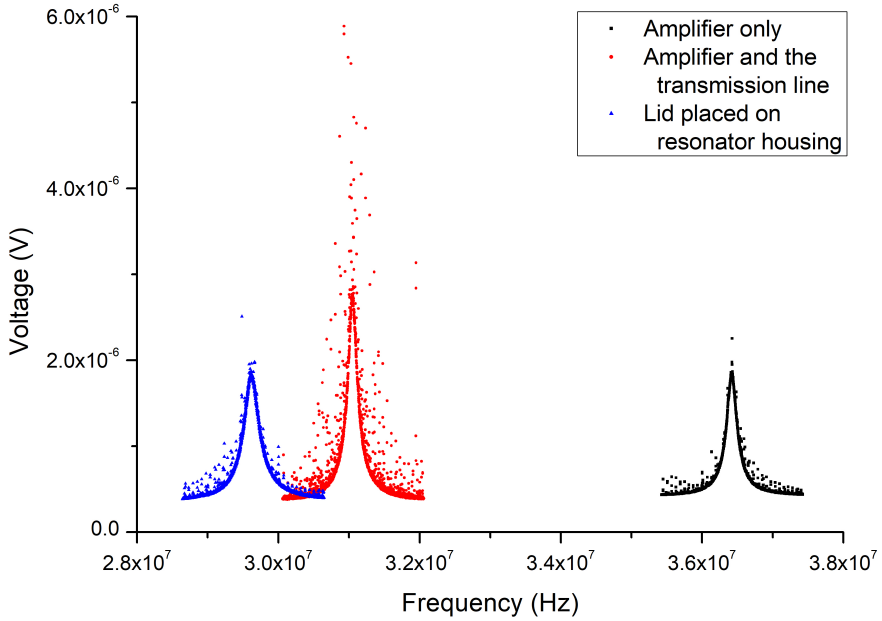

Figure 6.19: Voltage response of the helical resonator when; only the amplifier is connected to it (black), both the amplifier and the transmission line are connected (red) and finally with both the transmission line, the amplifier and the lid secured onto the resonator housing (blue). The red data shows a large amount of noise on the signal which is due to the transmission line acting as an antenna when one end of the the line is open.

6.5 Detection System Connected To Geonium Chip

The detection system is now ready to be connected to the Geonium Chip. Throughout this section the Geonium Chip is connected to the wafer probe system depicted in figure 4.4. A sketch of the detection system connected to the chip can be seen in figure 6.20 where there are no DC voltage lines connected to the trap, only the detection electronics.

This setup was used to produce the plot in figure 6.21 which shows the resonator's voltage response (without any excitation) as each part of the system is connected together. The blue line shows the resonator connected to the amplifier and the transmission line. The red line shows the amplifier, resonator and transmission line connected to the probe card with the probes lifted away from the surface of the chip. Finally, the black line shows the voltage response of the resonator when the probes are lowered on to the surface of the Geonium Chip. Each connection adds capacitance and causes the resonance frequency to reduce. This can be used to estimate the capacitance of the probe card in the same manner as the transmission line, using equation 6.5, to give 1.48 pF.

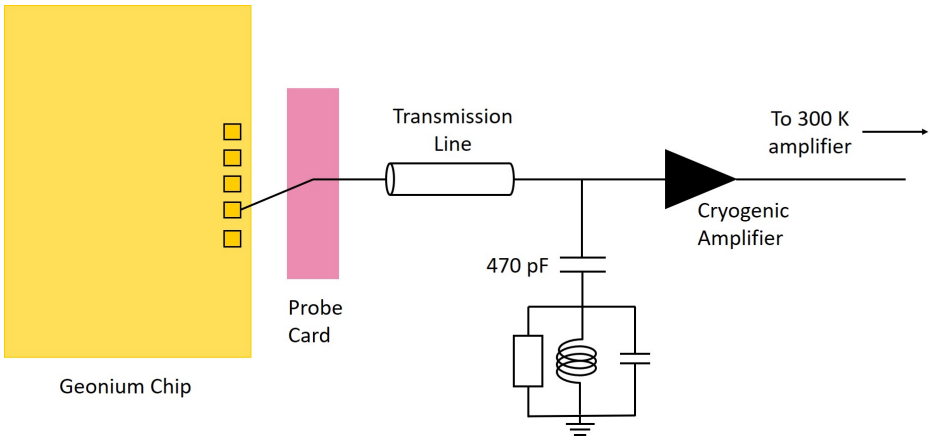

Figure 6.20: A sketch of the detection system connected to the Geonium Chip where the contact pads of the chip have been exaggerated for clarity.

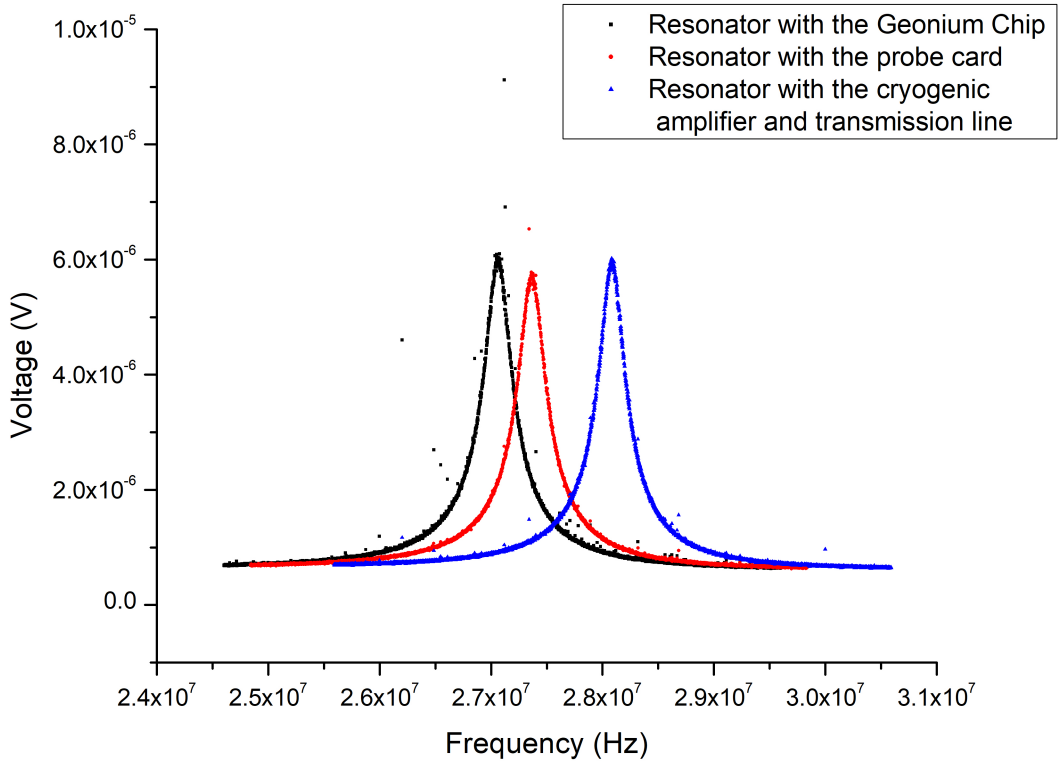

Figure 6.21: Voltage response of the resonator as steps are taken to attach the detection system to the Geonium Chip. The blue data shows the resonator attached to the cryogenic amplifier and the superconducting transmission line. The red data shows the above connected to the probe card but with the probes lifted away from the surface of the chip. The black data shows the voltage response when the probes are lowered on to the chip's contact pads.

The trap voltage lines now need to be connected to the chip but each of these voltage lines carry low pass filters to prevent noise from causing the trap voltages to fluctuate.

Connecting these voltage lines to all but the left compensation does not affect the detection system. However, connecting a voltage line with its corresponding low pass voltage to the left compensation causes the resonator signal to disappear because the signal is going to ground through the low pass filter. To prevent this from happening a high impedance block was added to the voltage line leading to the left compensation. The trap wiring now looks like figure 6.22.

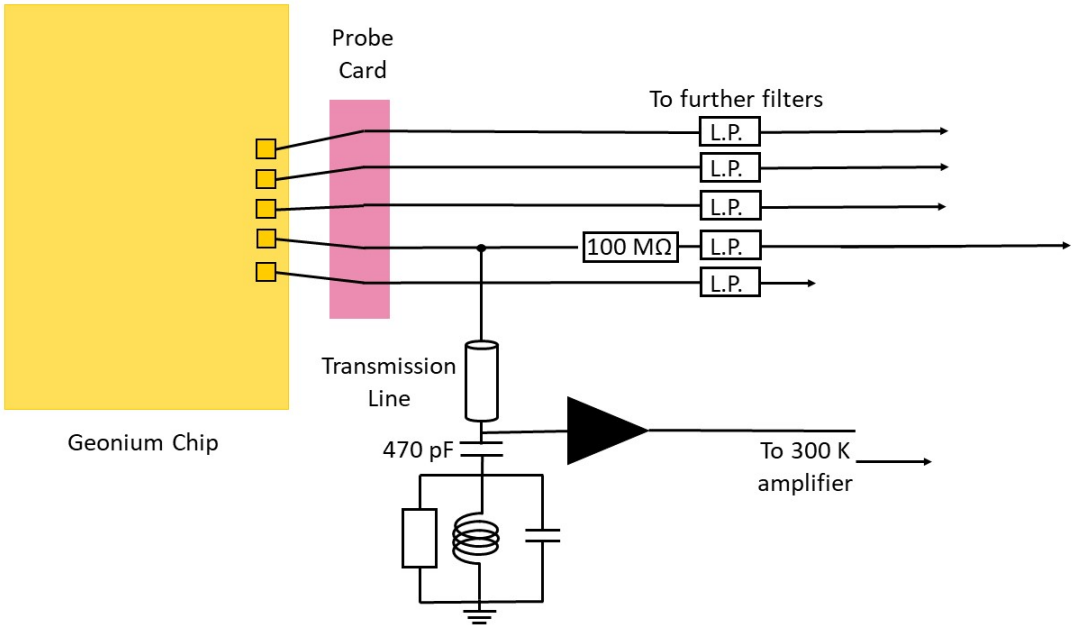

Figure 6.22: The Geonium Chip connected to the low pass filters (L.P.) of the voltage lines and the detection system with a 100 MΩ high impedance block.

Testing this configuration at 4 K gave the voltage response in figure 6.23. The Q-factor was 218 which can still be greatly improved but is sufficient for detecting a cloud of electrons. It is not however sufficient for detecting a single electron which would require a Q-factor of greater than 600. For example, a Q-factor of 670 would give an axial dip width of 67 Hz and the frequency fluctuations caused by the trapping voltages would be ∼13 Hz, allowing the dip to be differentiated from the noise.

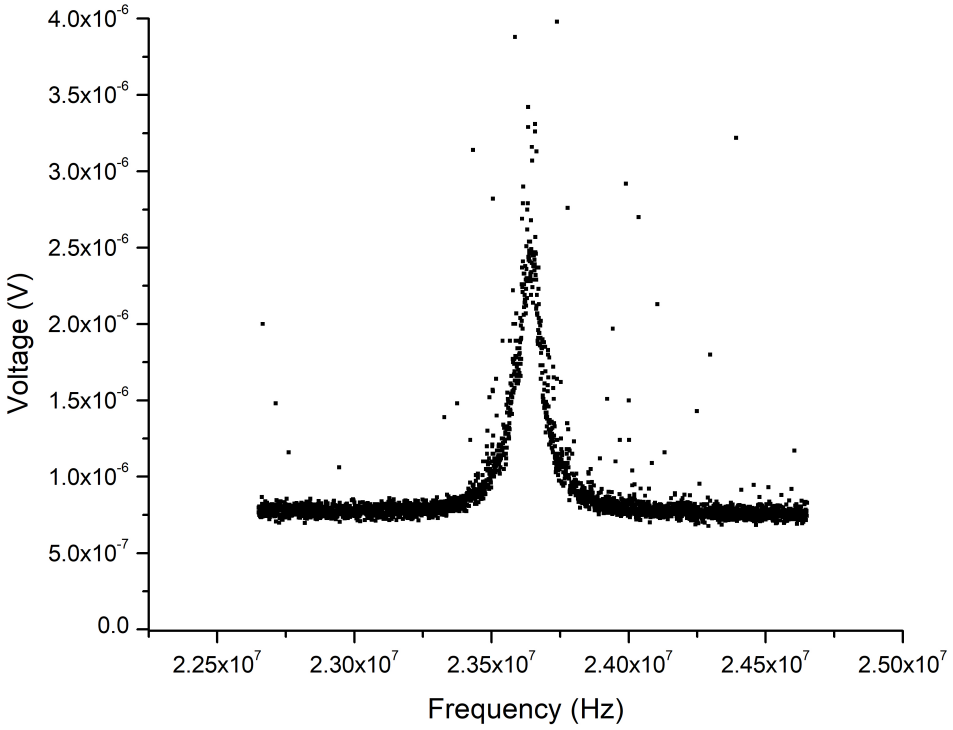

Figure 6.23: Voltage response of the helical resonator at 4 K without any external excitation

Once the chip was connected to the detection system the first trapping attempts were made. Unfortunately, these were unsuccessful and the possible reasons for this are discussed in chapter 8.

Chapter 7

Experimental Setup

This chapter focusses on the main experimental setup which includes; the cryostat, the cryogenic wiring and the techniques used to thermalise the system, in particular the currents required for the magnetic field prototype. The method for generating electrons within the trapping region is also discussed and demonstrated at both room temperature and 4 K. Finally, once the entire setup was assembled, additional noise was found on the detection signal from the helical resonator. Section 7.3 explores the noise sources and the steps taken to remove the noise from the detection signal.

7.1 Cryostat

The experiment consists of two vacuum vessels; the first has already been introduced in section 4.5 and is formed around the trapping region, the second, much larger vacuum chamber contains all of the necessary wiring and is built around a 4 K pulse tube (Sumitomo SRP-062B). The pulse tube has a two stage cold head with the first stage capable of reaching 60 K with a 30 W load and the second stage capable of reaching 4.2 K with a 0.5 W load. The pulse tube is sealed to a four-way cross of feedthrough flanges to form the top of the main vacuum chamber and together these are sealed to the bottom of the chamber. When the chamber is opened the top section is lifted out of the bottom using a ceiling hoist. Once sealed using ISO O-rings the chamber is evacuated using a pumping line connected to a flange at the bottom of the chamber and an Agilent TPS Compact pumping system. An exploded view of the top and bottom sections of the main vacuum chamber can be seen in figure 7.1 and the closed system can be seen in figure 7.2.

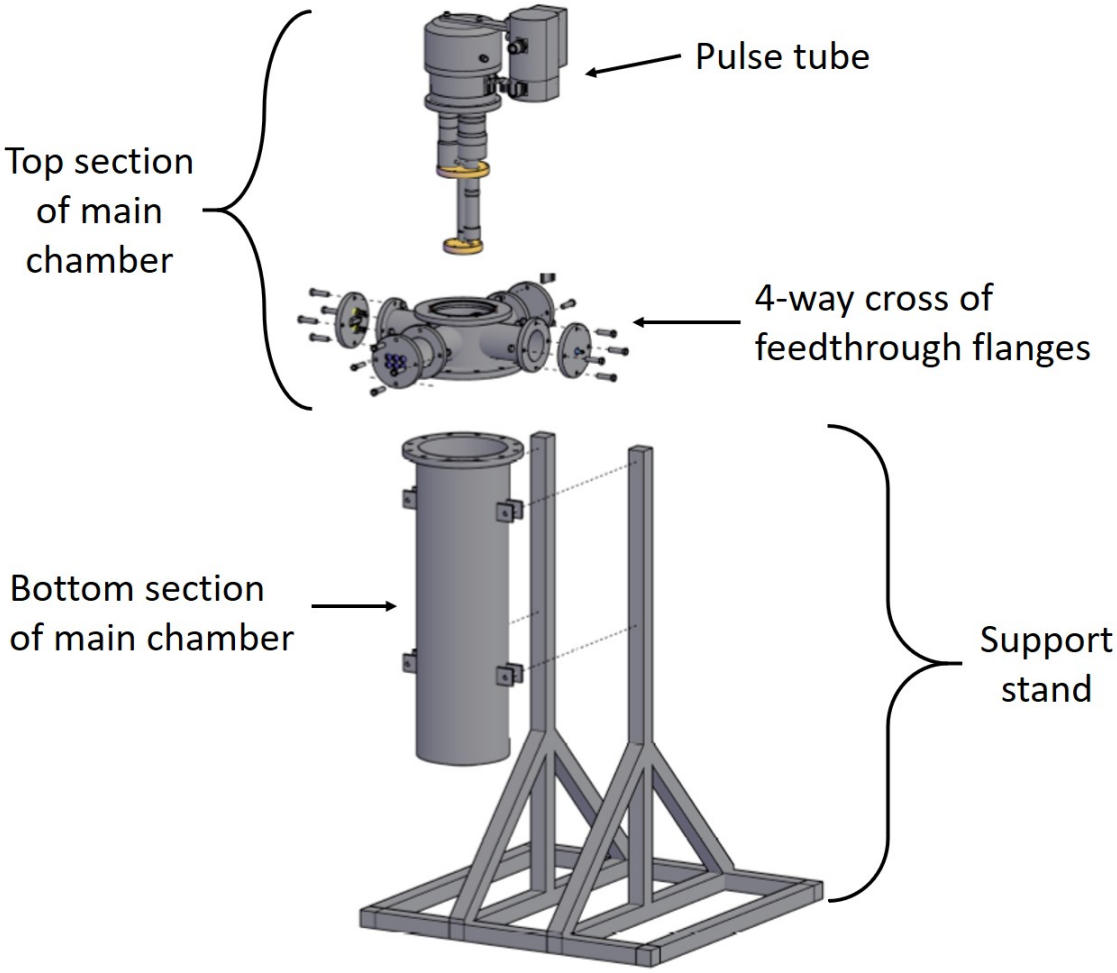

Figure 7.1: Exploded view of the main vacuum chamber showing the pulse tube, 4-way cross of feedthrough flanges and the bottom section of the chamber with its support stand [1].

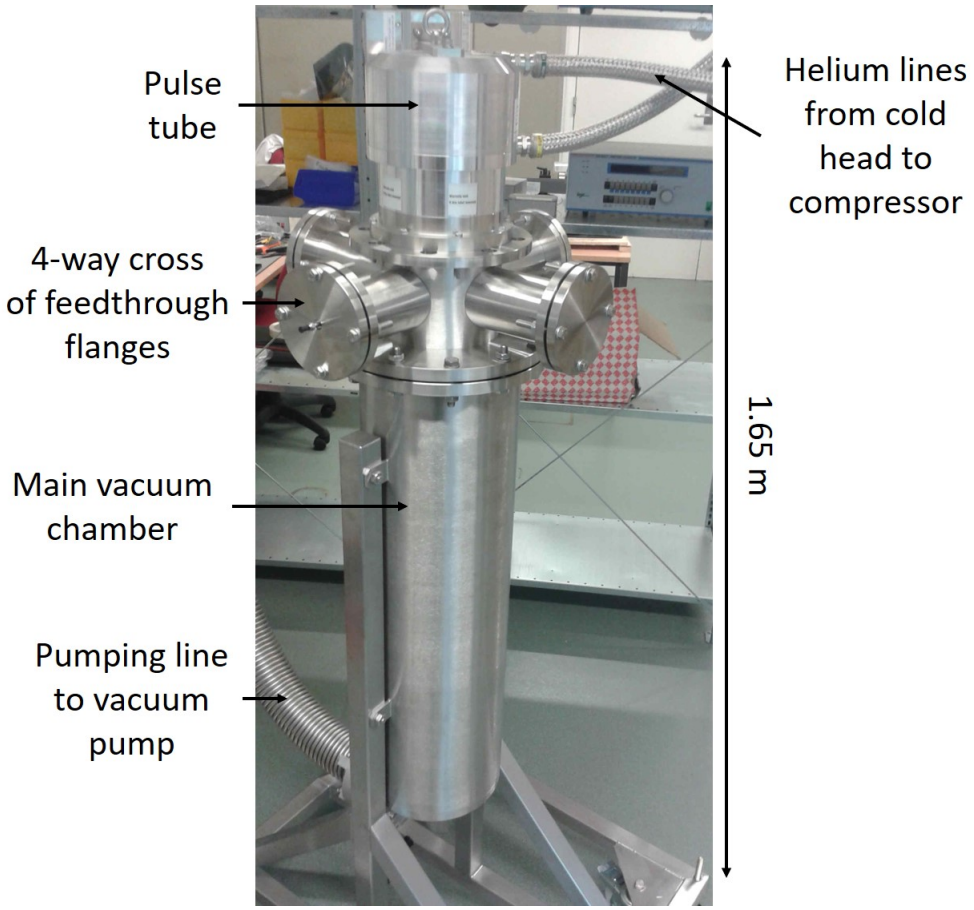

Figure 7.2: Photograph of the main vacuum chamber whilst closed [1]

7.1.1 Thermalisation Of Radiation Shields

To minimise radiative heating of the cryostat each stage of the cold head is wrapped in a radiation shield made from high purity aluminium. The surface of the aluminium is first mechanically polished and then electro-polished to minimise its emissivity[1]. Emissivity is the ratio of the thermal energy radiated from a material's surface to that radiated from a blackbody at the same frequency and temperature [100]. Therefore, the inside of each of the shields requires a surface with a low emissivity to prevent them from re-radiating the thermal energy that is incident upon their outer surface. An exploded diagram of the radiation shields is shown in figure 7.3 where the inner dimensions of the 4 K shield define the experimental region as having a height of 480 mm and a diameter of 124 mm.

[1]Emissivity of oxidised aluminium = 0.11 (200°), unoxidised = 0.028 (100°), highly polished = 0.08 (low temperatures) [100]

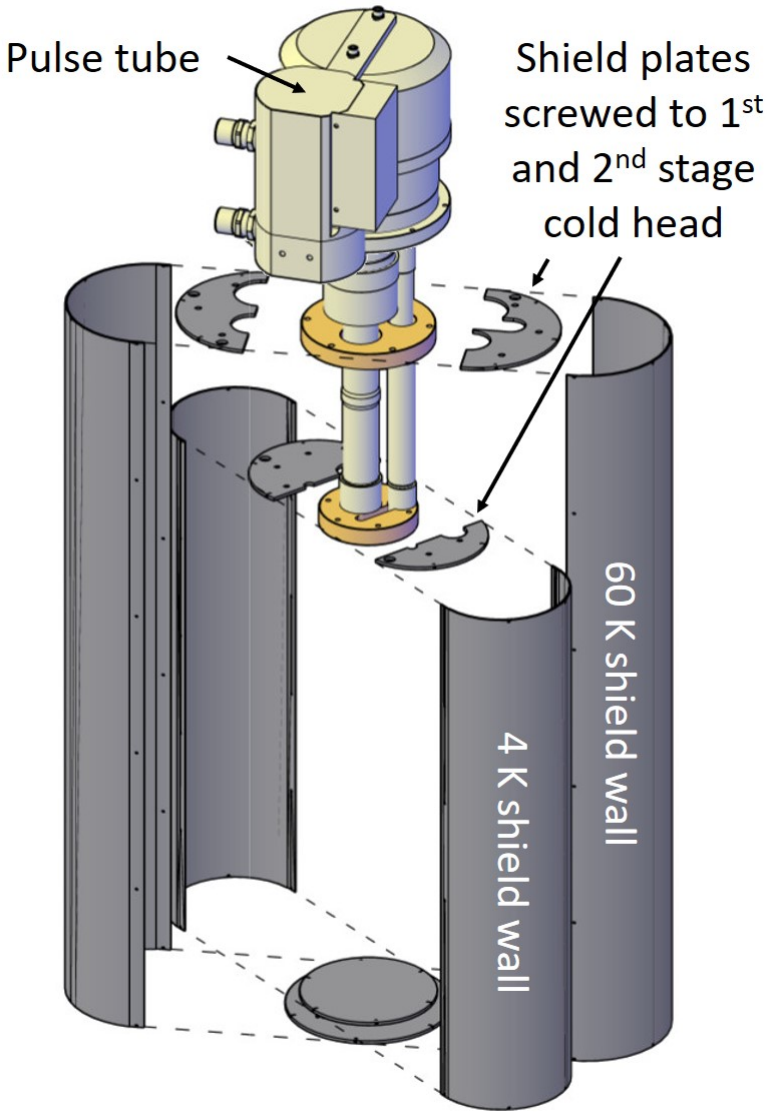

Figure 7.3: An exploded diagram of the aluminium radiation shields which fit around both the 1st and 2nd stage cold head to prevent radiative heating [1]

As mentioned in section 6.1 there were difficulties in reaching the base temperature of the cryostat and it was decided that a single layer aluminium shield was unable to provide adequate radiation shielding. The first step in improving the radiative shielding was to wrap the aluminium shields in multi-layer insulation (MLI) which was purchased from Scientific Magnetics. The MLI or 'superinsulation' as it is also known, is made from ten layers of double aluminised Mylar with a polyester spacer between each layer. The MLI wrapped shields can be seen in figure 7.4. This extra insulation along with other thermalisation steps such as wire anchoring, coaxial line thermalisation with attenuators and the tightening of loose bolts, was capable of allowing the cryostat to reach its base temperature.

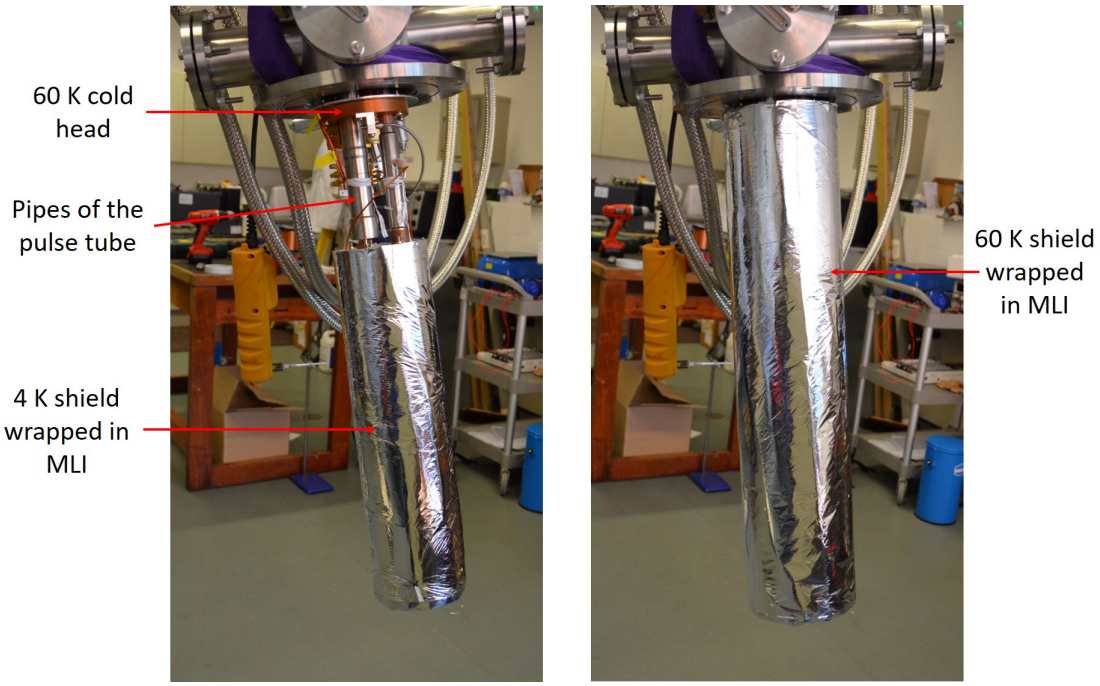

Figure 7.4: The 4 K (left) and the 60 K (right) radiation shields wrapped in multi-layer insulation to reduce radiative heating of the experimental region

The radiation shields are secured to the cold head at each temperature stage by aluminium plates, as seen in figure 7.3. The shield walls were mounted to the plates via six 1.6 mm screws. However, over time these mounting screws became less secure and an alternative mounting scheme was devised by J.Pinder. Not only was this new scheme more robust but it also allowed the shield walls to more tightly screwed to the plates. A tight connection is required to allow the shield walls to thermalise. The new mounting brackets (shown in figure 7.5) also increased the surface area of the shield wall in contact with the shield plate which helps to further thermalise the shield.

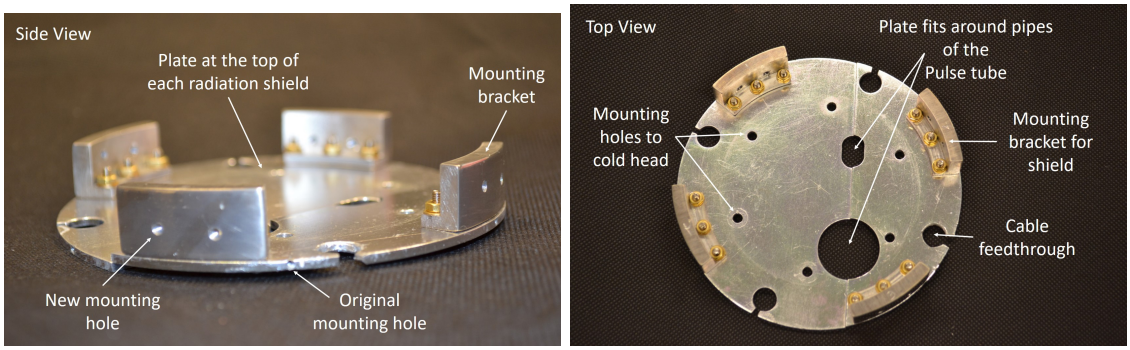

(a) Side view of shield plate

(b) Top view of shield plate

Figure 7.5: New scheme to mount the shield walls onto the plates at the top of the shield

7.2 Cryogenic Electronics

7.2.1 Trap Voltages

To maintain a stable axial frequency the voltages supplied to the trap's electrodes must also be free from fluctuations. In addition, to achieve a harmonic potential the optimal tuning ratio requires voltages which can be controlled to 1 μV. This is achieved with precision voltage calibrators from Time Electronics which have a voltage range of 0 - 22 V and an adjustability of 1 μV.

Additionally, any connections in the DC voltage lines have been made with crimps or screws to avoid the use of solder. This is due to the large thermoelectric mismatch of power between copper and lead-tin solder which can cause fluctuations in the voltages supplied to the electrodes [2]. The voltage fluctuations (V_{AB}) caused by these connections can be calculated using [3]

$$V_{AB} = Q_{AB}(T_1 - T_2) \tag{7.1}$$

where Q_{AB} is the Seebeck coefficient of material A with respect to material B and $T_1 - T_2$ is the temperature difference between the two materials. The Seeback coefficients for common materials with reference to copper can be seen in table 7.1.

Table 7.1: Seebeck coefficients of common metals [2, 3]

Material	$\mu V/°C$
Copper	<0.2
Gold	0.2
Copper-Beryillium	0.9
Lead-Tin	3
Copper oxides	>1000

Therefore, the larger the Seebeck coefficient of the material, the larger the thermoelectric voltages it causes over the same temperature difference. Copper oxides can cause particularly large thermoelectric voltages and any pure copper surfaces were cleaned with Scotch-Brite^{TM} to ensure that there were no oxides present. Where a direct copper to copper connection has not been possible, gold or beryllium copper has been used as they have a low Seebeck coefficient.

At each temperature stage (300 K, 60 K and 4 K) the trap voltages are thermalised and filtered to reduce noise and prevent heat from reaching the lower temperature stages.

The filters consist of a lowpass RC filter with a bypass made using a GaAs antiparallel Schottky[2] diode (figure 7.6) [101]. The diodes allow an applied RF signal to bypass the RC filter and reach the electrodes, in order to excite the cloud of electrons. This will be crucial for exciting high temperature electrons to leave the trap, thereby reducing the total electron number of the cloud and cooling the remaining electrons [102]. Additionally, this bypass could be used for sideband coupling, which requires RF and MW frequencies to couple the magnetron or cyclotron motion of the electron to its axial motion. This coupling allows quanta of energy to move from one motional mode to another, cooling the target mode [65].

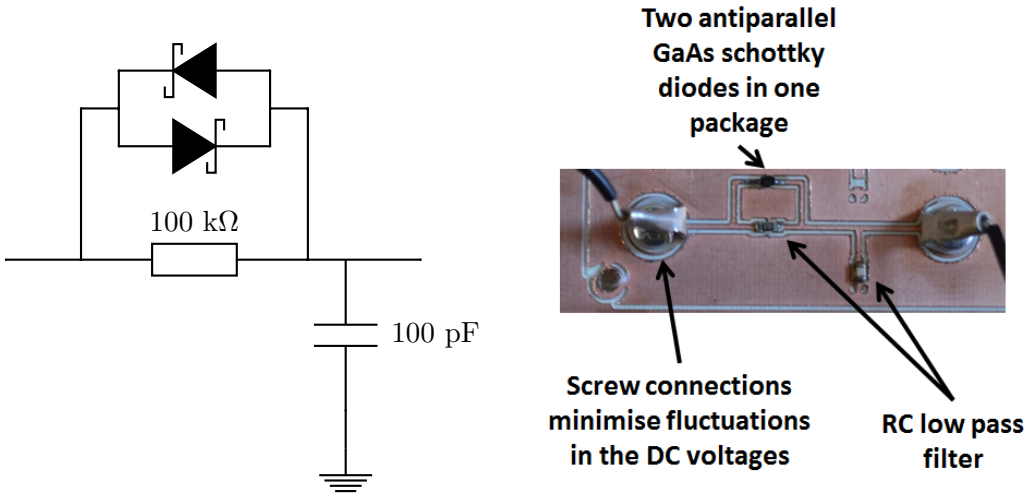

(a) Circuit diagram [101] (b) Example trap voltage filter

Figure 7.6: Low pass filters on each of the trap voltage lines at 300 K, 60 K and 4 K. Left - circuit diagram including a schottky diode bypass for RF and MW frequencies. Right - example low pass filter with two antiparallel GaAs Schottky diodes in one SMD package and two ring terminals to provide a screw connection rather than a solder connection.

To initiate the diode bypass the signal amplitude must be above the forward voltage of the diode. The effect of increasing the signal amplitude can be seen in figure 7.7, as the peak to peak height of the signal is increased, the amount of signal flowing through the bypass increases.

Each filter board is milled from a Rogers low loss dielectric board and connected to the next filter board via a copper loom of twisted pairs. The loom is thermalised by wrapping it around the pipes of the cold head and the struts of the 4 K region. It is then connected to the filter board using ring terminals which are crimped to the copper wires and screwed

[2] Aeroflex Metelics SMGS21

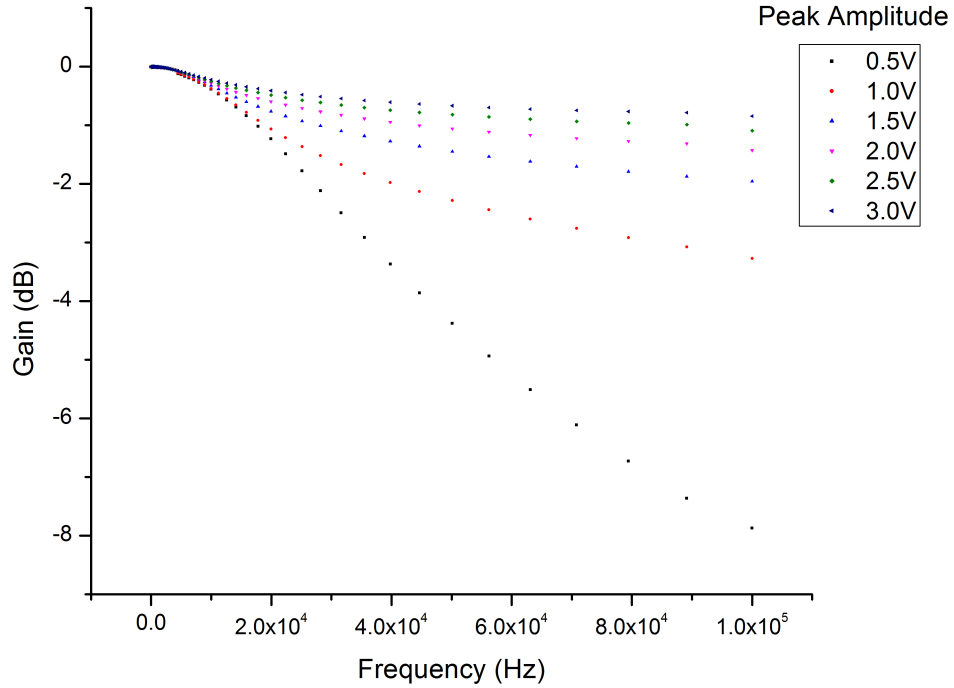

Figure 7.7: Variation of filter gain with voltage peak and frequency

to the board. The ring terminals are tin plated copper and copper to copper connections are required so the tin has been stripped from the ring terminals. This was achieved using the electrolysis of sodium hydroxide (120 g/L) at 50°C with the ring terminal set as the anode. The cathode is a stainless steel bolt and a voltage of $2.2 - 2.6$ V is sufficient to begin to strip the tin from the copper. After approximately five minutes the electrolysis will leave an oxidised copper terminal, free of tin. The oxides can be removed by leaving the ring terminal in 99% glacial acetic acid for five minutes. Figure 7.8 shows the three stages of stripping the tin from the copper terminal.

Figure 7.8: Stages of stipping tin from copper

The final filter board is connected to the probe card of the the chip using a copper loom and screw terminals. The probe card has been modified to facilitate these screw terminals and provide a copper-copper connection all the way to the contact pads of the chip. The modified probes can be seen in figure 7.9.

Figure 7.9: Modified wafer probes designed to maintain a copper-copper connection from the voltage calibrators at 300 K all the way to the contact pads of the Geonium Chip

An overview of the trap voltages can be seen in figure 7.10.

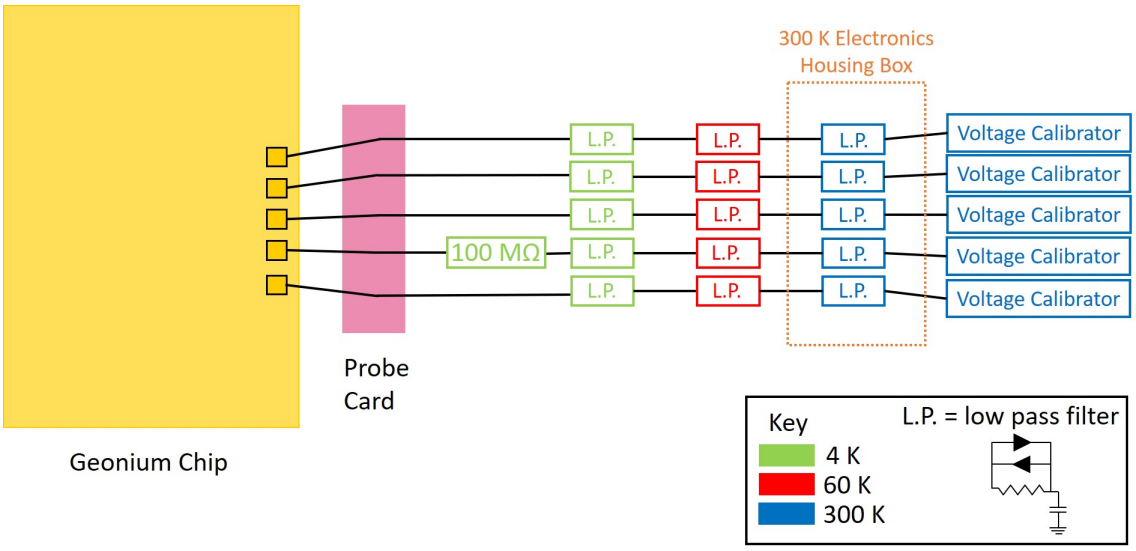

Figure 7.10: Overview of the trap wiring

7.2.2 Amplifier Voltages

The cables carrying the voltages needed to bias the cryogenic amplifier also need to be thermalised upon entering the cryostat. As a result, the signals pass through low pass filters without the schottky bypass used for the trap voltages. The amplifier voltages travel down constantan wires as copper to copper connections are not required and constantan allows less heat to flow from the 300 K region to the 4 K region. The constantan wires are 110 μm in diameter and are twisted together into a loom which is soldered directly to the filter boards. The amplifier does not have a separate filter board at 4 K, like the trap, because there are 1 μF capacitors to ground on each of the bias lines as they enter the board of the cryogenic amplifier. These channel any AC noise on the bias voltage to ground, keeping the biasing of the transistors stable. An overview of the amplifier wiring can be seen in figure 7.11 where the 300 K amplifier is also shown as part of the signal chain.

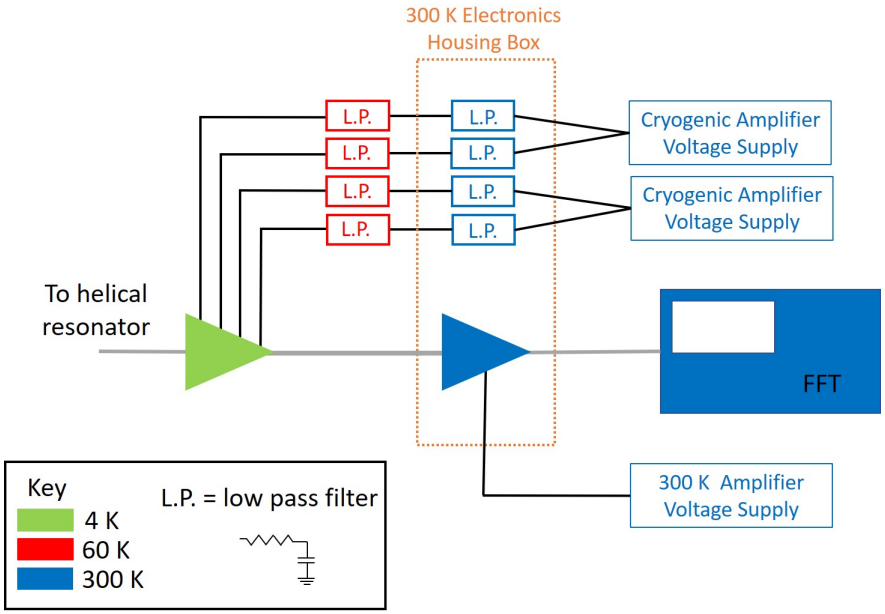

Figure 7.11: Overview of the cryogenic amplifier wiring with the signal chain (grey) to the 300 K amplifier and FFT.

7.2.3 Magnetic Field Currents

The magnetic field of the magnetic field prototype described in section 5.2 scales linearly with the current supplied to it. Therefore, the thermalisation of the current wires needs to be designed to pass as much current as possible without raising the temperature of the experimental region above a few kelvin and certainly not beyond the critical temperature of niobium titanium. The heat load needs to be carefully managed and fully thermalised at both the 60 K temperature stage and the 4 K temperature stage.

The currents enter the cryostat through screw connections to power feedthroughs capable of passing 20 A. From the 300 K flange down to the 60 K cold head the currents pass through 1.6 mm diameter enamel coated copper wire. This is the optimum diameter ($\varnothing$) of copper wire to pass 10 A from 300 K to 4 K and is calculated from [103]

$$\varnothing = 2\sqrt{\frac{LI}{(3.5 \times 10^6)} \cdot \frac{1}{\pi}}, \tag{7.2}$$

where L is the length of the wire and I is the current. This equation is a compromise which balances the effect of Joule heating, which is reduced with a large diameter wire, and the heat conduction of the wire, which is reduced by using a small diameter wire.

To thermalise the copper wires they were wrapped around the pulse tubes above the 60 K section. This means that they are above the outer 60 K shield and therefore subject to radiation emanating from outside the cryostat. As a result, both the pulse tubes and

the wires are wrapped in more than one layer of MLI to reduce the effect of the radiation and prevent the temperature of the system from rising. Figure 7.12a shows the first layer, where the two smaller pulse tubes are wrapped individually in insulation and the wires are wrapped around the larger pulse tube and held in place with Mylar tape. Figure 7.12b shows the second layer, where the smaller pulse tubes are encased in one piece of MLI and the windings of the wires are wrapped in another piece of MLI. Finally, both of the tubes are wrapped in one piece of MLI (figure 7.12c).

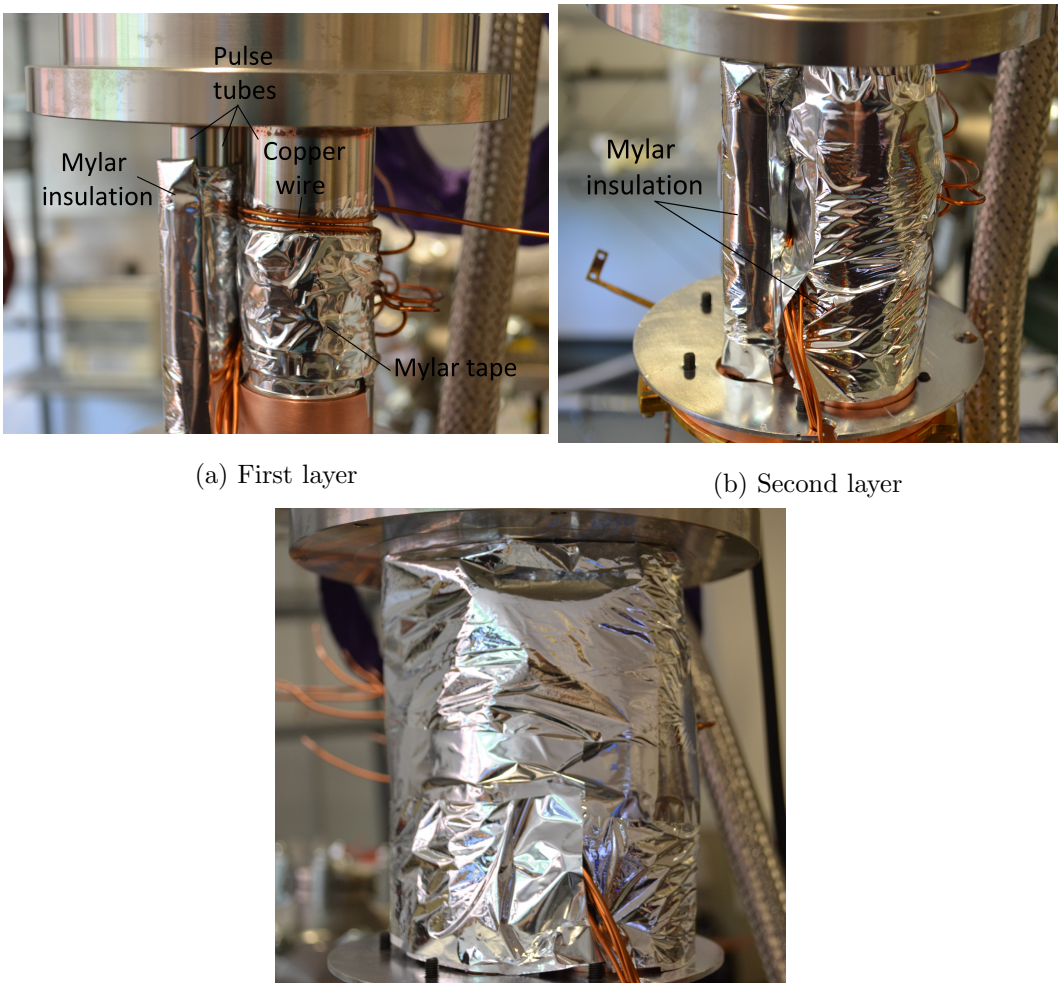

(a) First layer

(b) Second layer

(c) Third layer

Figure 7.12: Thermalisation of 1.6 mm diameter copper wires carrying the currents required for the magnetic field prototype. The wires are wrapped around the large pipe of the pulse tube, above the 60 K cold head, and then wrapped in MLI superinsulation to prevent radiation from raising the temperature of the system. Additionally the two smaller pipes of the pulse tube are also wrapped in MLI.

Once the copper wires reach the 60 K temperature stage they are soldered to solder tags which are screwed to busbars. These busbars allow the current to pass from an input solder

tag to an output solder tag and dissipate heat into the busbar itself, which is machined from oxygen free copper. The oxygen free copper is polished to provide as smooth a surface as possible and then gold plated to prevent the build up of copper oxides. Both of these techniques help to maximise the heat flow across the boundaries of the busbar. The busbar is mechanically screwed to a gold plated copper faceplate but electrically isolated from the plate using kapton tape and PEEK inserts around the holding screws, as shown in figure 7.13. This faceplate is directly screwed to the 60 K cold head and N grease is used between the interface of the faceplate and cold head to maximise heat flow across the boundary of the plates. In this manner the heat from the current wires is sunk at the 60 K temperature stage where there is more cooling power.

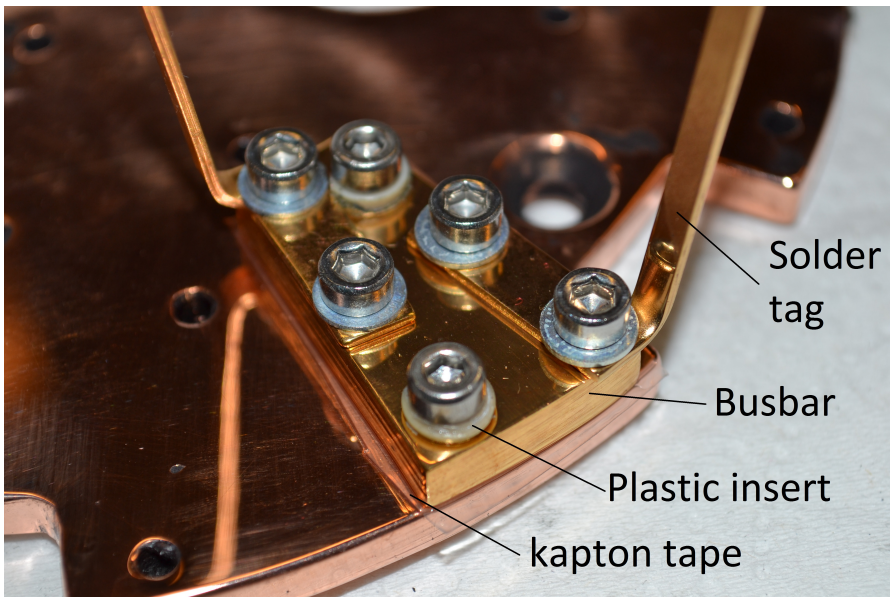

Figure 7.13: Input and output solder tags screwed to a busbar which in turn is screwed to the 60 K faceplate.

Copper wires cannot be used in the next section because even an optimum wire size would produce a higher heat load than the second stage of the pulse tube is capable of dealing with. Therefore, the copper wire is replaced by superconducting tape[3]. The tape consists of a high temperature superconductor (RE)BCO (Rare Earth Barium Copper Oxide) with a silver outer layer encased in a copper stabilizer which can be soldered directly to the solder tags. However, care must be taken not to overheat the tape and damage the superconducting layer. Once soldered the tags are gold plated to prevent oxides forming. The superconducting tape is then coated in kapton tape to ensure that it is electrically insulated from the rest of the experiment. The tape runs from the 60 K

[3]Superpower Inc. 2G HTS with copper stabilizer

faceplate to the 4 K faceplate and is thermalised by wrapping it around the pulse tubes between the two cold head stages, as shown in figure 7.14.

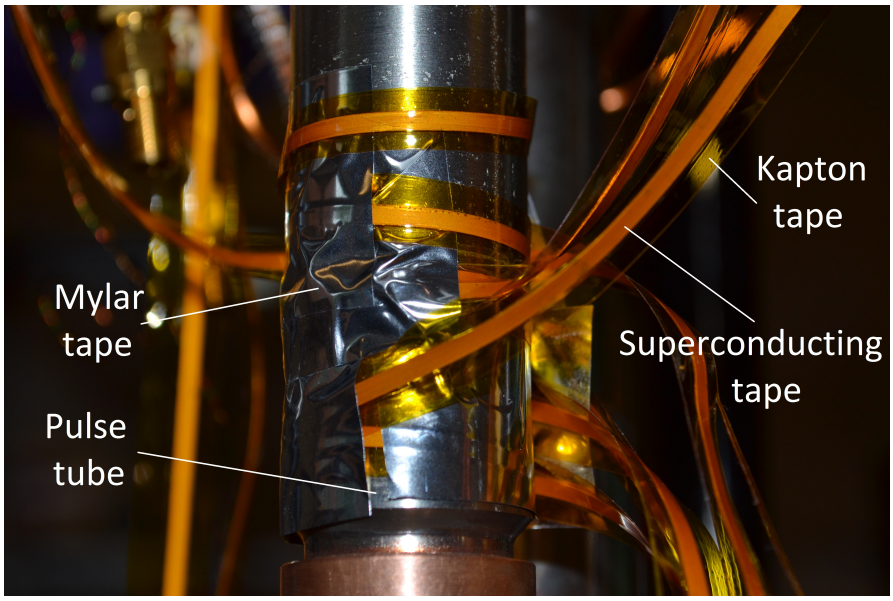

Figure 7.14: Thermalisation of superconducting tape

Once the superconducting tape reaches the 4 K temperature region it is screwed to the 4 K faceplate in the same manner at it was to the 60 K faceplate. However, the 4 K faceplate is of a slightly different design due to the lack of space in this region. Both faceplates can be seen in figure 7.15.

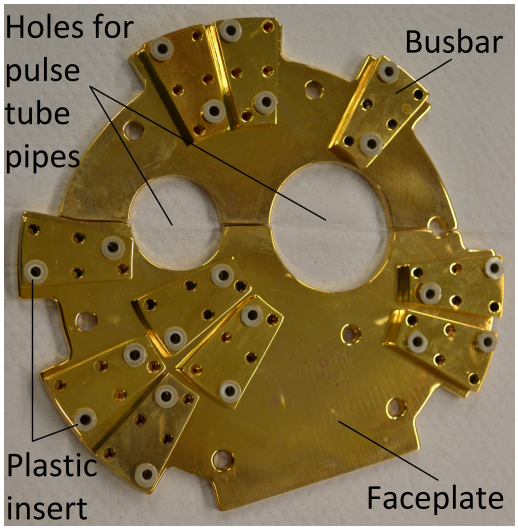

(a) 60 K faceplate

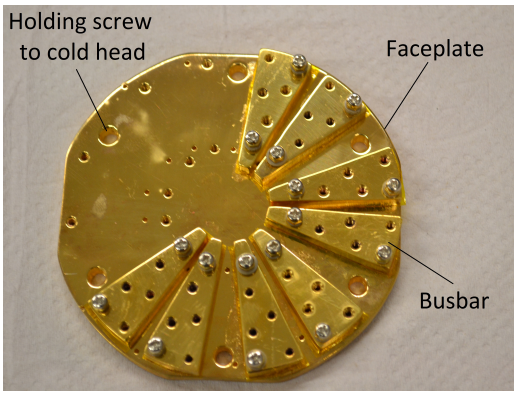

(b) 4 K faceplate

Figure 7.15: Faceplates and busbars at each temperature stage

The final section of the wiring leads directly to the magnetic field prototype and

therefore consists of the niobium titanium wires that were used to make the prototype. These wires are soldered to the tags using a meandered section of wire (as shown in figure 7.16) to ensure that the maximum surface area possible is in contact with the solder tag.

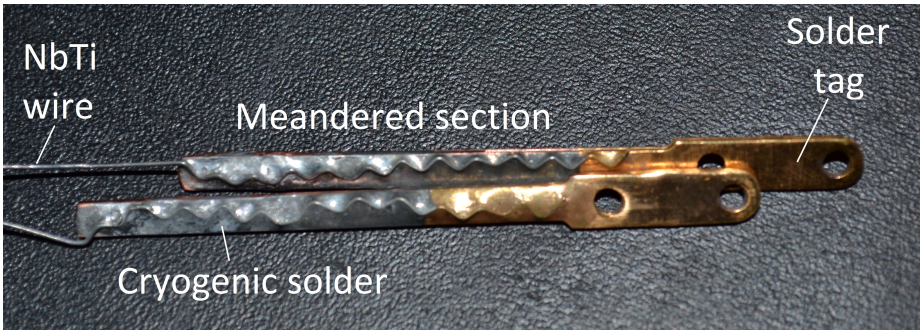

Figure 7.16: Meandered section of NbTi on a solder tag

The full wiring diagram for the magnetic field currents can be seen in figure 7.17.

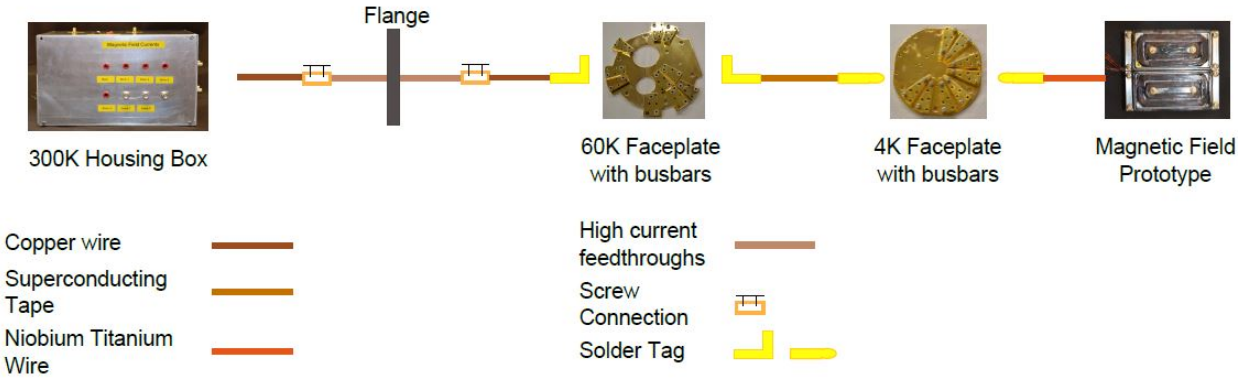

Figure 7.17: Wiring diagram for the magnetic field prototype

7.2.4 Head Load On The 60 K And 4 K Temperature Stages

The Sumitomo test report for the pulse tube states that the first temperature stage can maintain a temperature of 60.1 K with a 30 W load and the second temperature stage can reach 3.97 K with a load of 0.5 W. Therefore, the heat load at each stage must be managed to ensure that each stage is not overloaded and the pulse tube can reach its base temperature. The following section includes the calculations of the heat load caused by the wiring.

Current Carrying Wires

Copper current carrying wires can be optimally sized according to equation 7.2 and as a consequence will all have the same minimium heat flux [103] for each temperature range

$$\dot{q} = 84\text{mW/A for (300 - 4)K} \tag{7.3}$$

$$\dot{q} = 18\text{mW/A for (77 - 4)K.} \tag{7.4}$$

The heat load for the superconducting tape cannot be easily estimated due to its complex structure. However, once the tape is superconducting the heat load should be negligible as the current will be running through the superconducting layer, negating any heat load due to Joule heating.

Voltage Carrying Wires

The heat flow down voltage carrying wires can be calculated from tabulated thermal conductivity integrals [2] for two arbitrary temperatures using

$$\dot{q} = \frac{A}{L}\int_{T_1}^{T_2}\lambda(T)dT = \left(\frac{A}{L}\right)\left[\int_{4K}^{T_2}\lambda(T)dT - \int_{4K}^{T_1}\lambda(T)dT\right] \tag{7.5}$$

where A is the wire's cross-sectional area, L is the wire's length, $\lambda(T)$ is the material's temperature-dependent thermal conductivity, and T_1 and T_2 are the temperatures at the beginning and end of the wire.

Calculated Heat Loads

Table 7.2 and 7.3 show the heat load at each temperature stage of the cryostat calculated using the above equations. Due to careful design of the cryostat wiring both loads are well below the maximum load of the pulse tube. As a result, the base temperature of the entire system (containing all necessary components for the experiment) is 3.97 K.

Table 7.2: Heat load from 300 K to 60 K when the magnetic field currents are set to zero

Quantity	Use	Material	Diameter	Heat Load
5	Trap Voltages	Copper	90 μm	3.29 mW
4	Amplifier Voltages	Constantan	110 μm	0.172 μW
6	Hall Voltages	Copper	0.08 mm	0.519 mW
2	Hall Currents	Copper	0.10 mm	0.84 mW
12	Temperature Sensors	Constantan	110 μm	0.516 μW
8	Magnetic Field Currents	Copper	1.6 mm	3.36 W
Total				**3.365 W**

Table 7.3: Heat load from 60 K to 4 K

Quantity	Use	Material	Diameter	Heat Load
5	Trap Voltages	Copper	90 μm	1.87 mW
4	Amplifier Voltages	Constantan	110 μm	0.023 μW
6	Hall Voltages	Copper	0.08 mm	1.77 μW
2	Hall Currents	Copper	0.10 mm	0.18 mW
8	Temperature Sensor	Constantan	110 μm	0.046 μW
Total				**0.002 W**

7.3 Noise Reduction

Once all of the wiring was completed and the cryostat was cooled to 4 K, preparations were made for the first trapping attempts. The detection electronics were switched on and the voltage response was observed on the spectrum analyser. However, once the cables for the magnetic field currents were connected to the electronic housing box, the signal on the spectrum analyser became noisier, as seen in figure 7.18a. Switching on the current supply increased the noise levels, as seen in figure 7.18b, and switching on the current output caused the noise to increase further, as seen in figure 7.18c. Noise of this amplitude would obscure the signal of a cloud of electrons and render their detection impossible. This section therefore discusses the possible noise sources and their resolution to regain a clean detection signal at 4 K.

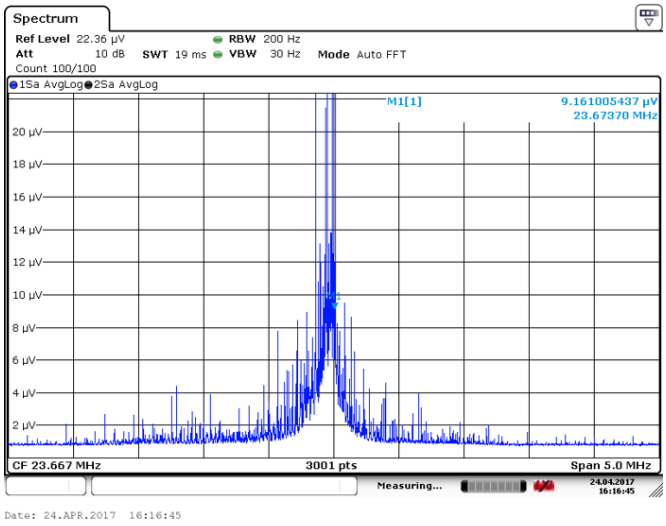

(a) Connecting the current cables

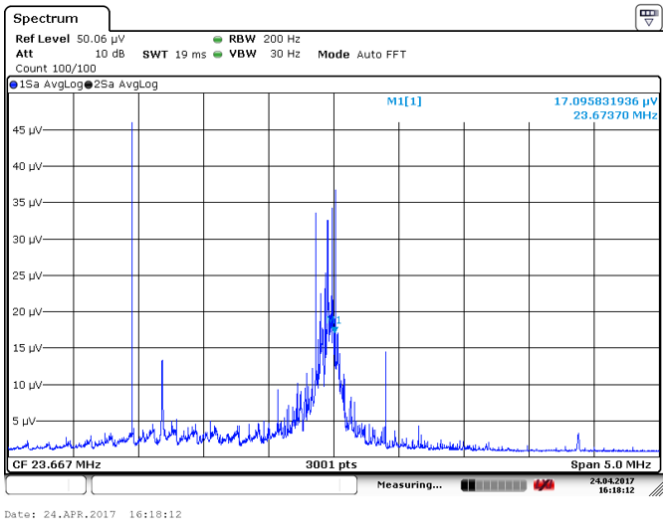

(b) Switching on the current supply

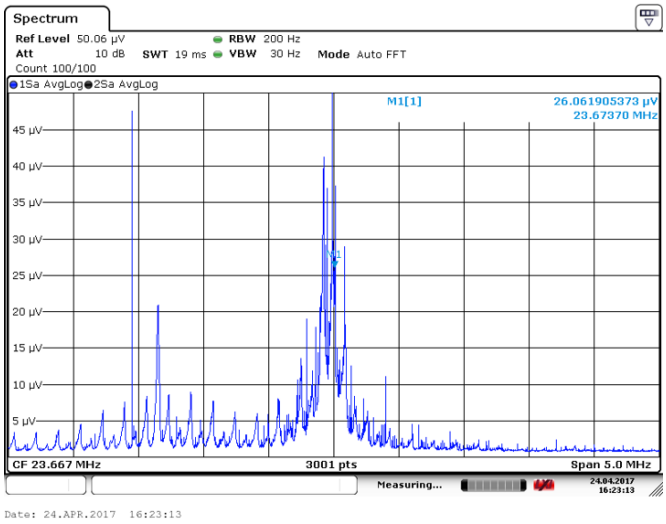

(c) Outputting the currents from the supply

Figure 7.18: Noise on the detection signal observed at 4 K. Noise was observed when the current cables were connected to the 300 K electronics box (figure 7.18a), the current supply was switched on (figure 7.18b) and was further increased when the currents were output from the supply (figure 7.18c).

7.3.1 Cabling

Cables can act as large antennas which pick up radiated noise from external sources and then conduct this noise into the system or re-radiate it, to be picked up by another cable. There are three ways that radiated noise can couple onto a cable: capacitive, inductive or electromagnetic. Capacitive coupling occurs due to stray capacitances between wires or traces when electric field induction is dominant. Inductive coupling occurs when the magnetic field of a current carrying loop induces a noise current in a second loop i.e. when magnetic field induction is dominant. Electromagnetic coupling is only significant when the source is close to the cable, where the electric and magnetic fields can be treated separately. Therefore, the steps to reduce capacitive and inductive coupling should suffice to reduce electromagnetic coupling [104].

Capacitive coupling can be reduced by increasing the distance between the offending conductors or by shielding each of them. However, capacitive coupling between the shield and the conductor still exists and therefore any noise that couples onto the shield can capacitively couple onto the conductor. To prevent this from happening, the shield should be grounded to provide the noise with a low impedance path to ground [105]. Therefore, all cables from power supplies must be shielded and additionally their shields must be grounded.

Inductive coupling can be reduced by minimising the area of any conducting loops, arranging them perpendicular to one another, or by shielding them [104, 105]. The magnetic field prototype requires multiple current loops which carry DC currents. To reduce inductive coupling at low frequencies, the forward and return cables must be shielded with the shield only grounded at one end of the cable (closest to the supply). Otherwise, the shields of the forward and return cable will form a ground loop between the supply and the 300 K electronics housing box. Additionally, the cables should be bundled together to reduce the area of the loop.

7.3.2 Power Supply Decoupling

No power supply is an ideal zero impedance current or voltage source. Therefore, they can couple the circuits connected to them and allow noise to flow from one to the other [105]. To counteract this all outputs from the power supplies are decoupled using low pass filters. Low pass filters can consist of a resistor-capacitor network or an inductor-capacitor network. There are pros and cons to both networks. A low pass filter needs to present a high series impedance to high frequencies. This is difficult to achieve with a resistor

as its response is not frequency-dependent and would require a large value resistor which would reduce the power supply voltage. On the other hand, an inductor-capacitor filter can provide more high frequency filtering without causing as much loss as a resistor [105]. However, inductors have to be chosen carefully to ensure that the DC current can pass without saturating the core. Inductors should also be shielded as they can pick up spurious magnetic fields and radiate the noise voltage that they are filtering out of the signal path. Due to the high currents required for the magnetic field prototype, the first decoupling filters that were built consisted of ferrite sleeves, in place of an explicit inductor, and a parallel arrangement of three capacitors. The capacitors help to filter noise over a larger frequency range and the theory behind this is discussed in more detail in section 7.3.5. The power supply decoupling filters can be seen in figure 7.19 where an additional ferrite sleeve was also placed directly on the current supply cables just outside of the housing box.

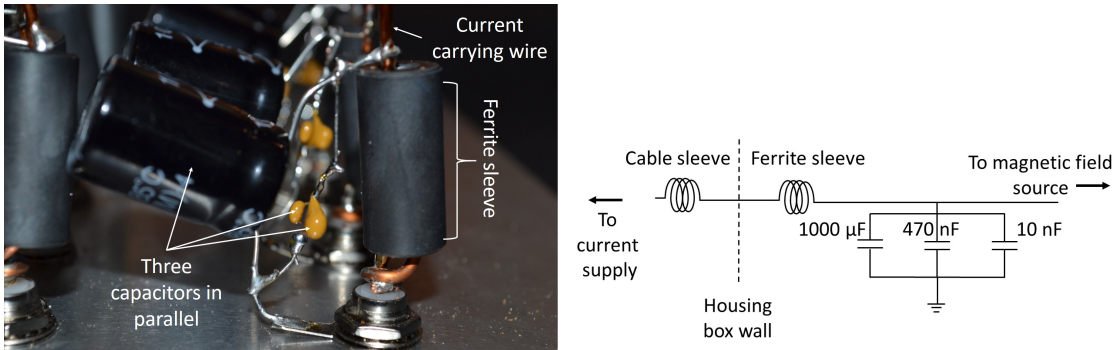

(a) Photograph of an LC filter inside the 300 K electronic housing box

(b) LC filter schematic

Figure 7.19: Power supply decoupling filter for the current supply

7.3.3 Results From Improving Cabling And Power Supply Decoupling

Once the cabling had been improved and the decoupling filters installed on the current wires, the noise on the signal was re-measured. The signal peak has reduced from 35 μV in figure 7.18c to 5 μV in figure 7.20. The repeating noise signals that dominated the noise floor in figure 7.18c have also been greatly reduced. However, there is still a considerable amount of noise on the detection signal, making the electron dip immeasurable. Therefore, to reduce the noise further, the noise contributions from the power supply were explored and multi-stage EMI filters were built.

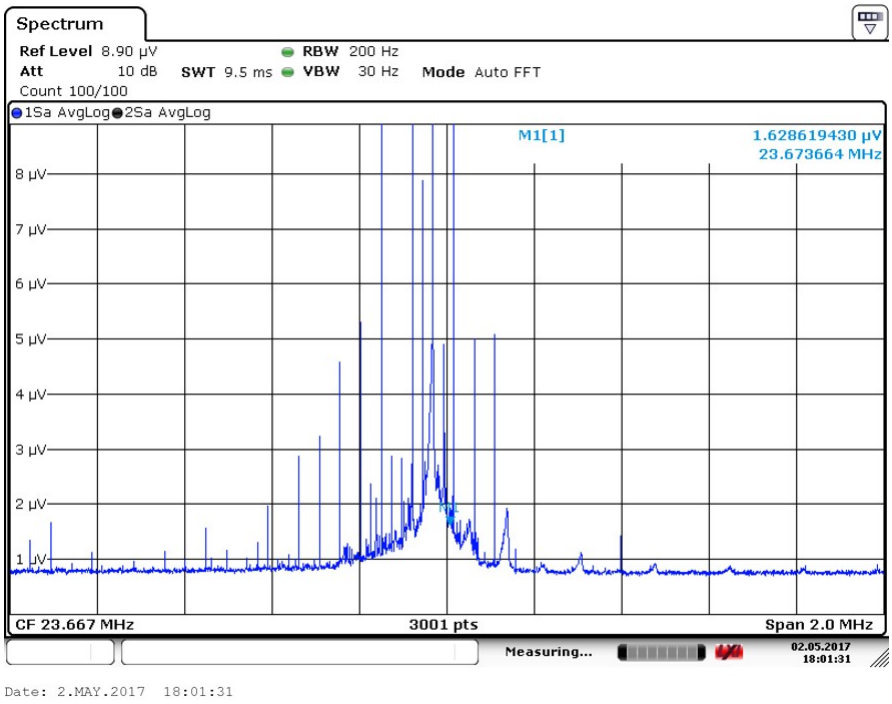

Figure 7.20: The noise observed on the detection signal following improvements made in the cabling and the decoupling of the power supply. In this plot the current supply was outputting currents to the magnetic field.

7.3.4 Noise Contributions From Switching Mode Power Supplies

The current supply used to provide the currents for the magnetic field prototype is a switching mode power supply (SMPS). SMPS are notoriously noisy, suffering from four main types of noise [104];

- Switching frequency - conducts along the output cable creating a ripple in the intended output.
- Ripple of the switching frequency - fluctuations in the swtiching frequency can radiate inductively from the supply at the harmonics of this frequency due to the square wave nature of the signal [106]
- Common-mode interference - caused by external noise sources coupling on to the ground plane and inducing a noise voltage in the parasitic resistances and inductances of the ground plane.
- Mains hum - results directly from the mains supply at 50 Hz. This is fully rectified within the supply to 100 Hz and conducts along the output rail [106].

Noise which conducts directly along the output cable, such as the noise caused by the switching frequency and the mains hum, is coupled in differential mode. Differential mode noise appears in series with the intended signal (also coupled in differential mode) and travels forwards on the output rail and backwards on the return rail, as shown in figure 7.21. Differential noise can be filtered out using LC filters with the capacitor connected between the output rail and the return rail [107]. This ensures that the noise shorts to the return rail and returns to the source before reaching the load.

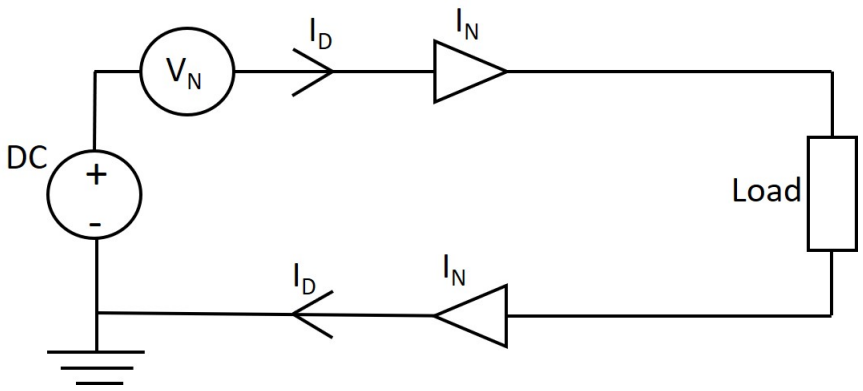

Figure 7.21: Differential mode noise coupling

Common mode noise is generated on the power supply's ground plane and parasitic capacitances between the ground and power supply's output channels cause this noise voltage to couple onto both the output rail and the return rail. The noise travels towards the load on both rails and returns along the ground plane due to a stray capacitance at the load, as depicted in figure 7.22. Common-mode noise cannot be filtered out with a capacitor between the rails because the noise signal is identical on both rails [107]. Common-mode noise can be suppressed with a common-mode choke which consists of a torodial ring and two counter wound wires. The common-mode noise causes a magnetic flux to accumulate in the toroid which then presents a high impedance to the common-mode noise. Magnetic flux caused by the differential forward current (of the intended signal) cancels the flux caused by the return current and therfore the intended signal sees no increase in impedance. As a result, the common-mode choke suppresses the common-mode noise without attenuating the useful differential mode signal [105, 107].

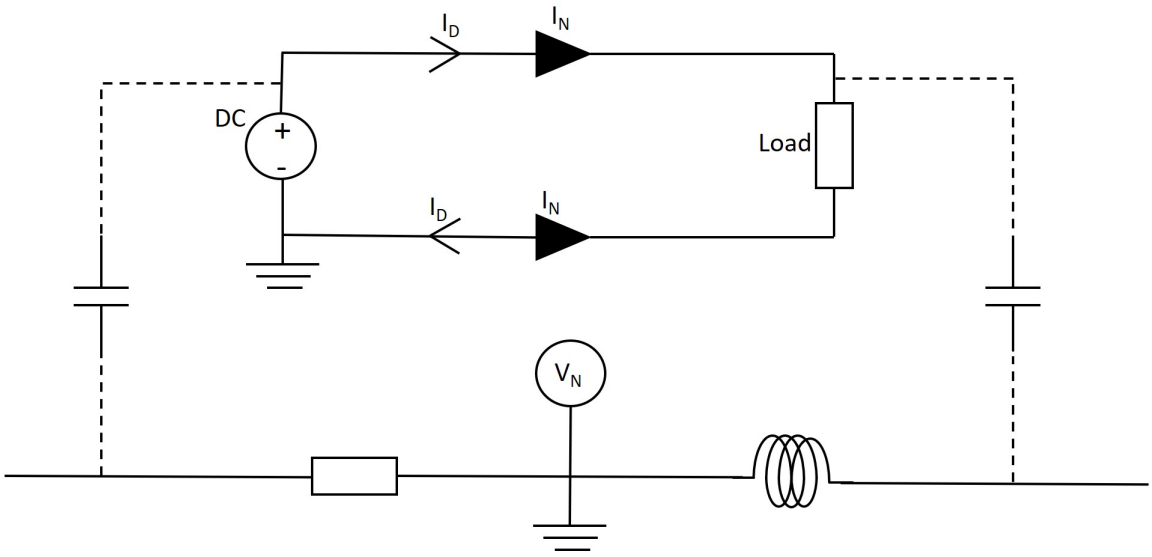

Figure 7.22: Common-mode noise coupling

7.3.5 Multi-Stage EMI Filter Design

Due to the wide frequency range of the noise produced by a switching mode power supply, it is difficult to provide one filter that suppresses all of the noise contributions. Therefore, a multi-stage Electromagnetic Interference (EMI) filter is required. EMI filters were added to all the outputs from the SMPS and the cryogenic amplifier voltage supply. The EMI filters were made in-house and the schematic for all of the filters can be seen in figure 7.23. The filters were based on a design by that of KainkaLabs[4] and adapted to suit the frequencies and currents required for our purposes. Due to time constraints the filters were not iterated, so further improvements could still be made. A comprehensive overview of EMI filter design can be found in [108] which details the purpose of every part of the filter in figure 7.23, an overview of which is provided below.

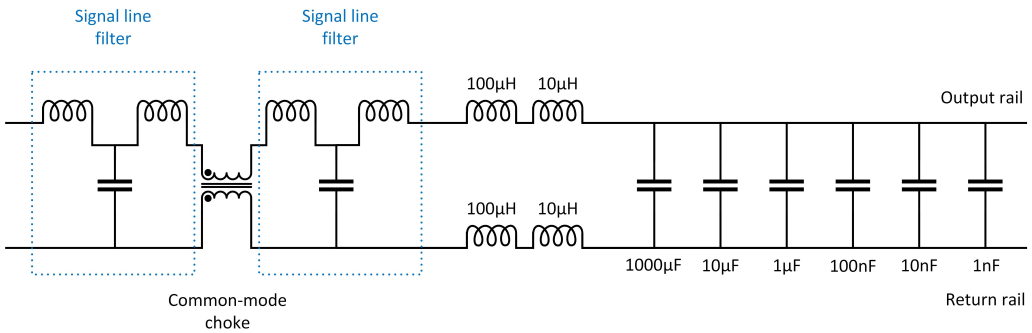

Figure 7.23: Schematic for the multi-stage EMI filters

[4] As of 2018 these are now available with documentation from http://www.ak-modul-bus.de

The input of each filter consists of a pair of signal line filters (also known as feedthrough capacitors) either side of a common-mode choke. The signal line filters serve to filter out very high frequency noise above 100 MHz [109] and the common-mode choke prevents common-mode noise from propagating to the load.

The inductors and capacitors form a low pass filter covering a wide frequency range. Multiple inductors and capacitors are required because no inductor or capacitor is an ideal component [9]. The impedance (Z) of an ideal inductor follows

$$Z = j\omega L, \tag{7.6}$$

where ω is the frequency of the signal passing through the inductor with inductance (L). Therefore, as the frequency increases, the impedance presented by the inductor grows. This also means that the intended DC signal will be presented with a low impedance and pass unaffected. However, in reality an inductor has a self-resonant frequency above which its impedance begins to fall again, as shown in figure 7.24b. To ensure that a high impedance is presented to a wider frequency range two inductors are used in series, so that when one inductor's impedance starts to fall, the other inductor takes over in presenting a high impedance to the noise.

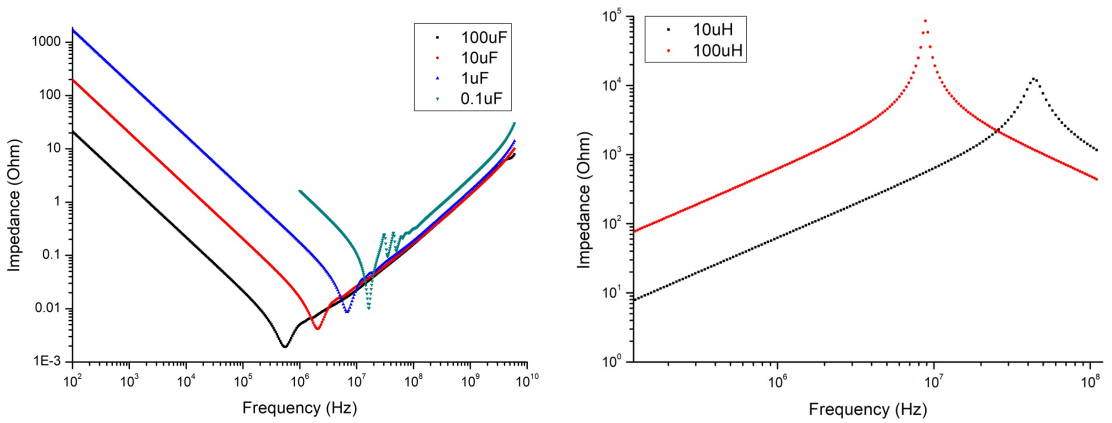

(a) Frequency dependent behaviour of capacitors (b) Frequency dependent behaviour of inductors

Figure 7.24: Frequency dependent behaviour of real components [10]

The capacitors are used to provide a low impedance path to ground, but figure 7.24a shows that after a self-resonant dip the capacitor's impedance begins to rise again. Therefore, more than one capacitor is used in parallel so that when the impedance of the first capacitor begins to rise, the noise sees the impedance of the second capacitor, and so on down the line. This ensures that a wide frequency range of noise is shorted to the return rail.

Finally, the filter is kept as symmetric as possible with signal line filters either side of the common-mode choke and inductors on both the output rail and the return rail. This is to ensure that the filter presents a balanced impedance to the noise as imbalance can cause some of the common-mode noise to be converted to residual differential mode noise [104, 110].

The EMI filters made for the current supply were manufactured to be capable of passing 20 A and the filters for the voltage supplies were manufactured to be capable of passing 2 A. Components for the 20 A filter were harder to source due to the necessity to pass such a high current. As a result the 100 μH inductors were hand-wound using 1.6 mm diameter wire on iron powder cores that would not saturate at 20 A. The signal filters were also impossible to find operating at 20 A and therefore an explicit SMD capacitor was used with two ferrite sleeves with the values chosen to match that of the purchased signal line filters. Finally, the tracks for the 20 A filter were designed to have a width of 12 mm to ensure that they would be capable of carrying 20 A. An example circuit board of the 20 A and 2 A filters can be seen in figure 7.25.

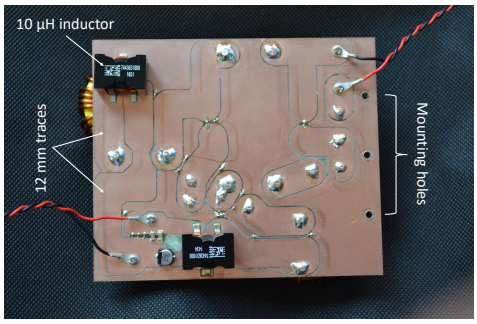

(a) 20 A Filter - front

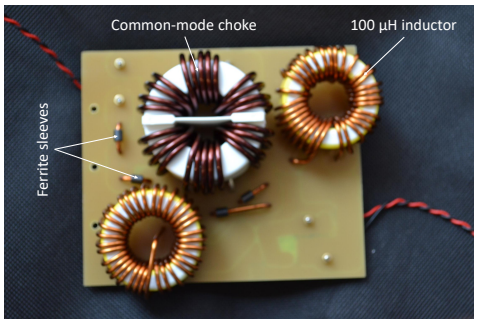

(b) 20 A filter - back

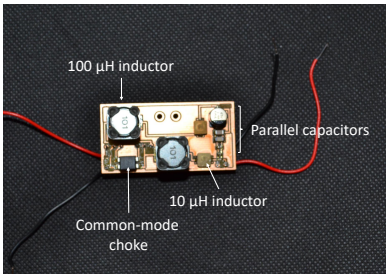

(c) 2 A filter

Figure 7.25: Multi-stage EMI filters

7.3.6 Filter Testing

All of the filters were tested using a 1 Vpp signal from a function generator with the voltage response recorded on a spectrum analyser. The insertion loss was then calculated using [8]

$$\text{Insertion Loss} = 20 \cdot \text{Log}\left(\frac{|V_1|}{|V_2|}\right), \tag{7.7}$$

where V_1 is the voltage at the load without the filter installed, and V_2 is the voltage at the load when the filter is installed. The average insertion loss for the 20 A filters at 23 MHz was 49 dB and an example is shown in figure 7.26. The average insertion loss for the 2 A filters at 23 MHz was 51 dB.

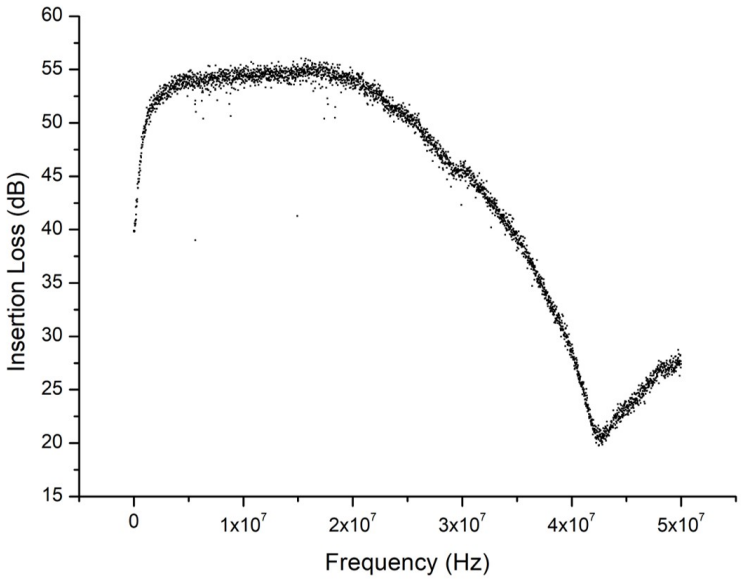

Figure 7.26: Insertion loss of a 20 A filter

7.3.7 Results Of Installing Multi-Stage EMI Filters

The multi-stage EMI filters were installed inside the 300 K electronics housing box and the detection signal was re-measured on the spectrum analyser. Figure 7.27a shows the size of the original noise problem presented in section 7.3 and figure 7.27b shows the detection signal after the installation of the EMI filters.

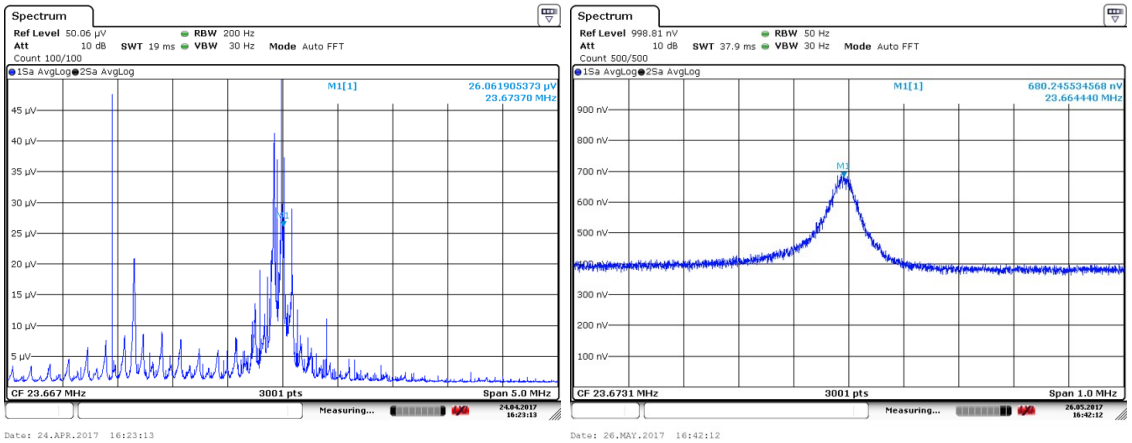

(a) Initial noise from current supply (b) Noise free signal

Figure 7.27: Overall improvement in the noise on the detection signal

The Lorentz profile from the resonator can now be seen clearly without being obstructed by noise spikes. To detect a single electron an axial dip of $\approx$ 70 Hz needs to be resolved. A cloud of electrons would would lead to a wider dip which scales with the number of electrons in the cloud. Both of these cases should now be easily resolved on the FFT.

7.4 Generating electrons

7.4.1 Room Temperature

The electrons are generated directly from the chip using an ultraviolet (UV) light emitting diode (LED) source. The UV photons liberate photoelectrons from the metalisation layer of the chip, which for the first trapping attempts was the 80:20 gold silver alloy. To eject electrons from the surface of the chip, the UV source must provide photons with an energy greater than the work function of the surface. The work function (Φ) of the gold silver alloy can be estimated using [111]

$$\Phi_{\mathrm{AuAg}} = \Phi\mathrm{Ag} + (\Phi_{\mathrm{Au}} - \Phi_{\mathrm{Ag}})x^2, \tag{7.8}$$

where x is the fractional content of gold. Taking the room temperature work function of gold as 5.1 eV and silver as 4.26 eV [112] gives the Geonium Chip a theoretical work function of 4.80 eV. Therefore, a 240 nm LED source (*Ocean Optics*), which provides photons with an energy of 5.166 eV, should be sufficient to eject electrons from the chip at room temperature. This was tested using a benchtop vacuum chamber and picoam-

meter kindly lent by the ITCM group at Sussex. The experimental setup can be seen in figure 7.28 where pickup wires have been arranged in a grid above the chip to collect any photoelectrons ejected from the chip. The pickup wires are connected to the picoammeter using a custom made triaxial cable which is required to ensure the photoelectron signal is distinguishable above the noise. Additionally, the chip is connected to a power supply which is used to make the chip more positive and find the voltage at which the electrons stop flowing from the chip to the pickup wires. The results can be seen in figure 7.29 where the maximum photocurrent detected was 8 pA and the stopping voltage calculated from a linear fit was 316 mV. This gives the Geonium Chip a measured work function of

$$\Phi_{\mathrm{AuAg}} = 5.166 - 0.316 = 4.85\,\mathrm{eV}. \tag{7.9}$$

This is consistent with the theoretically calculated value of 4.80 eV, when the errors in reading the small scale on the picoammeter are taken into account.

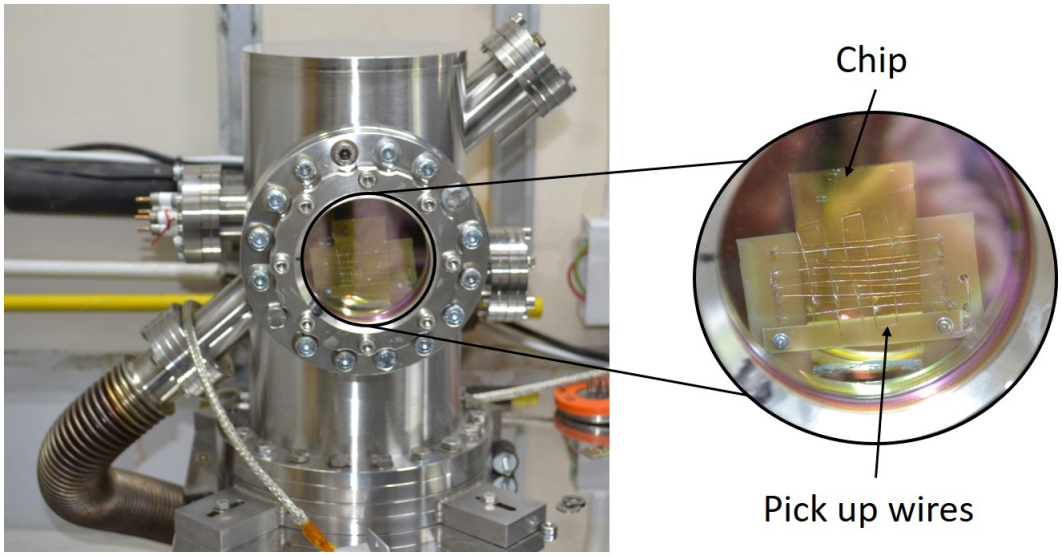

Figure 7.28: Experimental setup to measure the electrons ejected from the Geonium chip

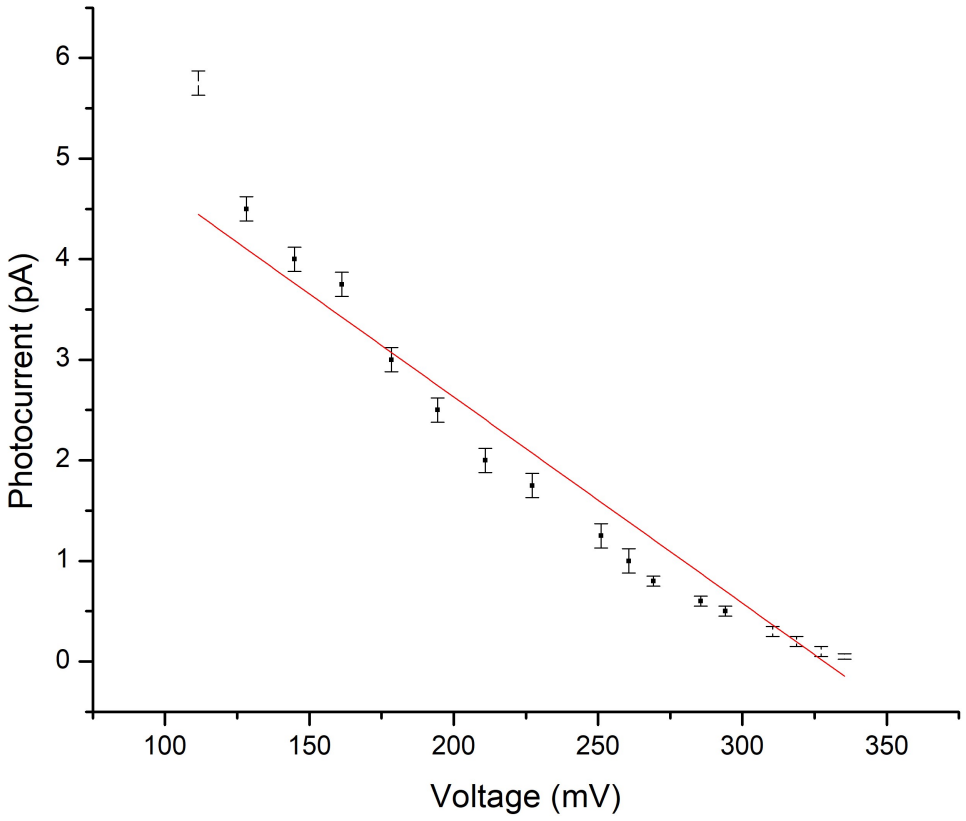

Figure 7.29: Stopping voltage of the Geonium chip

7.4.2 Cryogenic Temperatures

Now that the UV source has been shown to eject electrons from the chip at room temperature it has to be tested at 4 K. Firstly, the work function of a metal varies with temperature according to [113]

$$\Phi(T) = \Phi_0 - \gamma \frac{(k_B T)^2}{\Phi_0}, \tag{7.10}$$

where γ is a metal specific constant, k_B is the Boltzmann constant in electronvolts and Φ_0 can be expressed in terms of the free electron density(n)

$$\Phi_0 = \frac{e^3 m^{1/2} n^{1/6}}{16^3 \sqrt{3} \pi^{5/3} \hbar \epsilon_0^{3/2}}, \tag{7.11}$$

where e is the elementary charge, m is the mass of the electron, $\hbar$ is the reduced Planck constant and ϵ_0 is the vacuum permittivity. This gives a cryogenic work function of silver as

$$\Phi_{\mathrm{Ag}}(4.2K) = 4.331\,\mathrm{eV} \tag{7.12}$$

and, using equation 7.8, a cryogenic work function of the Geonium chip is estimated as 4.87 eV. Therefore, an electron ejected from the chip at 4.2 K should have an energy of,

$$\text{Photon Energy} = 5.166 - 4.86 = 0.296\,\text{eV} \tag{7.13}$$

with the energy equally distributed between the three degrees of freedom to give the electron an initial axial energy of ~ 0.1 eV.

As the work function of the chip has reduced with temperature it was expected that the *Ocean Optics* UV source would still eject electrons from the chip at 4 K. However, the first trapping attempts were unsuccessful. The first two reasons considered for this were that either the *Ocean Optics* source was not powerful enough to ensure that photons reached the surface of the chip (they pass through two optical fibres and the window of the microwave chamber) or at least one of the trapping voltages was not reaching the chip and therefore a harmonic potential well was not formed above the surface of the chip. To investigate the former an additional UV source was borrowed from *Hamamatsu* (UV-VIS fiber light source). This source supplied light over a range of 200 to 1600 nm with a deuterium lamp and a 9W tungsten halogen lamp. By contrast the *Ocean Optics* source only supplied 240 nm with a FWHM of 11 nm and a minimum power of 2 μW when coupled into a fibre.

To test whether the sources were ejecting electrons from the chip whilst it was held at 4 K, one of the electrodes was connected to the picoammeter via a trap voltage connection. All the other electrodes were grounded outside of the cryostat at the 300 K electronics housing box. The picoammeter was connected to the ungrounded electrode via a triaxial cable whose outer shield was grounded to reduce noise fluctuations from obscuring the signal. When the *Hamamatsu* source was switched on a current of ~ 5 pA was detected on the picoammeter. Repeating this test for all other electrodes found that all but one showed a clear current flow of photoelectrons. One electrode gave a noisy fluctuating response which implied that this electrode had a loose connection somewhere within the system. This was discovered to be true when the system was warmed up and opened for inspection. The same test was repeated with the *Ocean Optics* source at 4 K and room temperature, and no response was seen on any electrode. Therefore, this source is either not powerful enough to ensure UV photons reach the chip or creates such a small current that it cannot be detected on a picoammeter. Either way, this source is not suitable for the Geonium Chip experiment as we need to be able to check that electrons are being

ejected before we begin trapping attempts. Additionally, this test checks that the probes are touching the contact pads of the chip to deliver the trapping voltages.

Chapter 8

Summary And Outlook

8.1 Summary

This thesis details the work undertaken in the budding experimental Geonium Group at the University of Sussex. The work includes the following:

- **Network analysis of the detection system** - Microwave network analysis was used to theoretically analyse the detection system and calculate the optimal values of the coupling capacitors between the chip, resonator and cryogenic amplifier.
- **High frequency analysis of the Geonium Chip** - Two different techniques were used to couple to the contact pads of the Geonium Chip. The S-parameters of each technique were measured using a VNA. These scattering parameters were then transformed to admittance parameters which were used to calculate the inter-electrode and chip's input capacitances.
- **4 K characterisation of the planar magnetic field source** - The planar magnetic field source was installed in the cryostat and cooled to 4 K. The magnetic field of this source was measured for each shim separately to calculate the adjustments needed to make the Γ matrix applicable at temperatures below the source's critical temperature.
- **Building and optimisation of the detection system** - The Q-factor of the helical resonator was measured at cryogenic temperatures and then optimised to achieve a value of 34,400 at 2.6 K. Along with building a cryogenic amplifier, an investigation was conducted to study the effects of both the gate one voltage and the input capacitor, on the resonance frequency and Q-factor of the detection system. A superconducting transmission line was built to provide a low capacitance

connection between the chip and the helical resonator. The cryogenic amplifier and superconducting transmission line were both tested at 4 K. They were then coupled to the chip and the resonator to complete the detection system.

- **Thermalisation of the cryostat** - The radiation shields were improved to prevent radiative heating of the cryostat. In addition, the magnetic field current wiring was carefully designed to prevent loading of the 4 K experimental region, which would prevent the cryostat from reaching its base temperature. Once all of the experimental wiring had been installed in the cryostat, temperatures as low as 3.97 K were achieved.

- **Noise reduction** - Noise on the detection signal was eliminated using judicious cable shielding, grounding and cable management. Additionally, multi-stage EMI filters were built and applied to both the magnetic field currents and cryogenic amplifier voltages.

- **Generation of electrons** - The generation of photoelectrons was demonstrated at 300 K and 4 K.

8.2 Outlook

Following the demonstrated generation of electrons at 4 K, trapping attempts were planned but challenges were encountered with the detection system.

Once the experiment was cooled to 4 K, the cryogenic amplifier and room temperature electronics were switched on, and the voltage response of the resonator was observed on the FFT for ~ 2 minutes before decaying into the noise floor. This hints that the detection system connected to Geonium Chip and the connection of the wafer probes to the chip at 4 K require further investigation. At 300 K, once the resonator is attached to the Geonium Chip and the trap filters, the resonator's signal cannot be seen without external excitation. This is possibly due to the large losses of the Geonium Chip, modelled by R_s in chapter 4, combined with the losses due to the trap filters. The resistive losses in the chip include the resistance of the buried wires which connect the contact pads to the electrodes. At 300 K, these resistances have been measured to be 1.75 kΩ and a recent 4 K measurement of this resistance has yielded 25 Ω. However, the thermalisation of the chip during this measurement could be improved and therefore the measurement should be repeated once this has been achieved. It is expected that all the other losses in the chip will reduce with temperature in a similar manner to the resistance of the buried wires. If the resistance

falls further with improved thermalisation techniques then perhaps the reason that the detection signal disappeared after $\sim$ 2 minutes is due to the thermalisation of the chip. When the cryogenic amplifier is switched on, the resistance of the buried wires is low enough to observe the signal, but over time the amplifier raises the temperature of the 4 K region and as a result the resistance of the buried wires, which causes the resonator signal to decay. This therefore requires further investigation.

In the design of the next generation Geonium Chip the cross-section of the buried wires should be increased to ensure that the resonator can be observed with the chip at 300 K, making debugging of the system easier when problems occur. Additionally, the gaps between the contact pads, which are currently 10 μm wide, should also be increased. As these gaps are outside the microwave chamber they do not disturb the trapping potential but they are also unprotected from dust and other contaminants. As a result, every time the cryostat is opened contaminants settle in the gaps creating resistances to ground in the order of MΩs. Cleaning the chip in situ is a difficult and time consuming process which reduces some of these MΩ resistances, but cleaning cannot eliminate them entirely. When the chip is cooled to 4 K these resistances become un-measurable with a multimeter and are therefore greater than 200 MΩ (the upper limit of the multimeter), but they may not be completely eliminated. Therefore, the design of the second generation Geonium Chip should use larger insulating gaps around the contact pads.

Once the challenge with the detection signal has been solved, attempts to trap a cloud of electrons can continue. Using a cloud of electrons, the optimum tuning ratio can be found experimentally by adjusting T_c and measuring the fluctuations of the electrons' axial frequency with temperature. The optimum tuning ratio will be found when the axial frequency no longer fluctuates with temperature. The cloud of electrons can then be reduced to a single electron by exciting the cloud with a resonant frequency and then lowering the trap depth. This causes the hottest electrons to leave the trap and can be repeated until one electron remains. The Γ matrix of the magnetic field prototype could then be measured with the single electron to produce the most homogeneous field possible with our magnetic field source.

Once the trapping of a single electron has been demonstrated with the Geonium Chip, attention can turn to the interesting applications to which the Geonium Chip is suited. The Geonium Chip has the potential to bring accurate mass spectrometry to a wider market with a smaller footprint and capital outlay than the popular Orbitrap or FT-ICR. Additionally, single MW photon detection is still an experimental challenge and may lead

to applications in the first quantum radar.

As of September 2018 the Geonium Group have switched from the microfabricated chip to a PCB based chip. This has reduced the output capacitances from 40 pF to 3 pF and allowed the resonator to be seen whilst connected to the chip at room temperature. PhD candidate Alberto Uribe has measured a Q-factor of 670 for the entire detection system which is capable of resolving a single electron. Additionally, the PCB based chip has provided photocurrents of greater than 100 pA at 4 K. Therefore, the Geonium Group is continuing to their attempts to trap a cloud of electrons which they should achieve in the near future.

Bibliography

[1] J. Pinder. *The Geonium Chip - engineering a scalable planar Penning trap*. PhD thesis, University of Sussex, 2016. 17, 44, 45, 56, 57, 61, 62, 63, 64, 82, 84, 103, 104, 105

[2] J.W. Ekin. *Experimental Techniques For Low-Temperature Measurements*. Oxford University Press, 2006. 60, 107, 117

[3] M. L. Kidd. Watch Out for Those Thermoelectric Voltages ! *Cal Lab: International Journal of Metrology*, pages 18–21, 2012. 107

[4] J. Pinder and J. Verdú. A planar Penning trap with tunable dimensionality of the trapping potential. *International Journal of Mass Spectrometry*, 356:49–59, 2013. viii, 14, 15, 17, 18, 19, 21, 22, 28, 43, 66, 67, 79, 147, 148, 149

[5] P. Edwards. Initial report on the application of the Geonium Chip for Accurate Mass Spectrometry. Technical report, Polestar Engineering, 2015. 8

[6] J Verdú. Theory of the coplanar-waveguide Penning trap. *New Journal of Physics*, 13(11):113029, 2011. 12, 14, 16, 19, 20

[7] A. Al-Rjoub and J. Verdú. Electronic detection of a single particle in a coplanar-waveguide Penning trap. *Applied Physics B: Lasers and Optics*, 107(4):955–964, 2012. 26, 27, 29

[8] D. M. Pozar. *Microwave Engineering*. John Wiley & Sons, 4th edition, 2012. 32, 34, 35, 36, 40, 46, 47, 51, 127

[9] C. Bowick. *RF Circuit Design*. Elsevier Science, 1982. 53, 82, 125

[10] Murata. SimSurfing (DL). `www.murata.com/en-eu/tool/download/simsurfing`, 2017. [Acessed 23 Nov 2017]. 125

[11] H.G. Dehmelt. Radiofrequency Spectroscopy of Stored Ions I: Storage. *Advances in Atomic, Molecular and Optical Physics*, 3:53–72, 1968. 1

[12] H.G. Dehmelt. Radiofrequency Spectroscopy of Stored Ions II: Spectroscopy. *Advances in Atomic, Molecular and Optical Physics*, 5:109–154, 1969. 1

[13] F.M. Penning. Die glimmentladung bei niedrigem druck zwischen koaxialen zylindern in einem axialen magnetfeld. *Physica*, 3(9):873–894, 1936. 1

[14] H.G. Dehmelt. Experiments with an Isolated Subatomic Particle at Rest. *AIP Conference Proceedings*, 233(1):28–45, 1991. 1

[15] D. Wineland, P. Ekstrom, and H. Dehmelt. Monoelectron Oscillator. *Physical Review Letters*, 31(21):1279–1282, 1973. 1

[16] R. Van Dyck, P. Ekstrom, and H. Dehmelt. Axial, magnetron, cyclotron and spin-cyclotron-beat frequencies measured on single electron almost at rest in free space (geonium). *Nature*, 262(5571):776–777, 1976. 1

[17] R.S. Van Dyck, P.B. Schwinberg, and H.G. Dehmelt. Precise Measurements of Axial, Magnetron, Cyclotron, and Spin-Cyclotron-Beat Frequencies on an Isolated 1-meV Electron. *Physical Review Letters*, 38(7):310–314, 1977. 1

[18] M.H. Holzscheiter. Ion-Trap Quantum Computation. *Los Alamos Science*, 27:264–283, 2002. 2

[19] H. Häffner, C. Roos, and R. Blatt. Quantum computing with trapped ions. *Physics Reports*, 469(4):155–203, 2008.

[20] P. Schindler, D. Nigg, T. Monz, J. T. Barreiro, E. Martinez, S. X. Wang, S. Quint, M. F. Brandl, V. Nebendahl, C. F. Roos, M. Chwalla, M. Hennrich, and R. Blatt. A quantum information processor with trapped ions. *New Journal of Physics*, 15(12):123012, 2013. 2

[21] K.R. Brown, J. Kim, and C. Monroe. Co-designing a scalable quantum computer with trapped atomic ions. *Npj Quantum Information*, 2, 2016.

[22] I. Marzoli, P. Tombesi, G. Ciaramicoli, G. Werth, P. Bushev, S. Stahl, F. Schmidt-Kaler, M. Hellwig, C. Henkel, G. Marx, I. Jex, E. Stachowska, G. Szawiola, and A. Walaszyk. Experimental and theoretical challenges for the trapped electron

quantum computer. *Journal of Physics B: Atomic, Molecular and Optical Physics*, 42(15):154010, 2009. 2

[23] S. Stahl, F. Galve, J. Alonso, S. Djekic, W. Quint, T. Valenzuela, J. Verdú, M. Vogel, and G. Werth. A planar Penning trap. *The European Physical Journal D*, 32(1):139–146, 2005. 2

[24] M. D. Hughes, B. Lekitsch, J.A. Broersma, and W.K. Hensinger. Microfabricated ion traps. *Contemporary Physics*, 52(6):505–529, 2011. 2

[25] D. Cho, S. Hong, M. Lee, and T. Kim. A review of silicon microfabricated ion traps for quantum information processing. *Micro and Nano Systems Letters*, 3(1):31–34, 2015. 2

[26] G. Ciaramicoli, I. Marzoli, and P. Tombesi. Scalable quantum processor with trapped electrons. *Physical Review Letters*, 91(1):017901, 2003. 2

[27] G. Ciaramicoli, I. Marzoli, and P. Tombesi. Trapped electrons in vacuum for a scalable quantum processor. *Physical Review A*, 70(3):032301, 2004. 2

[28] S. Peil and G. Gabrielse. Observing the quantum limit of an electron cyclotron: QND measurements of quantum jumps between Fock states. *Physical Review Letters*, 83(7):1287–1290, 1999. 2, 4

[29] M. Hellwig, A. Bautista-Salvador, K. Singer, G. Werth, and F. Schmidt-Kaler. Fabrication of a planar micro Penning trap and numerical investigations of versatile ion positioning protocols. *New Journal of Physics*, 12, 2010. 2

[30] J. R. Castrejón-Pita and R. C. Thompson. Proposal for a planar Penning ion trap. *Physical Review A*, 72(1):013405, 2005.

[31] J. R. Castrejón-Pita, H. Ohadi, D. R. Crick, D. F. A. Winters, D. M. Segal, and R. C. Thompson. Novel designs for Penning ion traps. *Journal of Modern Optics*, 54(11):1581–1594, jul 2007. 2

[32] F. Galve, P. Fernández, and G. Werth. Operation of a planar Penning trap. *The European Physical Journal D*, 40(2):201–204, 2006. 2

[33] F. Galve and G. Werth. Motional frequencies in a planar Penning trap. *Hyperfine Interactions*, 174(1-3):41–46, 2007. 2

[34] P. Bushev, S. Stahl, R. Natali, G. Marx, E. Stachowska, G. Werth, M. Hellwig, and F. Schmidt-Kaler. Electrons in a cryogenic planar Penning trap and experimental challenges for quantum processing. *The European Physical Journal D*, 50(1):97–102, 2008. 2

[35] J. Goldman and G. Gabrielse. Optimized planar Penning traps for quantum information studies. *Hyperfine Interactions*, 199(1):279–289, 2011. 2

[36] J.D. Goldman. *Planar Penning Traps with Anharmonicity Compensation for Single-Electron Qubits*. PhD thesis, Harvard, 2011. 2, 43

[37] M. Vogel. The anomalous magnetic moment of the electron. *Contemporary Physics*, 50(3):437–452, 2009. 2

[38] D. Hanneke, S. Fogwell, and G. Gabrielse. New Measurement of the Electron Magnetic Moment and the Fine Structure Constant. *Physical Review Letters*, 100(12), 2008. 2

[39] D. Hanneke, S. Fogwell Hoogerheide, and G. Gabrielse. Cavity control of a single-electron quantum cyclotron: Measuring the electron magnetic moment. *Physical Review A*, 83(5), 2011. 2

[40] R.S. Van Dyck, P.B. Schwinberg, and H.G. Dehmelt. New high-precision comparison of electron and positron g factors. *Physical Review Letters*, 59(1):26–29, 1987. 3

[41] H. Dehmelt, R. Mittleman, R.S. Van Dyck, and P. Schwinberg. Past Electron-Positron g - 2 Experiments Yielded Sharpest Bound on CPT Violation for Point Particles. *Physical Review Letters*, 83(23):4694–4696, 1999. 3

[42] C. Smorra, K. Blaum, L. Bojtar, M. Borchert, K.A. Franke, T. Higuchi, N. Leefer, H. Nagahama, Y. Matsuda, A. Mooser, M. Niemann, O. Ospelkaus, W. Quint, G. Schneider, S. Sellner, T. Tanaka, S. Van Gorp, J. Walz, Y. Yamazaki, and S. Ulmer. BASE - The Baryon Antibaryon Symmetry Experiment. *The European Physical Journal Special Topics*, 224:3055–3108, 2015. 3

[43] S. Ulmer, C. Smorra, A. Mooser, K. Franke, H. Nagahama, G. Schneider, T. Higuchi, S. Van Gorp, K. Blaum, Y. Matsuda, W. Quint, J. Walz, and Y. Yamazaki. High-precision comparison of the antiproton-to-proton charge-to-mass ratio. *Nature*, 524(7564):196–199, 2015. 3

[44] F. Heiße, F. Köhler-Langes, S. Rau, J. Hou, S. Junck, A. Kracke, A. Mooser, W. Quint, S. Ulmer, G. Werth, K. Blaum, and S. Sturm. High-Precision Measurement of the Proton's Atomic Mass. *Physical Review Letters*, 119(3):033001, 2017. 3

[45] E.R. Cohen and B.N. Taylor. The 1986 CODATA Recommended Values of the Fundamental Physical Constants. *Journal of Physical and Chemical Reference Data*, 17(4):1795–1803, 1988. 3

[46] K. Blaum, Yu.N. Novikov, and G. Werth. Penning traps as a versatile tool for precise experiments in fundamental physics. *Contemporary Physics*, 51(2):149–175, 2010. 3

[47] R.H. Hadfield. Single-photon detectors for optical quantum information applications. *Nature Photonics*, 3(12):696–705, 2009. 3

[48] M. Keller, B. Lange, K. Hayasaka, W. Lange, and H. Walther. Continuous generation of single photons with controlled waveform in an ion-trap cavity system. *Nature*, 431(7012):1075–1078, 2004.

[49] B. B. Blinov, D.L. Moehring, L.-M. Duan, and C. Monroe. Observation of entanglement between a single trapped atom and a single photon. *Nature*, 428(6979):153–157, 2004. 3

[50] A.J. Manninen, A. Kemppinen, J. Lehtinen, E. Mykkanen, G. Amato, E. Enrico, V. Lacquaniti, M. Kataoka, T. Lindstrom, R. Dolata, M. Khabipov, B. Jalali Jafari, S.V. Lotkhov, A.B. Zorin, R.E. Lake, M. Mottonen, J.P. Pekola, R. George, Yu.A. Pashkin, J. Prance, O. Astafiev, P.J. Meeson, and K. Porsch. Towards measurement and control of single-photon microwave radiation on chip. In *2015 1st URSI Atlantic Radio Science Conference (URSI AT-RASC)*. IEEE, 2015. 3

[51] G. Romero, J.J. García-Ripoll, and E. Solano. Microwave Photon Detector in Circuit QED. *Physical Review Letters*, 102(17):173602, 2009. 3, 5

[52] K. Inomata, Z. Lin, K. Koshino, W.D. Oliver, J. Tsai, T. Yamamoto, and Y. Nakamura. Single microwave-photon detector using an artificial L-type three-level system. *Nature Communications*, 7, 2016. 3, 4

[53] A. Cridland, J. Lacy, J. Pinder, and J. Verdú. Single Microwave Photon Detection with a Trapped Electron. *Photonics*, 3(4):59, 2016. 4, 5

[54] S.R. Sathyamoorthy, T.M. Stace, and G. Johansson. Detecting itinerant single microwave photons. *Comptes Rendus Physique*, 17(7):756–765, 2016. 4

[55] B. Peropadre, G. Romero, G. Johansson, C.M. Wilson, E. Solano, and J.J. García-Ripoll. Approaching perfect microwave photodetection in circuit QED. *Physical Review A*, 84(6):063834, 2011. 4

[56] J. Bartlett, G. Hardy, and I.D. Hepburn. Performance of a fast response miniature Adiabatic Demagnetisation Refrigerator using a single crystal tungsten magnetoresistive heat switch. *Cryogenics*, 72:111–121, 2015. 4

[57] H.G. Dehmelt. Continuous Stern-Gerlach effect: Principle and idealized apparatus. *Proceedings of the National Academy of Sciences of the United States of America*, 83(8):2291–4, 1986. 4

[58] Frost and Sullivan. Global Mass Spectrometry Market, Forecast to 2022. Technical report, Frost & Sullivan, 2016. 6

[59] A.G. Marshall and T. Chen. 40 years of Fourier transform ion cyclotron resonance mass spectrometry. *International Journal of Mass Spectrometry*, 377:410–420, 2015. 6

[60] A.G. Marshall, C.L. Hendrickson, and G.S. Jackson. Fourier transform ion cyclotron resonance mass spectrometry: A primer. *Mass Spectrometry Reviews*, 17(1):1–35, 1998. 6

[61] Q. Hu, R.J. Noll, H. Li, A. Makarov, M. Hardman, and R.G. Cooks. The Orbitrap: a new mass spectrometer. *Journal of Mass Spectrometry*, 40(4):430–443, 2005. 7

[62] R.A. Zubarev and A. Makarov. Orbitrap Mass Spectrometry. *Analytical Chemistry*, 85(11):5288–5296, 2013. 7

[63] A. Makarov. Electrostatic Axially Harmonic Orbital Trapping: A High-Performance Technique of Mass Analysis. *Analytical Chemistry*, 72:1156–1162, 2000. 7

[64] L.S. Brown and G. Gabrielse. Precision spectroscopy of a charged particle in an imperfect Penning trap. *Physical Review A*, 25(4):2423–2425, 1982. 9

[65] L.S. Brown and G. Gabrielse. Geonium theory: Physics of a single electron or ion in a Penning trap. *Reviews of Modern Physics*, 58(1):233–311, 1986. 14, 16, 19, 20, 108

[66] M. Kretzschmar. Theory of the elliptical Penning trap. *International Journal of Mass Spectrometry*, 275(1-3):21–33, 2008. 17, 18, 19

[67] P. Paasche, C. Angelescu, S. Ananthamurthy, D. Biswas, T. Valenzuela, and G. Werth. Instabilities of an electron cloud in a Penning trap. *The European Physical Journal D*, 22(2):183–188, 2003. 18

[68] M. Knoop. Physics with Trapped Charged Particles. In M. Knoop, N. Madsen, and R.C. Thompson, editors, *Physics with Trapped Charged Particles: Lectures from the Les Houches Winter School*. World Scientific Publishing Europe Ltd., 2014. 23

[69] R. Alheit, C. Hennig, R. Morgenstern, F. Vedel, and G. Werth. Observation of instabilities in a Paul trap with higher-order anharmonicities. *Applied Physics B Lasers and Optics*, 61(3):277–283, 1995. 23

[70] J.A.V. Otamendi. *Development of an Experiment for Ultrahigh-Precision g-Factor Measurements in a Penning-Trap Setup*. PhD thesis, Johannes Gutenberg University of Mainz, 2007. 23, 25

[71] X. Feng, M. Charlton, M. Holzscheiter, R.A. Lewis, and Y. Yamazaki. Tank circuit model applied to particles in a Penning trap. *Journal of Applied Physics*, 79(1):8, 1996. 28

[72] D.J. Wineland and H.G. Dehmelt. Principles of the stored ion calorimeter. *Journal of Applied Physics*, 46(2):919–930, 1975. 29, 30, 31

[73] H.G. Dehmelt and F.L. Walls. "Bolometric" Technique for the rf Spectroscopy of Stored Ions. *Physical Review Letters*, 21(3):127–131, jul 1968. 30

[74] W.M. Itano, J.C. Bergquist, J.J. Bollinger, and D.J. Wineland. Cooling methods in ion traps. *Physica Scripta*, T59:106–120, 1995. 30

[75] S. Ulmer, K. Blaum, H. Kracke, A. Mooser, W. Quint, C.C. Rodegheri, and J. Walz. A cryogenic detection system at 28.9MHZ for the non-destructive observation of a single proton at low particle energy. *Nuclear Instruments and Methods in Physics Research Section A: Accelerators, Spectrometers, Detectors and Associated Equipment*, 705:55–60, 2013. 31, 81, 88, 91

[76] S. Ulmer, H. Kracke, K. Blaum, S. Kreim, A. Mooser, W. Quint, C.C. Rodegheri, and J. Walz. The quality factor of a superconducting rf resonator in a magnetic field. *Review of Scientific Instruments*, 80(12), 2009. 32, 81, 84

[77] W.W Macalpine and R.O. Schildknecht. Coaxial Resonators with Helical Inner Conductor. *Proceedings of the IRE*, 47(12):2099–2105, 1959. 32, 82

[78] R. Boylestad and L. Nashelsky. *Electronic Devices And Circuit Theory*. Prentice-Hall International, 7th edition, 1999. 34

[79] A. Niknejad. Scattering Parameters. http://rfic.eecs.berkeley.edu/~niknejad/ee242/pdf/eecs242_lect5_sparam.pdf, 2014. [Acessed 23 Nov 2017]. 47

[80] K. Kurokawa. Power Waves and the Scattering Matrix. *IEEE Transactions on Microwave Theory and Techniques*, 13(2):194–202, 1965. 47

[81] J. Pan and P. Fraud. Wire bonding challenges in Optoelectronics packaging. *Proceedings of the 1st SME Annual Manufacturing Technology Summit: Dearborn, MI*, 2004. 49

[82] J.D. Irwin. *Basic Engineering Circuit Analysis*. Macmillan, 2nd edition, 1987. 50

[83] G. Wilpers, P. See, P. Gill, and A.G. Sinclair. A compact UHV package for microfabricated ion-trap arrays with direct electronic air-side access. *Applied Physics B*, 111(1):21–28, 2013. 64

[84] G. Gabrielse and H. Dehmelt. Observation of inhibited spontaneous emission. *Physical Review Letters*, 55(1):67–70, 1985. 64

[85] J.L. Verdú. Ion Trap, 2013. 45, 70, 77

[86] J. Lacy. *Untitled*. PhD thesis, University of Sussex, 2018. 72

[87] A. Chowdhury and S. Bhattacharjee. Experimental investigation of change in sheet resistance and Debye temperatures in metallic thin films due to low - energy ion beam irradiation. *Journal of Physics D: Applied Physics*, 46(43):435304, 2013. 73

[88] G.T. Meaden. *Electrical resistance of metals*. Springer, 2013. 73

[89] Supercon Inc. NbTi Superconducting Wires. http://www.supercon-wire.com/content/nbti-superconducting-wires. [13 Oct 2017]. 78

[90] P. Fabbricatore, G. Gemme, R. Musenich, R. Parodi, M. Viviani, B. Zhang, and V. Buscaglia. Niobium and Niobium-Titanium Nitrides for rf Applications. *IEEE Transactions on Applied Superconductivity*, 3(1):1761–1764, 1993. 82

[91] J. Yeh and S.M. Anlage. In situ broadband cryogenic calibration for two-port superconducting microwave resonators. *Review of Scientific Instruments*, 84(3):034706, 2013. 86

[92] M. Freeman. Cryogenic Electronics. In R. Richardson and E. Smith, editors, *Experimental Techniques In Condensed Matter Physics At Low Temperatures*, chapter 4, pages 201–202. 1988. 88

[93] J.W. Lamb. Evaluation of biasing and protection circuitry components for cryogenic MMIC low-noise amplifiers. *Cryogenics*, 61:43–54, 2014. 88

[94] F. Teyssandier and D. Prêle. Commercially Available Capacitors at Cryogenic Temperatures. *Ninth International Workshop on Low Temperature Electronics - WOLTE9*, 2010. 88

[95] J. Bourne, R. Schupbach, B. Hollosi, J. Di, A. Lostetter, and H.A. Mantooth. Ultra-wide temperature (-230C to 130C) DC-motor drive with SiGe asynchronous controller. *IEEE Aerospace Conference Proceedings*, pages 1–15, 2008. 88

[96] S. Ulmer. *First Observation of Spin Flips with a Single Proton Stored in a Cryogenic Penning Trap*. PhD thesis, University of Heidelberg, 2011. 88

[97] U. Tietze and Ch. Schenk. *Electronic Circuits: Handbook for Design and Applications*. Springer, 2nd edition, 2002. 88

[98] A.M. Niknejad. Two-Port Networks and Amplifiers. `http://citeseerx.ist.psu.edu/viewdoc/download?doi=10.1.1.146.5770&rep=rep1&type=pdf`, 2008. [Acessed 23 Nov 2017]. 90

[99] S.R. Jefferts, T. Heavner, P. Hayes, and G.H. Dunn. Superconducting resonator and a cryogenic GaAs field-effect transistor amplifier as a single-ion detection system. *Review of Scientific Instruments*, 64(3):737–740, 1993. 95

[100] R.C. Weast. *Handbook of Chemistry and Physics*. The chemical Rubber Co., 53rd edition, 1972. 104

[101] S. Stahl. Cryogenic Low Pass Filter Unit, 2009. 108

[102] N. Masuhara, J.M. Doyle, J.C. Sandberg, D. Kleppner, T.J. Greytak, H.F. Hess, and G.P. Kochanski. Evaporative Cooling of Spin-Polarized Atomic Hydrogen. *Physical Review Letters*, 61(8):935–938, 1988. 108

[103] R. Mcfee. Optimum Input Leads for Cryogenic Apparatus. *Review of Scientific Instruments*, 30(1959):98, 1959. 112, 116

[104] G. Vasilescu. *Electronic Noise and Interfering Signals: Principles and Applications*. Springer-Verlag, 2005. 120, 122, 126

[105] H.W. Ott. *Noise Reduction Techniques In Electronic Systems*. John Wiley & Sons, 2nd edition, 1936. 120, 121, 123

[106] R. Morrison. *Noise And Other Interfering Signals*. Wiley-Interscience, 1992. 122

[107] Murata. Differential and Common Mode Noise. https://www.murata.com/~/media/webrenewal/products/emc/emifil/knowhow/26to30.ashx. [Acessed 23 Nov 2017]. 123

[108] R. Ozenbaugh and T. Pullen. *EMI Filter Design*. CRC Press, 3rd edition, 2012. 124

[109] Murata. Lead EMIFILr Capacitor Type for General Small Type DSN6/DSS6 Series I Dimension DSN6 Series. http://docs-europe.electrocomponents.com/webdocs/08d0/0900766b808d0ee3.pdf, 2006. [Acessed 23 Nov 2017]. 125

[110] S. Maniktala. Safety concerns for practical EMI line filters, 2003. 126

[111] S. Fain and J. McDavid. Work-function variation with alloy composition: Ag-Au. *Physical Review B*, 9(12):5099–5107, 1974. 128

[112] H. Kawano. Effective work functions for ionic and electronic emissions from mono- and polycrystalline surfaces. *Progress in Surface Science*, 83(1-2):1–165, 2008. 128

[113] R. Rahemi and D. Li. Variation in electron work function with temperature and its effect on the Young's modulus of metals. *Scripta Materialia*, 99:41–44, 2015. 130

[114] J. Verdú, S. Kreim, K. Blaum, H. Kracke, W. Quint, S. Ulmer, and J. Walz. Calculation of electrostatic fields using quasi-Green's functions: application to the hybrid Penning trap. *New Journal of Physics*, 10(10):103009, 2008. 149

Appendix A

Electrostatic Potential Of The Geonium Chip

The functions for the potential contributions from the electrodes and the gaps between them depend upon the dimensions of the electrodes which are shown diagrammatically in figure A.1.

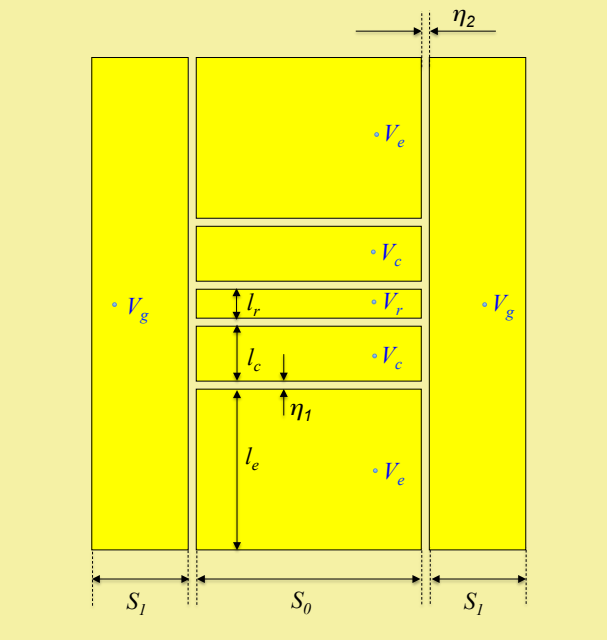

Figure A.1: The dimensions of the electrodes of the Geonium Chip where the axes origin (0, 0, 0) is defined to be at the center of the ring electrode. The electrodes are surrounded by a ground plane [4].

The total potential for the boxed trapped (equation 2.2) has already been expressed as a combination of the electrostatic potential given by the electrodes plus that given by

the gaps between the electrodes. The potential given by the electrodes in equation 2.3 depends upon the terms $\Lambda^r_{m,n}$, $\Lambda^c_{m,n}$, $\Lambda^e_{m,n}$ and $\Lambda^g_{m,n}$ which are stated in table A.1. Here, r refers to the ring, c to the correction electrodes, e to the endcaps and g to the side electrodes.

Table A.1: Functions defining the contribution of each of the trap's electrodes to the electrostatic potential given in equation 2.3 [4].

$$\begin{aligned}\Lambda^r_{m,n} &= \left\{\cos\left(\frac{m\pi\,(L_z+l_r)}{2\,L_z}\right)-\cos\left(\frac{m\pi\,(L_z-l_r)}{2\,L_z}\right)\right\}\times\left\{\cos\left(\frac{m\pi\,(L_x+S_0)}{2\,L_x}\right)\right.\\ &\left.-\cos\left(\frac{m\pi\,(L_x-S_0)}{2\,L_x}\right)\right\}. \qquad (A.1)\end{aligned}$$

$$\begin{aligned}\Lambda^c_{m,n} &= \left\{\cos\left(\frac{m\pi\,(L_z+l_r+2\eta_1+2l_c)}{2\,L_z}\right)-\cos\left(\frac{m\pi\,(L_z+l_r+2\eta_1}{2\,L_z}\right)+\cos\left(\frac{m\pi\,(L_z-l_r-2\eta_1)}{2\,L_z}\right)\right.\\ &\left.-\cos\left(\frac{m\pi\,(L_z-l_r-2\eta_1-2l_c}{2\,L_z}\right)\right\}\times\left\{\cos\left(\frac{m\pi\,(L_x+S_0)}{2\,L_x}\right)-\cos\left(\frac{m\pi\,(L_x-S_0)}{2\,L_x}\right)\right\}. \qquad (A.2)\end{aligned}$$

$$\begin{aligned}\Lambda^e_{m,n} &= \left\{\cos\left(\frac{m\pi\,(L_z+l_r+4\eta_1+2l_c+2l_e)}{2\,L_z}\right)-\cos\left(\frac{m\pi\,(L_z+l_r+4\eta_1+2l_c)}{2\,L_z}\right)+\cos\left(\frac{m\pi\,(L_z-l_r-4\eta_1-2l_c)}{2\,L_z}\right)\right.\\ &\left.-\cos\left(\frac{m\pi\,(L_z-l_r-4\eta_1-2l_c-2l_e)}{2\,L_z}\right)\right\}\times\left\{\cos\left(\frac{m\pi\,(L_x+S_0)}{2\,L_x}\right)-\cos\left(\frac{m\pi\,(L_x-S_0)}{2\,L_x}\right)\right\}. \qquad (A.3)\end{aligned}$$

$$\begin{aligned}\Lambda^g_{m,n} &= \left\{\cos\left(\frac{m\pi\,(L_x+S_0+2\eta_2+2S_1)}{2\,L_x}\right)-\cos\left(\frac{m\pi\,(L_x+S_0+2\eta_2)}{2\,L_x}\right)+\cos\left(\frac{m\pi\,(L_x-S_0-2\eta_2)}{2\,L_x}\right)\right.\\ &\left.-\cos\left(\frac{m\pi\,(L_x-S_0-2\eta_2-2S_1)}{2\,L_x}\right)\right\}\times\left\{\cos\left(\frac{m\pi\,(L_z+L_0)}{2\,L_z}\right)-\cos\left(\frac{m\pi\,(L_z-L_0)}{2\,L_z}\right)\right\}. \qquad (A.4)\end{aligned}$$

The potential created by the small insulating gaps between each of the central electrodes is obtained by substituting the expression $V_r\cdot(\Lambda^r_{m,n}+T_c\,\Lambda^c_{m,n}+T_e\,\Lambda^e_{m,n}+T_s\,\Lambda^s_{m,n})$ in ϕ_{el} of equation 2.3, by the function $\Pi^i_{m,n}$ given in equation A.5. In that equation i refers to the interface between two particular neighbour central electrodes. Therefore, following down from the top of figure A.1 there are 6 possibilities for i: ground plane $\overset{1}{-}$ endcap $\overset{2}{-}$ correction $\overset{3}{-}$ ring $\overset{4}{-}$ correction $\overset{5}{-}$ endcap $\overset{6}{-}$ ground place and therefore six functions that describe the potential due to the gaps between the central electrodes.

Additionally, the interfacing gaps between the five central electrodes and each of the side electrodes have to be taken into account. Here, the function $\Pi^j_{m,n}$, equation A.6, is used instead of $\Pi^i_{m,n}$. In total there are 2×5 $\Pi^j_{m,n}$ functions to take into account the left and right side electrode.

Table A.2: Functions with the contributions of the different gaps to $\phi_{\text{gaps}}(\vec{r})$ [4].

$$\Pi^{i}_{m,n} = -\frac{1}{m\pi}\left\{\cos\left(\frac{n\pi x'}{L_x}\right)\Big|_{x'\to x \text{ limits}}\left(L_z\, k\, \sin\left(\frac{m\pi z'}{L_z}\right)\right.\right. \\ \left.\left. -m\pi(kz'+l)\cos\left(\frac{m\pi z'}{L_z}\right)\right)\Big|_{z'\to z \text{ limits}}\right\}. \quad \text{(A.5)}$$

$$\Pi^{j}_{m,n} = -\frac{1}{n\pi}\left\{\cos\left(\frac{m\pi z'}{L_z}\right)\Big|_{z'\to z \text{ limits}}\left(L_x\, k\, \sin\left(\frac{n\pi x'}{L_x}\right)\right.\right. \\ \left.\left. -n\pi(kx'+l)\cos\left(\frac{n\pi x'}{L_x}\right)\right)\Big|_{x'\to x \text{ limits}}\right\}. \quad \text{(A.6)}$$

The potentials created by all the insulating gaps are approximated by a linear interpolation between the neighbouring electrodes (for more details see [114]). In equations A.5 and A.6 the symbols k and l represent the slope and the y-intercept of the linear interpolation of the potential, respectively. The *x limits* and *z limits* define the size and position of the gap. For the gap between the left side electrode and the central electrodes the *x limits* are $\left\{\frac{S_0}{2}, \frac{S_0}{2}+\eta_2\right\}$ and for the gap between the right side electrode and the central electrodes the *x limits* are $\left\{-\frac{S_0}{2}-\eta_2, -\frac{S_0}{2}\right\}$ (remembering that the origin of the axes is defined as the centre of the ring electrode). The values of *z limits* depend on the particular electrodes. For example, *z limits* takes the values $\left\{\frac{l_r}{2}, \frac{l_r}{2}+\eta_1\right\}$ and $\left\{-\frac{l_r}{2}-\eta_1, -\frac{l_r}{2}\right\}$, for the gap between the ring and the upper and lower correction electrodes, respectively. Similar expressions define the values of *z limits* for all other interfaces between neighbouring central electrodes.

Appendix B

Full Chip Measurement Data

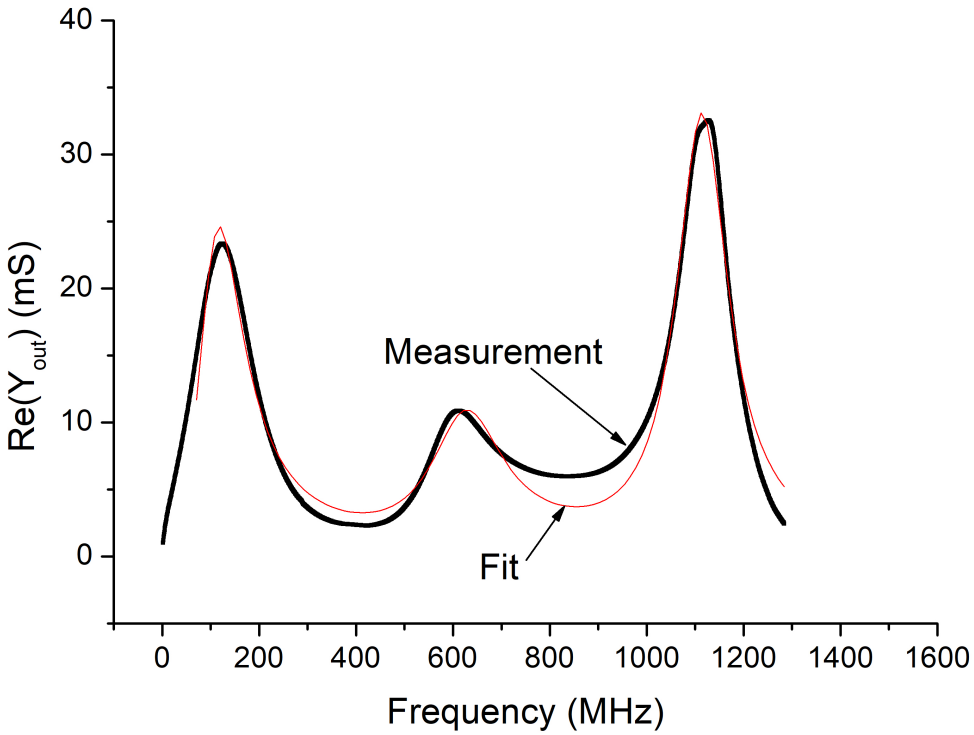

Figure B.1: The black data points are the real part of one Y_{out} parameter of the Geonium chip, where the input port was set to the left correction electrode and the output port was set to the ring electrode. The chip's S-parameters were measured using a vector network analyser and transformed to Y-parameters using standard conversion equations. The red line is a fit of three 'real' capacitors connected in parallel to one another. The adjusted R-squared for the fit is 0.97631.

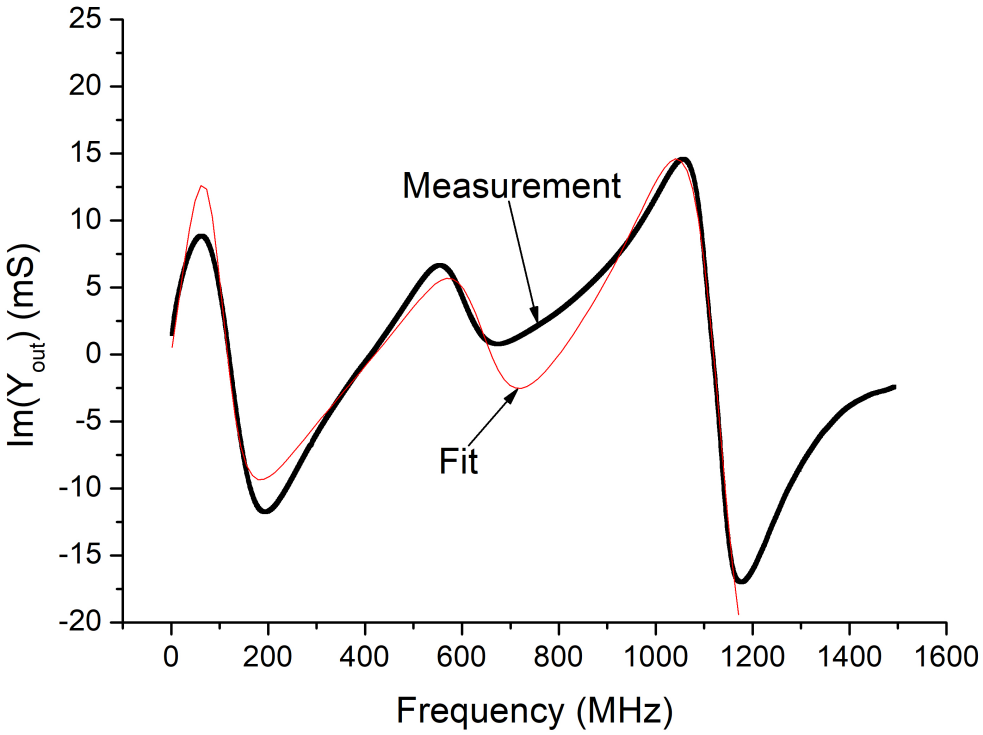

Figure B.2: The black data points are the imaginary part of one Y_{out} parameter of the Geonium chip, where the input port was set to the left correction electrode and the output port was set to the ring electrode. The chip's S-parameters were measured using a vector network analyser and transformed to Y-parameters using standard conversion equations. The red line is a fit of three 'real' capacitors connected in parallel to one another. The adjusted R-squared for the fit is 0.96999.

Table B.1: 300K Geonium chip output parameters

Electrode	Value ± Error		
	R_s (Ω)	L (nH)	C (pF)
Left Endcap	37.2 ± 0.2	44.3 ± 0.3	42.4 ± 0.4
	63.7 ± 0.5	45.8 ± 0.5	1.11 ± 0.01
	19.99 ± 0.07	25.8 ± 0.1	0.58 ± 0.003
Right Endcap	38.0 ± 0.1	34.9 ± 0.1	43.7 ± 0.3
	79.8 ± 0.5	62.8 ± 0.6	0.882 ± 0.008
	24.06 ± 0.07	21.92 ± 0.09	0.44 ± 0.002
Ring	39.5 ± 0.1	51.3 ± 0.3	36.6 ± 0.3
	75.7 ± 0.5	39.1 ± 0.7	0.841 ± 0.009
	27.51 ± 0.08	28.7 ± 0.1	0.566 ± 0.002
Right Correction	38.3 ± 0.1	37.0 ± 0.1	43.0 ± 0.3
	73.3 ± 0.3	54.1 ± 0.4	1.006 ± 0.007
	26.3 ± 0.07	23.84 ± 0.09	0.448 ± 0.002
Left Correction	37.8 ± 0.1	42.0 ± 0.2	43.7 ± 0.3
	61.0 ± 0.3	43.6 ± 0.4	1.195 ± 0.009
	21.60 ± 0.06	2.4 ± 0.1	0.564 ± 0.002

Table B.2: Inter-electrode capacitances between the correction electrodes and the rest of the electrodes

Electrode	Value ± Error		
	R_s (Ω)	L (nH)	C (pF)
Left Correction to Ring	363 ± 13	838 ± 44	17.6 ± 1.3
	101.5 ± 0.6	74.25 ± 0.05	5.65 ± 0.06
	75.6 ± 0.5	136.5 ± 0.9	0.149 ± 0.001
	20.79 ± 0.03	23.12 ± 0.03	0.4403 ± 0.0007
Right Correction to Ring	359 ± 14	815 ± 46	17.9 ± 1.4
	102.1 ± 0.7	77.4 ± 0.7	5.48 ± 0.07
	72.4 ± 0.5	134 ± 1.0	0.154 ± 0.001
	21.83 ± 0.03	23.3 ± 0.4	0.4423 ± 0.0007
Left Correction to Left Endcap	361 ± 18	555 ± 49	20 ± 2
	98 ± 1	73 ± 1	4.7 ± 1.0
	31.4 ± 0.2	82.5 ± 0.4	0.212 ± 0.001
	21.18 ± 0.05	27.97 ± 0.08	0.3225 ± 0.0009
Left Correction to Right Endcap	158 ± 2	142 ± 2	2.82 ± 0.4
	207 ± 4	270 ± 6	0.225 ± 0.005
	63.9 ± 0.5	134 ± 1	0.128 ± 0.001
	13.20 ± 0.01	23.3 ± 0.03	0.4361 ± 0.0006
Right Correction to Right Endcap	344 ± 20	502 ± 57	20 ± 3
	107 ± 2	86 ± 2	4.2 ± 0.1
	37.0 ± 0.3	83.58 ± 0.06	0.211 ± 0.002
	15.24 ± 0.04	25.21 ± 0.07	0.363 ± 0.001
Right Correction to Left Endcap	154 ± 2	137 ± 2	2.9 ± 0.5
	201 ± 4	259 ± 6	0.233 ± 0.006
	65.8 ± 0.6	149 ± 1	0.117 ± 0.001
	15.41 ± 0.03	24.63 ± 0.04	0.4149 ± 0.0007
Left Correction to Right Correction	120 ± 1	103 ± 1	4.0 ± 0.5
	215 ± 4	268 ± 6	20.12 ± 0.005
	76.0 ± 0.6	129 ± 1	0.150 ± 0.001
	16.55 ± 0.03	24.46 ± 0.04	0.4528 ± 0.0008

Table B.3: Inter-electrode capacitances between the endcap electrodes and the rest of the electrodes

Electrode	Value ± Error		
	R_s (Ω)	L (nH)	C (pF)
Left Endcap to Ring	132.3 ± 0.9	107.7 ± 0.9	3.74 ± 0.04
	498 ± 10	266 ± 8	0.161 ± 0.005
	99.1 ± 0.7	157 ± 1	0.117 ± 0.001
	19.66 ± 0.03	28.53 ± 0.04	0.3384 ± 0.0005
Right Endcap to Ring	137.9 ± 0.9	116 ± 1	3.50 ± 0.03
	562 ± 12	307 ± 10	0.155 ± 0.005
	97.1 ± 0.6	146 ± 1	0.126 ± 0.001
	17.02 ± 0.02	28.09 ± 0.03	0.3442 ± 0.0004
Left Endcap to Right Endcap	196 ± 4	182 ± 4	2.02 ± 0.05
	220 ± 5	328 ± 10	0.217 ± 0.007
	32.5 ± 0.2	102.6 ± 0.6	0.1460 ± 0.0008
	10.95 ± 0.02	19.13 ± 0.03	0.5224 ± 0.0008

Appendix C

Electronic Components

Capacitors

Value	Brand	Dielectric	Tolerance	Package
10nF	Panasonic	PPS	±2%	0805
1μF	Panasonic	PPS	±20%	1210
470pF	Phycomp	NP0	±5%	0805
100pF	TDK	C0G	±5%	0603
22pF	AVX	C0G	±2%	0603

Resistors

Value	Brand	Technology	Tolerance	Temperature Co-efficient	Package
100MΩ	TE Connectivity RN73	Thick film	±10%	±100ppm/°C	0805
1MΩ	Bourns CRT Series	Thin film	±0.1%	±25ppm/°C	0805
100kΩ	Vishay MCT series	Thin film	±0.5%	±25ppm/°C	0603
10kΩ	TE Connectivity RN73	Thin film	±0.1%	±10ppm/°C	0603
820Ω	TE Connectivity CPF	Thin film	±0.1%	±25ppm/°C	0805
470Ω	Vishay TNPW series	Thin film	±0.1%	±10ppm/°C	0603
100Ω	TE Connectivity RN73	Thin film	±0.1%	±10ppm/°C	0805